

Kristoffer Stabell Andersson

# Co-Simulation of an IPMSM Drive Using Comsol and Simulink

Master's thesis in Electric Power Engineering

Supervisor: Robert Nilssen

Co-supervisor: Roy Nilsen and Aravinda Perera

June 2021

NTNU  
Norwegian University of Science and Technology  
Faculty of Information Technology and Electrical Engineering  
Department of Electric Power Engineering



Norwegian University of  
Science and Technology



Kristoffer Stabell Andersson

# **Co-Simulation of an IPMSM Drive Using Comsol and Simulink**

Master's thesis in Electric Power Engineering  
Supervisor: Robert Nilssen  
Co-supervisor: Roy Nilsen and Aravinda Perera  
June 2021

Norwegian University of Science and Technology  
Faculty of Information Technology and Electrical Engineering  
Department of Electric Power Engineering





## Abstract

The finite element method (FEM) is the standard approach to evaluate the performance and design of electrical machines. Interior permanent magnet synchronous motors (IPMSM) are gaining increased popularity in traction applications, aerospace and marine propulsion with benefits for field weakening, robust rotor design for high-speed applications, and increased peak torque due to reluctance. This thesis describes how to obtain a co-simulation model of a FEM IPMSM with Comsol LiveLink for Simulink. It is modeled one sector of the motor using antiperiodic boundary conditions. The motor is star connected, with a rated phase-voltage of 230.00 V<sub>RMS</sub>, a rated phase-current of 4.93 A<sub>RMS</sub>, rated speed of 1000 RPM, and a rated torque of 27.80 Nm for the IPMSM drive. The torque control is based on vector maximum torque per ampere (MTPA) with the modulus optimum strategy. Speed control is using the symmetrical optimum strategy. Continuous proportional-integral (PI) controllers are used with feed-forward signals to improve the dynamic performance in the drive. The applied voltage signals from the d-axis and q-axis are, in principle, sinusoidal. Since the carrier-frequency PWM generated ripple phenomenon is neglected in the drive, the overall dynamic response of the electric machine is investigated, including cogging torque, saturation, cross-coupling, and the influence from the spatial harmonics on the torque.

Further, the FEM *model* of an IPMSM motor is compared with the equivalent lumped parameter *model* (LPM). This comparison shows that when pure inner loop MTPA control mode is used, the estimated reference torque from the control system is larger than the real produced torque by the FEM model (an error that can also be measured in a real motor). The torque error implies that the voltage given by the control system becomes too low in the q-axis compared with the LPM model. The applied currents are approximately equal for the LPM and FEM model. The consequence of the torque error is a reduced speed for a given load condition. When the cascade outer speed controller is added, the co-simulation drive system reaches the requested reference speed of 1.00 pu. However, the reference torque from the regulators is estimated too high, approximately 0.8913 pu, compared to the FEM model, approximately 0.8835 pu. A lower torque causes the FEM model phase voltage and currents to lag the LPM model. Furthermore, the error in the torque estimation in the LPM model is strongly increased when saturation is taken into account for the reference torque up to 2.00 pu. The LPM model is reaching 2.00 pu, while the FEM model is reaching approximately 1.92 pu. For reference torque less than 0.25 pu, the differences between the LPM and FEM models are negligible. It is observed from the results that the LPM model, in general, seems to have a faster dynamic response compared to the FEM model.

Late in the study, it was discovered, from what seemed to be a too low transient overshoot value in the FEM motor, that the computed parameters could be too low. It was assumed that the constant d-axis inductance was highly saturated. The saturated parameters, obtained with the field solution, were calculated with 100.00% positive d-and q-axis current. The drive is, for the most part operating in a much less saturated mode. A better drives description was achieved by recomputing the parameters with a -40.00% negative d-axis and +90.00% positive q-axis current in Comsol. The d-axis parameter was increased by 31.60%, and the new q-axis parameter increased with negligible 0.97%. The recomputed d-axis inductance improved the transient response and the voltage error in the FEM co-simulation from -6.19% to -2.63% when a 1.00 pu torque reference was applied, which is an improvement in voltage accuracy of 3.56%. A conclusion from this is that an accurate parameter computation is needed for co-simulation to mitigate torque errors.

Limitations with co-simulation for motor control are the inherent long computational time, required data storage, convergence issues further out in the co-simulation, and generally few references on the topic. Co-simulations with Comsol have been a challenging task - with practically no reference within drives co-simulations. It is obvious that Comsol must improve the documentation and support regarding the numerical co-simulation solver implementation and computer utilization. Nevertheless, co-simulation with Comsol LiveLink can potentially be a feasible tool for more accurate drive systems design in the future. The results presented in this thesis demonstrates the many opportunities of incorporating Comsol FEM models in a more general drives systems analysis. A frequency response analysis and stability analysis have been performed with the idealized LPM model.

## Sammendrag

Endelig elementmetoder (FEM) er standardtilnærmingen for å vurdere ytelse og design til elektriske maskiner. Permanent-magnet-synkron-motorer med innfelte magneter (IPMSM) øker i popularitet innen trekkapplikasjoner, romfart og marin fremdrift med fordeler som feltsvekking, et robust rotordesign for høyhastighetsmotorer og økt toppmoment på grunn av reluktans. Denne hovedoppgaven inneholder en detaljert beskrivelse om hvordan det kan bli utført en samsimulering av en FEM IPMSM med programvaren Comsol LiveLink for Simulink. Det er modellert en sektor av motoren ved bruk av antiperiodiske grensebetingelser. Motoren er stjerne koblet med en nominell fasespenning på 230,00 V<sub>RMS</sub>, en nominell fasestrøm på 4,93 A<sub>RMS</sub>, en nominell hastighet på 1000 RPM og et nominelt dreiemoment på 27,80 Nm. Dreiemomentreguleringen er basert på maksimalt-moment-per-ampere (MTPA) med «modulus optimum» vektor styringsstrategi i det roterende *dq*-referanseplanet. Hastighetsregulatoren bruker «symmetrical optimum» styringsstrategi. Kontinuerlige proporsjonal-integral-regulatorer (PI) brukes, med foroverkobling for å forbedre den dynamiske ytelsen i motordriften. De påførte spenningssignalene fra d-aksen og q-aksen er i prinsippet sinusformet. Puls-bredde-moduleringen (PWM) fra omformerer er linearisert med en ekvivalent første-ordens transferfunksjon tidsforsinkelse. Siden strøm- og moment-krusningene fra PWM bærer-frekvensen er neglisjert i motordriften, blir den generelle dynamiske responsen til den elektriske maskinen undersøkt uten påvirkning fra PWM. I samsimuleringen er det inkludert fenomener som romharmonisk dreiemoment som følge av stator-tenner, metning i blikk og effekter som tverrkobling mellom d-og q-aksen.

Videre sammenlignes FEM *modellen* til en IPMSM-motor med en ekvivalent parameterisert *modell* (LPM). Denne sammenligningen viser at når en ren indre sløyfe MTPA-kontrollmodus brukes, er det estimerte referansemomentet fra kontrollsystemet større enn det reelt produserte dreiemomentet fra FEM-modellen (et avvik som også kan måles i en ekte motor). Dreiemomentavviket innebærer at spenningen gitt av kontrollsystemet blir for lav i q-aksen sammenlignet med den genererte q-akse spenningen i LPM-modellen. Den påtrykte strømmen er omtrent lik for LPM- og FEM-modellen. Konsekvensen av dreiemomentavviket er redusert hastighet ved en gitt belastnings-forstyrrelse. Når den kaskade-koblede ytre-sløyfe hastighetsregulatoren blir lagt til, når samsimuleringen referansehastigheten på 1,00 pu. Referansemomentet fra momentregulatorene er imidlertid estimert for høyt på omtrent 0,8913 pu, sammenlignet med FEM-modellens dreiemoment på omtrent 0,8835 pu. Konsekvensene av et lavere dreiemoment er at FEM-modellens fasespenninger og -strømmer er forsinket i forhold til LPM-modellens. Feilen i dreiemomentets estimat i forhold til LPM-modellen øker ytterligere når maskinen går i kraftig metning med et påtrykt referansedreiemomentet på 2,00 pu. LPM-modellen når 2,00 pu, mens FEM-modellen når omtrent 1,92 pu. For et referansedreiemoment på 0,25 pu er forskjellene mellom LPM- og FEM-modellene ubetydelige. Det observeres fra resultatene at LPM-modellen generelt sett ser ut til å ha en raskere elektrisk innsvingningsrespons sammenlignet med FEM-modellen.

Sent i arbeidet ble det oppdaget, fra det som så ut til å være en for lav dynamisk respons i FEM-modellen, at de beregnede parameterne var for lave. Det ble på dette tidspunktet antatt at den forhåndsbestemte induktanseverdien i d-aksen var mettet. De mettede parameterne, beregnet med feltløsningen, ble estimert med en 100,00% positiv d- og q-aksestrøm. Motordriften fungerer for det meste i en tilstand med betydelig redusert metning i blikket. En bedre motordrift ble oppnådd ved å beregne parameterne på nytt i Comsol med en -40,00% negativ d-akse og +90,00% positiv q-aksestrøm. Parameteren i d-aksen ble økt med 31,60%, og den nye q-akseparameteren økte med ubetydelige 0,97 %. Den nye beregnede induktansen til d-aksen forbedret den dynamiske responsen, og spenningsfeilen i FEM-samsimuleringen gikk fra -6,19% til -2,63% når en referanse på 1,00 pu dreiemoment ble påtrykt. Dette er en forbedring i spenningsnøyaktigheten på 3,56% . En konklusjon fra dette er at en nøyaktig parameterberegning er nødvendig i samsimulering for å redusere dreiemomentsavviket.

Begrensninger med samsimulering for motorstyring er den iboende lange beregningstiden, lagring av større datamengder, konvergensproblemer lenger ut i samsimuleringen, og generelt få referanser om emnet. Samsimulering med Comsol har vært en utfordrende oppgave – hvor det i praksis ikke finnes referanser innen motorstyring for programvaren brukt i denne oppgaven. Det er åpenbart at Comsol må forbedre dokumentasjonen og støtten angående den numeriske samsimuleringsløsningsimplementering og utnyttelse av prosessorkraft. Likevel kan samsimulering med Comsol LiveLink for Simulink potensielt bli et verktøy for mer nøyaktig utvikling av fremtidens elektriske motordrifter. Resultatene presentert i denne oppgaven demonstrerer mulighetene for å innlemme Comsol FEM-modeller i en mer generell systemanalyse. En frekvensresponsanalyse og stabilitetsanalyse er utført med den idealiserte LPM-modellen.

# Co-Simulation of an IPMSM Drive Using Comsol and Simulink

Kristoffer Stabell Andersson  
Supervisor: Robert Nilssen  
Co-Supervisors: Roy Nilsen and Aravinda Perera  
June 2021 - Trondheim - Norway

**Abstract**—The finite element method (FEM) is the standard approach to evaluate the performance and design of electrical machines. Interior permanent magnet synchronous motors (IPMSM) are gaining increased popularity in traction applications, aerospace and marine propulsion with benefits for field weakening, robust rotor design for high-speed applications, and increased peak torque due to reluctance. This thesis describes how to obtain a co-simulation model of a FEM IPMSM with Comsol LiveLink for Simulink. It is modeled one sector of the motor using antiperiodic boundary conditions. The motor is star connected, with a rated phase-voltage of 230.00 V<sub>RMS</sub>, a rated-phase current of 4.93 A<sub>RMS</sub>, rated speed of 1000 RPM, and a rated torque of 27.80 Nm for the IPMSM drive. The torque control is based on vector maximum torque per ampere (MTPA) with the modulus optimum strategy. Speed control is using the symmetrical optimum strategy. Continuous proportional-integral (PI) controllers are used with feed-forward signals to improve the dynamic performance in the drive. The applied voltage signals from the d-axis and q-axis are, in principle, sinusoidal. Since the carrier-frequency PWM generated ripple phenomenon is neglected in the drive, the overall dynamic response of the electric machine is investigated, including cogging torque, saturation, cross-coupling, and the influence from the spatial harmonics on the torque.

Further, the FEM *model* of an IPMSM motor is compared with the equivalent lumped parameter *model* (LPM). This comparison shows that when pure inner loop MTPA control mode is used, the estimated reference torque from the control system is larger than the real produced torque by the FEM model (an error that can also be measured in a real motor). The torque error implies that the voltage given by the control system becomes too low in the q-axis compared with the LPM model. The applied currents are approximately equal for the LPM and FEM model. The consequence of the torque error is a reduced speed for a given load condition. When the cascade outer speed controller is added, the co-simulation drive system reaches the requested reference speed of 1.00 pu. However, the reference torque from the regulators is estimated too high, approximately 0.8913 pu, compared to the FEM model, approximately 0.8835 pu. A lower torque causes the FEM model phase voltage and currents to lag the LPM model. Furthermore, the error in the torque estimation in the LPM model is strongly increased when saturation is taken into account for the reference torque up to 2.00 pu. The LPM model is reaching 2.00 pu, while the FEM model is reaching approximately 1.92 pu. For reference torque less than 0.25 pu, the differences between the LPM and FEM models are negligible. It is observed from the results that the LPM model, in general, seems to have a faster dynamic response compared to the FEM model.

Late in the study, it was discovered, from what seemed to be a too low transient overshoot value in the FEM motor, that the computed parameters could be too low. It was assumed that the constant d-axis inductance was highly saturated. The saturated parameters, obtained with the field solution, were calculated with 100.00% positive d-and q-axis current. The drive is, for the most part operating in a much less saturated mode. A better drives description was achieved by recomputing the parameters with a -40.00% negative d-axis and +90.00% positive q-axis current in Comsol. The d-axis parameter was increased by 31.60%, and the new q-axis parameter increased with negligible 0.97%. The recomputed d-axis inductance improved the transient response and the voltage error in the FEM co-simulation from -6.19% to -2.63% when a 1.00 pu torque reference was applied, which is an improvement in voltage accuracy of 3.56%. A conclusion from this is that an accurate parameter computation is needed for co-simulation to mitigate torque errors.

Limitations with co-simulation for motor control are the inherent long computational time, required data storage, convergence issues further out in the co-simulation, and generally few references on the topic. Co-simulations with Comsol have been a challenging task - with practically no reference within drives co-simulations. It is obvious that Comsol must improve the documentation and support regarding the numerical co-simulation solver implementation and computer utilization. Nevertheless, co-simulation with Comsol LiveLink for Simulink can potentially be a tool for more accurate drive systems design in the future. The results presented in this thesis demonstrates the many opportunities of incorporating Comsol FEM models in a more general drives systems analysis. A frequency response analysis and stability analysis have been performed with the idealized LPM model.

**Index Terms**—IPMSM, co-simulation, Comsol, LiveLink, Simulink, drives systems, control theory, Finite Element Method.

## I. INTRODUCTION

**I**NTERIOR PERMANENT MAGNET MOTORS are gaining an increased popularity in traction applications like the automotive industry [1], aerospace [2] and marine propulsion [3], due to its wide operational range in field weakening [4], robust rotor design for high-speed applications, and increased peak torque due to reluctance [5]. In classical drives system simulations, the machine model is based on LPM with parameters estimated from tests or a FEM solution. However, an IPMSM is an electromagnetic component with effects like magnetic saturation in the electrical steel, harmonics due to slotting, cogging torque and torque ripples, and cross-coupling effects from the flux linkages. The non-linearities can greatly influence the performance of the drive [6]. Further, FEM is the standard for machine performance evaluation, and design [7].

Using the idealized model uses the assumption that [8] the magnetic saturation is neglected, all windings generate a sinusoidally distributed air gap field  $B_{ag}$ , symmetrical distribution of the windings, the physically distributed windings are concentrated, the parameters  $r_s$ ,  $l_s$  and  $\psi_m$  are independent of frequency and temperature (out of scope in this work). The LPM is not taking higher-order effects of the MMF field and is also referred to as the fundamental wave model. This is because the harmonic effects from slotting and skin effect are typically disregarded. In [6] it is derived a model that is taking saturation, cross, coupling, spatial harmonics, and temperature effects into consideration without using computer-intensive co-simulations. In [6] it is used LUT generated from the FEA simulation. The use of LUT for IPMSM is also described in [9], [10], [11]. LUT is out of scope in this thesis. However, LUTs are assumed to be linked to co-simulation since this allows for a more accurate magnetic representation of the machine in the controllers than using constant parameters.

This thesis will present how it is possible to enable the FEM model in a drives co-simulation using the software package Comsol LiveLink for Simulink. Co-simulation means that two or more software exchanges data at specified time intervals but performs a solution according to their own solver definitions within the time intervals between each communication point. Co-simulation is taking advantage of two software simulation programming languages enabling a holistic drive system simulation for future designs.

Previous work related to drives co-simulations can be found in the references listed here [7], [12], [13], [14], [15], [16], [17], [18], [19], [20], [21], [22], [23], [24], [25], [26], [27], [28], [29], [30], found during this work. It is published a paper from the Norwegian research institution SINTEF which describes eight guidelines for the users of co-simulations, not specifically for motor control in [31]. The guidelines are not complete or final but introduced to find tomorrow's design and technology solutions. It is also pointed out that these guidelines are not specific to the maritime industry but applicable in a wide range of engineering fields. Another article about co-simulation is given in [32].

A drive system involves analyzing power electronics with PWM control, electromagnetic, mechanical, and thermal con-

straints. An analysis of a multi-domain system calls for a designated simulation tool for each sub-domain. Co-simulation enables stand-alone subsystem interaction in a single simulation [7], [12]. To integrate several domain-analysis software platforms into one software, i.e., FEM and power electronics in one software can potentially translate into inaccurate computations [12, pp. 161–163]. The development of co-simulation software, powerful computational performance, and increased computational capacity allow analyzing complex multi-domain systems between FEM and the control of power electronics converters in the future [7], [25], [12] to mitigate the limitations of the idealized LPM approach.

The disadvantages of co-simulation are the computational time, required simplification of the converter and control system, a careful selection of the time step size [20], [25], a high amount of required data storage space [18], [19] and generally few references on the topic [7], [14]. It is several benefits to use a regular LPM model. It is in many cases possible to sufficiently analyze dynamic performance, voltages, and currents with a considerably shorter simulation time.

Previous works include the Ph.D. thesis of *Quintal* [7] where the aim was to design a small PMSG for operational and fault analysis. In [7] it is used PWM switching. Here the co-simulation connection cases are described with circuit diagrams. It is also mentioned in [7] that electrical machines can be unconventional, expensive to build, or difficult to manufacture. Co-simulation can then be a way to simulate fault-cases without risks of destroying a real machine in the co-simulation program - an argument enhancing the motivation for utilizing co-simulation. Motivations behind building fewer prototypes is also mentioned in [15]. The Ph.D. thesis of *Kanerva* [33] from 2005, where the aim was to develop a platform for a co-simulation environment capable of modeling and analyzing the interaction between electrical machines and controlled power electronics. More recent work includes *Quintal et al.* [14] with a modelling and co-simulation of a synchronous generator. *Bensalem et al.* [20] analyzed a fault case for induction motor in 2016 with a simplified inverter. In *Di Leonardo et al.* [25] it is performed a co-simulation of a 200 kW induction motor designed for traction EV, including cogging torque and saturation of iron with discrete controllers and SVPWM. In [28] it was described a method how to coupling a FEM model to a control system and comparing the lab results. In [28] co-simulations, the study highlighted the influence of cogging torque and torque ripples. In *Jagiela et al.* [34] from 2010 it was concluded that co-simulation can evaluate complex electromagnetically system operation. It was also concluded that the computational power required makes it unlikely for co-simulation to design control systems for electromagnetic components but can be used when more accurate details are required. In *Schulte et al.* [27], [26] it is stated that the two-step procedure is used for simulating the performance of the machine with the fundamental wave motors in the first step and the later step being a more accurate FEM design. It is mentioned that the accuracy of a dynamic drive co-simulation minimizes the limitations from the traditional two-step approach in drive design [27], [26]. In *Hang et al.* [24] it is used a FOC control scheme and SVPWM for an IM



where the leakage and passive elements are included.

### A. Relation to the Specialization Project

The specialization project did not use co-simulation, only electromagnetic models of a PMSM. This knowledge was needed because this project would have been highly challenging if electromagnetic modeling and co-simulation had to be learned simultaneously. One of the further work section goals in the specialization project is to obtain Comsol LiveLink for Simulink. That goal was written at the end of the specialization project when the LiveLink for Simulink software was released. The specialization project is given in reference [35].

### B. Targets and Scope

The targets are described as

- 1) The main objective in this thesis is to build a co-simulation Comsol Multiphysics LiveLink for Simulink platform and write a technical report about the modeling approach done in this thesis in detail.
- 2) Obtain results that highlight torque ripple, cogging torque, current ripples, voltage ripples, transient cross-coupling, and material saturation in a drive system simulation.
- 3) Compare the LPM motor drive with the FEA co-simulation motor.
- 4) Build and tune a drive system for co-simulation. Include a frequency response and dynamic analysis to evaluate the performance and avoid an unstable system. The frequency analysis and the stability analysis are done with the idealized LPM motor parameters.

The reader is expected to know

- 1) Machine design and FEM electromagnetic modelling [36], [5], [37].
- 2) Control theory [38].
- 3) Electrical drives [8], [39], [40],[4].

The following limitations and out of scope is

- 1) PWM switches and discrete controllers. The converter model is a linearized first-order transfer function, and the controllers are continuous.
- 2) Development of an advanced control system.
- 3) Mechanical, thermal, skin effects in the copper conductors, capacitive couplings between phases and ground, eddy currents, and electromagnetic losses [35] in the dynamic drive simulation.
- 4) Sensorless control.

### C. Organization of the Thesis

1) *Chapters:* It is included three theory chapters to separate FEM modelling in section II, control strategy in section III and general theory of co-simulation in section IV. It is included two modeling chapters. The first chapter section V is describing how the FEM model is set used for co-simulation. The second method chapter section VI is describing how the LiveLink for Simulink connection was made. The results are given in section VII. The first part of section VII is

analyzing the frequency response and stability of the system. The other parts are analyzing the results obtained from the co-simulation. All results from the co-simulation are included in the appendix. Some results are included in the main report result section. The discussion chapter is given in section VIII. The conclusion is in section IX. It is also made several appendices. The three last pages includes a table of contents, a list of symbols and a list of abbreviations, respectively.

2) *Notation:* All physics and features from Comsol are denoted with small bold letters. An example of this is **Coil group**. It is also indicated what physics feature is used in Comsol **RMM** or **EC**. Vectors are denoted with small bold letters **y**. Matrices are denoted with bold capital letters **C**.

## II. THEORY - FEM AND MACHINE DESIGN

### A. Introduction

*This subsection describes the theory behind the relevant properties in COMSOL and machine design theory that is relevant. An important note is that the 2D sector is working as a full machine for the co-simulation. This is required because if the coil length is too short, the applied voltage will yield a too high current.*

### B. IPMSM

Several electric and hybrid car manufacturers using PM materials in their motor topologies. PM motors make it possible to achieve the highest efficiencies and have negligible rotor Joule losses  $I_{rotor}^2 \cdot R_{rotor}$  [35],[4]. In addition, PM machines have a better power factor compared to induction motors, making the stator Joule losses  $I_s^2 \cdot R_s$  smaller compared to induction machines. It is often used vector control that requires knowledge about the rotor position with a pulse encoder. There is no general control method for the PMSM, as the optimal control strategy is dependent on the machine topology, i.e., surface mounted, embedded, and many other design factors [4, pp. 296–306]. An IPMSM can have different rotor topologies. A few examples are surface embedded, tangential embedded, V-shaped, I-shaped/radially embedded [36, p. 429] or synchronous reluctance rotor equipped with magnets (like the Tesla Model 3 [41]). The machine in this work belongs to the sub-group tangentially embedded magnets [36, p. 429].

A characteristic of an IPMSM is that magnets are embedded inside the rotor and not placed on the surface. Holes in the rotor lamination are made to hold the permanent magnet and to block the d-axis flux due to the stator current working as flux barriers [37, p. 186]. The permeability of the magnets is only approximately 5% higher in the magnets compared to air. Therefore, the permanence in the d-axis is lower than in the q-axis, and the effective air gap in the d-axis is thus longer than in the q-axis [8, p. 220], [4]. The d-axis in the IPMSM cannot attain the same amount of flux  $\psi_d$  as the q-axis  $\psi_q$ . This means that  $x_d < x_q$ . Consequently, it is possible to take advantage of the reluctance torque and the PM-produced torque. IPMSMs are the preferred choice for flux-weakening conditions over SPMSM due to the IPMSM capabilities to maintain a higher torque up to a wider speed range due to its inherent reluctance [37, p. 186], [4]. Field weakening is out of

the scope in this thesis. Field weakening is mentioned because this is an important characteristic of an IPMSM relative to an SPMSM.

The space harmonics in an IPMSM is mainly due to slotting related to rotor position  $\vartheta_r$ . While the saturation level of a IPMSM is dependent on the  $i_d$  and  $i_q$  level. The word cross coupling means that variables are dependent on the currents in the d- and q-axis with  $\psi_d(t) = \psi_d(i_d, i_q)$  and  $\psi_q(t) = \psi_q(i_d, i_q)$  [6].

### C. Coils and Phase Sequence

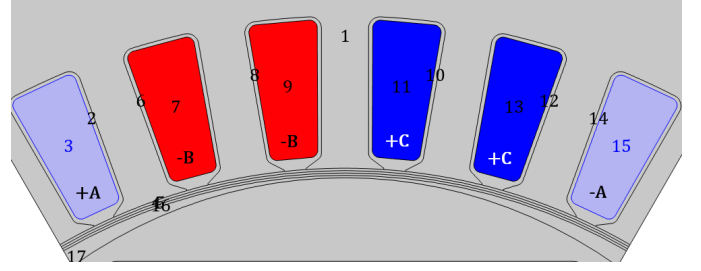
1) *Conductor Model and Group*: Now starting on the Comsol modelling theory [42]. The coil feature in **RMM** can be used to simplify the setup of the magneto-static and low-frequency electromagnetic models. It is assumed that a rated frequency of  $f_n = 50$  Hz for the IPMSM drive in this thesis is low. The coil is a **domain coil**, and not a **boundary coil**. The **Conductor model** that is used is the **Homogenized multi-turn** option in order to define a number of turns in the stator phase coils  $N_s$ . This feature enables to define  $N_s$  strands without making each individually turn physically in the Comsol model. Capacitive coupling and skin effects are omitted in the homogenized multi-turn model. The two effects are out of the scope in this thesis. Further, the current in the conductors flows only in the direction of the conductors; thus, induced eddy currents are neglected. Eddy currents are also out of the scope. Each strand in one domain is electrical isolated from the adjacent turn. The resistivity of the coils is affected by the number of turns  $N_s$  in the coil [42].

The **2D homogenized coil** have an additional setting. This is the check box called **Coil Group**. Each sub-domain in a **coil group** is representing the same cross-sectional area of the conductor [42]. This check box makes the selected domains in series. Another sub-function is also enabled with the **coil group**. The additional feature is **Reverse Current Direction**. One sub-domain in **Reverse Current Direction** can have a positive current direction, and the other sub-domains a negative current direction for the same coil. This is shown in Figure 1a and Figure 1b. In Figure 1a, domain 3 is defined with a positive current direction, and domain 15 is defined with a negative current direction. The two domains, 3 and 15, are in the same coil group. In Figure 1b both domain 7 and domain 9 is the negative phase B. When the **Coil Group** mode is activated, additional conditions are added to the model to constraint. The sum of all the voltages in the domains groups to be equal to the specified voltage in Equation 1

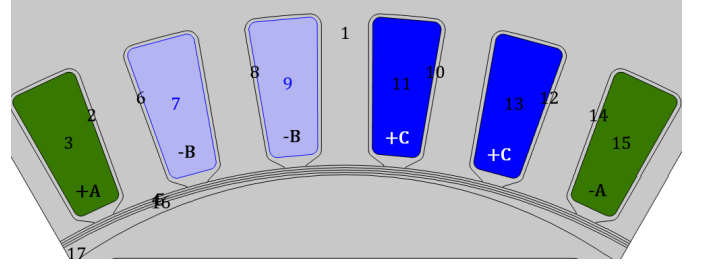
$$V_{coil} = \sum_{i=1}^{N=N_s} V_i = V_1 + V_2 + \dots + V_{N_s} \quad (1)$$

where  $V_i$  is the potential applied at the  $i$ -th conductor and  $N = N_s$  is the number of turns in that specific coil group.

2) *Coil Excitation*: After trial and error, it was determined that the coil excitation to be used in this project in the coils in **RMM** is **Coil excitation: Circuit (current)**. This connection is coupling the **RMM** physics to the external circuit **EC** with the external coupling **External I vs. U**. This modeling



(a) Coil A definitions in **RMM**. Domain 3 is negative and domain 15 is positive.



(b) Coil B definition in **RMM**. Reversed current direction in the Coil group check box due to being adjacent to phase +A.

Fig. 1: Phase definitions. Important domain numbers are on the coils.

approach worked in this thesis. It was discussed that the letter **U** in **External I vs. U** should be to the rightmost side [43].

In the Comsol setting window for the device **External I vs. U** it is written that the **external coupling device** works as a voltage source in the electrical circuit and where the electric potential  $V$  is applied as a coil voltage to (rmm/coil1). Remember, that coil1 in **RMM** have to be excited with **circuit (current)** in order to use this setting in the external circuit. The equation used in the **RMM** coils with the setting **External I vs. U** is given in Equation 2

$$\mathbf{J}_e = \frac{NI_{cir}}{A} \mathbf{e}_{coil} \quad (2)$$

It was assumed in an early phase of this thesis that **Circuit (voltage)** should be used in **RMM**. This is because the coils are voltage excited and not current excited. It is a voltage signal that is applied from Simulink to the **EC** in Comsol. This modelling technique is not used, but included because it may be interesting in further work. The **Circuit (voltage)** excitation applies the total user defined voltage over the coil  $V_{coil}$ . In this thesis that is the rated voltage  $V_{coil} = 230$  Vrms when the speed is rated  $N_n = 1000$  RPM. The voltage is lower at lower speed. Excitation of a multi-turn conducting domain gives the equation for the current density in Equation 3

$$J_e = \frac{N(V_{coil} + V_{ind})}{AR_{coil}} \quad (3)$$

where  $V_{coil}$  is the applied voltage specified by the user,  $R_{coil}$  is the total resistance of the coil calculated in Equation 4

$$R_{coil} = \int_A \frac{NL}{\sigma_{coil} a_{coil} A} \quad (4)$$

where  $L = L_s$ ,  $\sigma_{coil} a_{coil}$  is the product of the wire bulk conductivity and wire cross section and  $V_{ind}$  is the induced

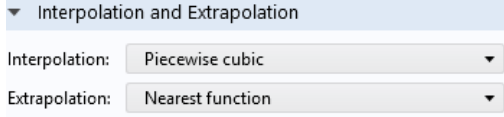


Fig. 2: Extrapolation of the steel. The settings are given by [45].

voltage calculated by integrating the electric field along the coil [42].

#### D. Boundary Conditions

It is used **anti-periodic boundary conditions** where the vector potential formulation is Amperes law described in Equation 5 [44]

$$\mathbf{A}_{src} = -\mathbf{A}_{dst} \quad (5)$$

For the **identity boundary pair** in the **sector symmetry** for the rotating domains it is also selected **antiperiodicity**. Since it is only one sector that is modelled, it is necessary to define that the number of sectors is  $n_{sect} = 6$  in **RMMs Sector Symmetry**.

#### E. Electrical Steel

In the domains with electrical steel in the rotor and stator, it is used the magnetization model: B-H curve Equation 6

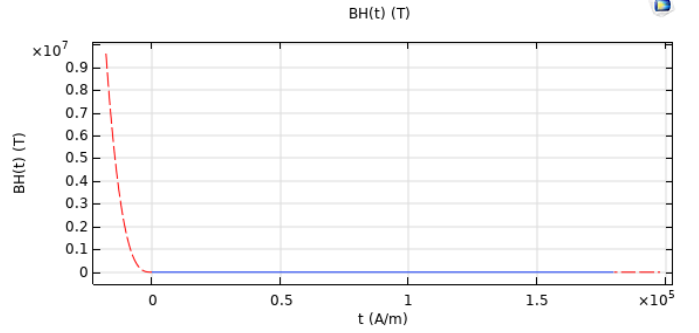
$$\mathbf{B} = f(\|\mathbf{H}\|) \frac{\mathbf{H}}{\|\mathbf{H}\|} \quad (6)$$

The material that is selected is the Silicon Steel NGO 50PN350. The number 50 is equal to the lamination thickness 0.5 mm. The number 350 is the loss per weight with the unit W/kg. This material is not specified by the manufacturer of the motor but suggested from [45]. The conductivity of the electrical steel is 10 S/m and not 0 S/m to improve the solver [35], [44]. The settings are shown in Figure 2 with the corresponding curve shown in Figure 3a. The original BH-curve is shown in Figure 3b. Further explanation about the setting of these materials is out of scope. The **Interpolation and Extrapolation**-settings of the BH-curve have to be adjusted in order to make the FEM-model converge with this NGO steel.

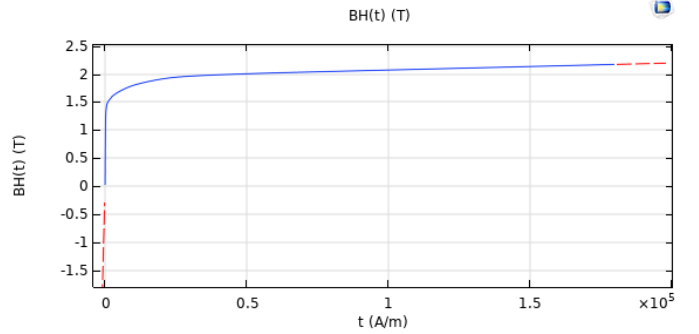
#### F. Magnet Description in Cylindrical Coordinates

The scalar remanent flux density  $B_r$  is pointing in the direction  $\mathbf{e} = [r, \varphi, z]^T = [1, 0, 0]^T$ , where the vector  $\mathbf{e}$  is a unity vector. This is the description of the north pole PM since the remanent flux density is described as a source and not a sink. Modeling of magnets is described in further detail in [35].

The remanent flux density is computed to  $B_r = 1.24$  T. It is then assumed that the magnet is of the type NdFeB and could be the material N35M with a typical remanent flux density  $B_r = 1.24$  T [46].



(a) The BH-curve after the extrapolation and interpolation settings are done.



(b) Original BH-curve without extrapolation settings and interpolation settings.

Fig. 3: Magnetic properties of the soft magnetic material.

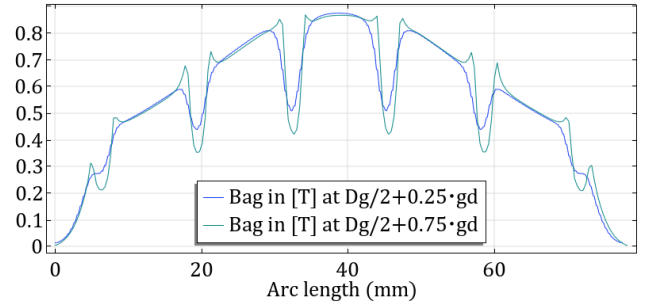


Fig. 4: Air gap flux density over  $\tau_p$  for the IPMSM used in this project.

#### G. Flux Distribution

In the LPM, it is assumed that the air gap flux density is sinusoidally distributed for the electrical parameters [8]. The air gap flux distribution  $B_{ag}$  of the machine in this report is shown in Figure 4. If a suitable pole shoe shape for embedded magnets is selected, the air gap flux density will be approximately sinusoidally distributed [36, p. 312]. The two curves are measured at different places in the air gap, thus the difference.

The flux density distribution in the ferromagnetic material in this thesis is shown in Table I. This is approximately corresponding to the expected values of a salient pole-synchronous machine that is common in *Pyrhonen et al.* [36, p. 298].

TABLE I: The flux densities during no-load nominal speed and rated current (current excited coils) nominal speed according to the theory in [36, p. 298]

Description (of maximum values)	Symbol	Value	Unit
Air gap flux density (no-load)	$B_g$	0.9000	T
Stator yoke flux density (rated load)	$B_{sy}$	1.4450	T
Tooth flux density (rated load)	$B_{st}$	1.7647	T
Rotor yoke flux density (rated load)	$B_{ry}$	1.0500	T

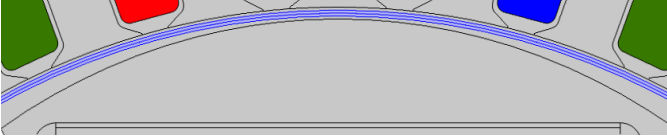


Fig. 5: The area of integration with Arkkios method. The integration is made over the complete pole shoe  $\tau_p$ .

### H. Torque

The positive rotational direction  $\omega_r$  and positive applied electromagnetic torque  $T_e$  direction is counter clockwise [42]. The standard torque calculations with Maxwell's stress tensors on the external surfaces described with Equation 7 [42]

$$\tau = \int_{d\Omega} d(\mathbf{r} - \mathbf{r}_0) \times (\mathbf{n}T)dS \quad (7)$$

It is also defined another variable name in Comsol called Arkkio's method described with the equation Equation 8 [35]

$$T_{el} = \frac{L_s}{\mu_0(r_o - r_i)} \iint_{S_{ag}} r B_r B_\varphi dS \quad (8)$$

where  $r_o$  is the outer radius  $r_i$  is the inner radius  $S_{ag}$  is the cross-sectional area of the air gap to be integrated over shown in Figure 5. The direction vector is defined as  $r = \sqrt{x^2 + y^2}$ , the radial flux direction is  $B_r = (rmm.BX \cdot X + rmm.BY \cdot Y)/r$  and the azimuthal direction is  $B_\varphi = (rmm.BX \cdot Y - rmm.BY \cdot X)/r$ .

It will also be compared the torque calculated with Arkkio's method, and the model that describes torque with flux linkages and currents [8, p. 171] with Equation 9

$$T_{dq} = \frac{3}{2}p(\Psi_{sd}I_{sq} - \Psi_{sq}I_{sd}) \quad (9)$$

The torque equation with the co-energy method's principle assumes that there are no core losses, winding losses, bearing losses, and constant temperature. In addition it is assuming no-zero sequence components [6].

Cogging torque and torque ripples will also influence the co-simulation drive. Cogging can be diminished if the rotor lamination's in a machine are displaced with skewing [47], [27]. The machine in this thesis do not consider skewing of the PMs shown in Figure 49b, Figure 49c and Figure 49a.

### I. External Circuit Star Connection

The external circuit makes it possible to control the circuit behavior of the FEM machine, which is essential to avoid circulating currents shown in section C. Using the external



(a) DC Voltage source in EC.

(b) Resistor in EC.

Fig. 6: Components in the external circuit EC.

circuit interface makes it possible to add effects like end windings, leakage inductances, and an isolated neutral resistance for the star connection. The resulting circuit layout is shown in Figure 13. The end winding inductance per phase is calculated analytically with Equation 10

$$L_w^S = \frac{2}{p} N_s \mu_0 l_w \lambda_w \quad (10)$$

where the product  $l_w \lambda_w = 2l_{ew} \lambda_{lew} + W_{ew} \lambda_{Wew}$ . It is estimated that the end winding cross section have a values corresponding to  $\lambda_{lew} = 0.297$  and  $\lambda_{Wew} = 0.232$  for a salient pole machine [36, pp. 261–262].

The resistance of the stator winding overhang  $R_{send}$  is given by [48, p. 289]

$$R_{end}^S = \rho C_u \frac{2l_w N_s}{A_{Cu}} \quad (11)$$

### J. Current Direction in External Circuit

The Comsol software is consistent in defining the positive current direction in all components. It is referred to as a *motor* reference direction for all circuit components, where the positive current direction is flowing towards the positive potential (anode). This is how all passive components are modeled in electric power engineering. However, it is common that sources are modeled with a *generator* current reference direction in electric power engineering. In a generator current direction, the positive current is flowing out from the source. Sources are modeled with a motor reference direction in Comsol. This is illustrated in Figure 6a and Figure 6b. The current direction is mentioned since this also was an obstacle and uncertainty when defining the correct input voltage direction. The **EC: Voltage source** have the settings **Source type: DC-source**. When the applied DC-battery source has a positively applied voltage drop  $\Delta U = U_{sa} - U_N > 0$  V. The current will be flowing away from the positive anode and into another component in EC. The measured current in the voltage source in the external circuit is then negative. The next part is that the same current is measured as positive in the **RMM: Coil domain**  $I_{coil}$  (since the current is flowing toward the coil).

### K. Induced EMF

According to Faraday's induction law, the electromotive force of the electrical machine is given by Equation 12

$$U_p = -\frac{d\Psi_m}{dt} = -N_s k_w \hat{\phi}_m \cos(\omega t) \quad (12)$$

where  $\Psi_m = N_s k_w \omega \hat{\phi}_{PM}$  is the induced air gap flux linkage [36, p. 300]. This relationship is important to include in the determination of the parameters from the FEM test that is outlined in section V.

#### L. Determining the Controller Parameters for an IPMSM

The flux linkages  $\Psi_d$  and  $\Psi_q$  of a IPMSM are always expressed by using the flux linkages  $\Psi_m$ ,  $L_d$  and  $L_q$ . The parameters represent the magnetic model of the motor and are obtained with different loading in the FEM software [37, pp. 188–189]. The inductance of the two axes is in general dependent on the magnitude of the stator current  $I_s$ . This is due to magnetic saturation of the core verified in Table IV.

The first step in the parameter computation is to compute the flux linkage generated by the permanent magnets  $\Psi_m$ . Computation of  $\Psi_m$  is done by setting the load current to 0 A while the motor is running at nominal speed 1000 RPM. This is known as the no-load test [37, p. 188]. In this test, it is used the **Current Source** in **EC** to make a model of the open circuit. This setting is not used for any co-simulations. The flux linkage of the PMs  $\Psi_m$  is the average value obtained from the test and is considered to be independent of any current loading.

The second step in the parameter computation is to run two separate tests with a 10% stator current. This is to avoid saturation of the metal and assume linear regions of the ferromagnetic material. In the first test run with a current  $10\%I_d$  and  $I_q = 0$ . Then the d-axis inductance can be calculated with Equation 13

$$L_d = \frac{\Psi_m - \Psi_d}{I_d} \quad (13)$$

For the third test, it is used a 10%  $I_q$  current and  $I_d = 0$  A to obtain the unsaturated q-axis inductance Equation 14

$$L_q = \frac{\Psi_q}{I_q} \quad (14)$$

The d- and q -axis calculations can be obtained by the flux linkages  $\Psi_{sa}$ ,  $\Psi_{sb}$  and  $\Psi_{sc}$  computed by Comsol in an built in variable. The flux linkages are transformed into the d- and q-axis with variables defined in Comsol by Equation 15 and Equation 16, respectively [37, p. 155]

$$\Psi_d = \frac{2}{3} [\Psi_a \cos(\vartheta) + \Psi_b \cos(\vartheta - \frac{2\pi}{3}) + \Psi_c \cos(\vartheta + \frac{2\pi}{3})] \quad (15)$$

$$\Psi_q = -\frac{2}{3} [\Psi_a \sin(\vartheta) + \Psi_b \sin(\vartheta - \frac{2\pi}{3}) + \Psi_c \sin(\vartheta + \frac{2\pi}{3})] \quad (16)$$

### III. THEORY - CONTROL OF AN IPMSM

#### A. Introduction

Control strategies used in this thesis is the same as in the chapter about PMSM and IPMSM in the electric drive course at NTNU [8]. The stationary operating characteristics and control strategies of an IPMSM are used to select the overall control of an IPMSM.

1) *Space Vector of IPMSM*: The IPMSM have two independent control signals  $u_d$  and  $u_q$ . The rotational induced voltage is the back EMF voltage  $u_p = jn\psi_m$ . The rotationally induced voltage lies only in the q-axis. It is optimal to operate with a negative d-axis component for an IPMSM to take advantage of the reluctance torque [4],[39]. In the rotating flux-oriented dq-reference frame, the d-axis is aligned with the rotating flux produced by the rotor's magnets. The knowledge of the rotor position is very important [4]. The alignment of the phase sequence and d-axis for the motor in this thesis is shown in Figure 8. For an PMSM the mechanical speed is  $\Omega_n = \omega_n/p$ . In this work, it will be utilized drive control with a position sensor. Sensorless control has been done for co-simulation before in reference [13] but not with LiveLink for Simulink. Sensorless-control, which is using estimation techniques to locate the rotor position, is out of the scope in this thesis [49],[50].

2) *Transformations*: The space vectors in this thesis is in the dq-reference frame with the standard Park-Clarke transformation [51]. It is further assumed that the three-phase currents are balanced and that there is no zero-sequence-currents  $i_0 = 0$  p.u. given by Equation 17

$$i_0 = \frac{i_a + i_b + i_c}{3} = 0 \quad (17)$$

The Clarke transformation is given by Equation 18

$$\begin{bmatrix} i_\alpha \\ i_\beta \end{bmatrix} = \frac{2}{3} \begin{bmatrix} 1 & -1/2 & -1/2 \\ 0 & \sqrt{3}/2 & \sqrt{3}/2 \end{bmatrix} \begin{bmatrix} i_a \\ i_b \\ i_c \end{bmatrix} \quad (18)$$

The Park transformation is given by Equation 19

$$\begin{bmatrix} i_d \\ i_q \end{bmatrix} = \begin{bmatrix} \cos \vartheta & \sin \vartheta \\ -\sin \vartheta & \cos \vartheta \end{bmatrix} \begin{bmatrix} i_\alpha \\ i_\beta \end{bmatrix} \quad (19)$$

The same procedure can be used for the flux linkages and voltages in Simulink.

The inverse Park transformation is given by Equation 20 and Equation 21

$$i_\alpha = i_d \cdot \cos(\vartheta) - i_q \cdot \sin(\vartheta) \quad (20)$$

$$i_\beta = i_d \cdot \sin(\vartheta) + i_q \cdot \cos(\vartheta) \quad (21)$$

The inverse Clarke transformation is given by Equation 22, Equation 23 and Equation 24

$$i_a = i_\alpha \quad (22)$$

$$i_b = -\frac{1}{2}i_\alpha + \frac{\sqrt{3}}{2}i_\beta \quad (23)$$

$$i_c = -\frac{1}{2}i_\alpha - \frac{\sqrt{3}}{2}i_\beta \quad (24)$$

3) *Basis Values and Per Unit Values:* The base current is given by [8, p. 224]. Equation 25.

$$I_{s,basis} = \hat{I}_n \quad (25)$$

where  $\hat{I}_n$  is the peak rated nameplate current. The basis voltage is given by Equation 26

$$U_{s,basis} = \hat{U}_n \quad (26)$$

where  $\hat{U}_n$  is the peak rated nameplate voltage. The flux linkage basis is given by Equation 27

$$\Psi_{s,basis} = \frac{\hat{U}_n}{\omega_n} = \frac{\hat{U}_n}{2\pi f_n} \quad (27)$$

where  $f_n$  is the rated electric frequency in Hz. The base power is given by Equation 28

$$S_n = \frac{3}{2} \cdot \hat{U}_n \cdot \hat{I}_n \quad (28)$$

The torque basis is given by Equation 29

$$T_{basis} = \frac{S_n}{\Omega_n} = \frac{3}{2} \cdot p \cdot \frac{\hat{U}_n}{\omega_n} \cdot \hat{I}_n = \frac{3}{2} \cdot p \cdot \Psi_n \cdot \hat{I}_n \quad (29)$$

where  $\Omega_n = \omega_n/p$ . The impedance basis value is given by Equation 30

$$Z_{s,basis} = \frac{\hat{U}_n}{\hat{I}_n} \text{ and } L_{s,basis} = \frac{\hat{U}_n}{\omega_n \hat{I}_n} \quad (30)$$

The per unit reactance value is given by Equation 31

$$x_s = \frac{\omega_n \cdot L_s}{Z_{s,basis}} = \frac{X_s}{Z_{s,basis}} \quad (31)$$

The time constant for the mechanical system is given by Equation 32

$$T_m = \frac{J \cdot \Omega_n^2}{S_{basis}} \quad (32)$$

4) *Power Electronics Model:* It is modelled a power electronic converter with a first order time delay  $T_{delay}$ . In previous work it have been used an ideal SVPWM switching scheme in co-simulations [18],[19],[20],[25]. SVPWM cause less THD compared to SPWM [24]. Some previous co-simulation work have used a linearized converter model with a first order  $T_{delay}$  [28].

5) *MTPA and Mechanical Model:* The equations in this subsection is from the well-know idealized model assuming no higher order non-linear effects that [6]. While in reality the state variables will be dependent on rotor position  $\vartheta_m$ ,  $i_d$  and  $i_q$  which can be obtained from a FEA model [6]. The flux linkages of the machine are decomposed into the following three terms Equation 33

$$\begin{aligned} \psi_d &= x_d \cdot i_d + \psi_m \\ \psi_q &= x_q \cdot i_q \\ \psi_m &= x_{md} \cdot i_m \end{aligned} \quad (33)$$

It is indicated in the last flux-linkage term that the PMs only produce a d-axis component. The per unit electromagnetic

torque in the LPM model of the machine is described with Equation 34

$$\tau_e = \psi_m \cdot i_q - (x_q - x_d) \cdot i_d \cdot i_q \quad (34)$$

An IPMSM have a saliency ratio  $x_q > x_d$ . This means that for the machine to produce a positive torque, the largest current component have to be a positive  $i_q$ . From Equation 34 the reluctance component is  $\tau_T = -(x_q - x_d) i_d i_q$ . The current  $i_d$  have to be negative to utilize this torque component and operate in the 2<sup>nd</sup> quadrant in the dq-plane [8, p. 224]. The optimal torque condition is obtain by taking the partial derivative of the torque with respect to the torque of Equation 35 [8, p. 234], [52]

$$\frac{\partial}{\partial i_q} \tau_e = \psi_m + (x_q - x_d) \frac{i_s^2 - 2i_q^2}{\sqrt{i_s^2 - i_q^2}} = 0 \quad (35)$$

have to be full filled. The stator current magnitude is given by Equation 36

$$i_s = \sqrt{i_d^2 + i_q^2} \quad (36)$$

The torque equation for maximum torque is expressed as a 4<sup>th</sup> order polynomial that can be reduced to a 3<sup>rd</sup> order polynomial in Equation 37 [8, p. 233],[52]

$$i_{dref}(\tau_{eref}) = \frac{\frac{\psi_m}{3} - \sqrt{\left(\frac{\psi_m}{3}\right)^3 + \frac{(x_q - x_d)^2 \tau_{eref}^2}{3\psi_m}}}{x_q - x_d} \quad (37)$$

The optimal q-axis current is described as a function of the torque reference and the d-axis current in Equation 38

$$i_{qref}(\tau_{eref}, i_{dref}) = \frac{\tau_{eref}}{\psi_m - (x_q - x_d) i_{dref}} \quad (38)$$

In this thesis the load model is only given in SI-units. The torque balance for the SI unit load is given by Equation 39

$$\frac{d\omega_n}{dt} = \frac{1}{J}(T_e - T_L) = \frac{1}{J}(T_e - k_L \cdot \omega_r^2) \quad (39)$$

where the load disturbance is dependent on the rotor speed and the load constant  $k_L = 0.0028$ . The the position is also a state variable that is the integrator of the speed Equation 40

$$\frac{d\vartheta}{dt} = p \cdot \omega_r \quad (40)$$

## B. Control Theory

The resonance frequency is denoted  $\omega_0$ . For a system with a damping  $\zeta \approx 0.707$  the crossover-frequency  $\omega_{ca} = \omega_0$ . The phase gain of the open-loop system should be  $\Delta K = |h_0(j\omega_{180})|[\text{dB}] \approx 6 \text{ dB}$  and the phase margin  $\psi = \angle h_0(j\omega_{0\text{dB}}) \approx 45^\circ$ . It will be performed a frequency analysis with Bode plots of the whole system. It will also be performed a stability analysis with the Nyquist stability diagram [38].

### C. Torque and Current Controllers - Modulus Optimum Control

For power, electronic converters systems, the internal reduction of the block diagrams often ends up with one dominant time constant, which is  $T_d$  and  $T_q$  for an IPMSM, and one or several small time constants which are described as one single time constant  $T_{sum}$  [8, p. 103]. The theoretical requirements for modulus optimum control is that:

- 1) The relative damping is  $\zeta = 1/\sqrt{2} \approx 0.707$ .
- 2) The large time constant for the integral time constant in the PI-controller  $T_I$  is equal to the electrical constant of the machine  $T_d$  or  $T_q$  to obtain a pole cancellation.
- 3) The crossover-frequency  $\omega_{c,a}$  is equal to the resonant frequency  $\omega_0 = 1/\sqrt{2}T_{sum}$  for the closed loop system  $M(s)$ .
- 4) The time to reach a step reference of  $\tau_{eref} = 1$  pu should have a rise time  $T_{rise} = 4.7T_{sum}$ .
- 5) For the same reference the overshoot should be 4.7% while the error is in withing the limit of  $\pm 2\%$  after a settling time  $T_{settling} = 8.4T_{sum}$  when applying a step reference.

The equations in this subsection describes the LPM description of the IPMSM. The d-axis and q-axis controlled voltages is given by Equation 41 and Equation 42, respectively.

$$u_d = r_s \cdot i_d + \frac{1}{\omega_n} \cdot \frac{d\psi_d}{dt} - n \cdot \psi_q \quad (41)$$

$$u_q = r_s \cdot i_q + \frac{1}{\omega_n} \cdot \frac{d\psi_q}{dt} + n \cdot \psi_d \quad (42)$$

From observing the dynamic state model in Equation 41 and Equation 42 of the IPMSM the d- and q-axis are coupled. This is shown in the rearranged the equations to Equation 43 and Equation 44

$$\frac{x_d}{\omega_n} \cdot \frac{di_d}{dt} = -r_s \cdot i_d + n \cdot x_q \cdot i_q + u_d \quad (43)$$

$$\frac{x_q}{\omega_n} \cdot \frac{di_q}{dt} = -r_s \cdot i_q - n \cdot x_d \cdot i_d - n \cdot \psi_m + u_q \quad (44)$$

The control voltages are thus divided into to components  $u_d = u_{dI} + u_{dII}$  and  $u_q = u_{qI} + u_{qII}$ . The terms  $u_{dI}$  and  $u_{qI}$  are the controlled signals by the PI-controllers. The terms  $u_{dII}$  and  $u_{qII}$  are the nonlinear feed-forward compensation and decoupling terms. The decoupling terms are calculated with Equation 45 and Equation 46

$$u_{dII} = -n \cdot x_q \cdot i_q \quad (45)$$

$$u_{qII} = n \cdot x_d \cdot i_d + n \cdot \psi_m \quad (46)$$

The controllable terms for the PI-controllers are then reduced to Equation 47 and Equation 48

$$\frac{di_d}{dt} = -\frac{\omega_n r_s}{x_d} i_d + \frac{\omega_n}{x_d} u_{dI} \quad (47)$$

$$\frac{di_q}{dt} = -\frac{\omega_n r_s}{x_q} i_q + \frac{\omega_n}{x_q} u_{qI} \quad (48)$$

where the time constants are  $T_d = x_d/(\omega_n r_s)$  and  $T_q = x_q/(\omega_n r_s)$ . It is now obtained two first order systems, where there is obtain a decoupling between the d- and q-axis in the unsaturated region assuming an ideal model [38]. When designing the controllers the time delays in the controllers, inverter and the filters need to be included. It is used dq-oriented controllers considering analogue techniques, derived in the continuous systems. The average time delay of a power inverter is  $T_{delay} = T_{sw}/3$  [8, p. 244]. The gains of the current controllers are calculated with Equation 49 and Equation 50

$$K_{pd} = \frac{x_d}{2\omega_n(T_{delay} + T_{fd})} \quad (49)$$

$$K_{pq} = \frac{x_q}{2\omega_n(T_{delay} + T_{fq})} \quad (50)$$

The open loop transfer function for two axes at zero-speed is written with the parameters obtained with the  $L_{d1}$ -parameter in Table V as Equation 51 and Equation 52

$$h_{oid}(s) \approx K_{pd} \frac{1 + T_{i,d}s}{T_{i,d}s} \frac{\omega_n T_d}{x_d(1 + T_d s)(1 + T_{sum} s)} \quad (51)$$

$$h_{oid}(s) = \frac{1 + 0.0123s}{0.0123s} \frac{0.47 \cdot 314 \cdot 0.0123}{0.158(1 + 0.0123s)(1 + 5.33 \cdot 10^{-4}s)}$$

$$h_{oiq}(s) \approx K_{pq} \frac{1 + T_{i,q}s}{T_{i,q}s} \frac{\omega_n T_q}{x_q(1 + T_q s)(1 + T_{sum} s)} \quad (52)$$

$$h_{oiq}(s) = \frac{1 + 0.0279s}{0.0279s} \frac{1.07 \cdot 314 \cdot 0.0279}{0.358(1 + 0.0279s)(1 + 5.33 \cdot 10^{-4}s)}$$

where  $T_{sum} = T_{delay} + T_{fd}$  and  $T_{fd} = T_{fq}$  for a PMSM and an IPMSM. Here it is divided  $u_{DC}/u_{DC}$  to make the controller parameters independent of the DC-bus voltage. The filters should be selected such that the ripple in the controlled voltages is in the range of only 5% – 8% for an LPM (fundamental wave model) motor. However, the verification of this statement is not considered in this thesis. The FEM motor has inherently higher-order space harmonics in the torque and current waveforms due to slotting, rotor topology, and the pole shoe shape of the machine. This is verified in subsection VII-J. The filtering techniques are used with common practice and are considering harmonic components from the converter and not the machine. The difference between spatial harmonics in the machine and converter is important to distinguish.

Tuning, design, and verification of the PI-controllers in the inner loop and the outer loop is done with the LPM Matlab/Simulink model due to the considerable reduction of computational time compared to FEM co-simulation [19], [18]. This is also the case for the load cases used in this thesis.

### D. Cross-Coupling and Saturation

In *Schulte et al.* [26] it is readily verified that cross-couplings effect causes overshoot and undershoot in the transient periods. This was verified through co-simulation and corresponding with measured lab data. It was also observed in [27, p. 440] that the segmented machine and unsegmented

co-simulated machine have a similar response with torque and current ripples, which also corresponds well to the measured real machine compared. However, the fundamental wave model is also compared in this work with the FEM model. In *Di Leonardo et al.* [25] it is also mentioned that the steady-state deviation from the rated speed is  $-6\%$  with what is referred to as detuning base on the constant parameter parameters. In [6] it is generated LUT that is considering space harmonics from the rotor position and saturation with different current loading in an IPMSM model. Reference [6] is not utilizing co-simulations.

### E. Speed Control Symmetrical Optimum

It is used symmetrical optimum where  $\beta = 4$  for the tuning of the speed controllers [8, p. 252]. The open loop transfer function with the speed controller is described with the parameters listen in Table V with Equation 53

$$h_{0,n}(s) = K_{p,n} \cdot \frac{1 + T_{i,n} \cdot s}{T_{i,n} \cdot s} \cdot \frac{1}{T_m \cdot s \cdot (1 + T_{sum,n} \cdot s)} \quad (53)$$

$$h_{0,n}(s) = \frac{1 + 0.0123 \cdot s}{0.0123 \cdot s^2} \frac{14.1915}{0.087 \cdot (1 + 0.0031 \cdot s)}$$

where  $T_{sum,n} = 2 \cdot T_{sum,i} + T_{f,n} = T_{eq,i} + T_{f,n}$ . The gain is calculated with Equation 54

$$K_{p,n} = \frac{T_m}{\sqrt{\beta} \cdot T_{sum,n}} \quad (54)$$

The PI current controller time constant is calculated with Equation 55

$$T_{i,n} = \beta \cdot T_{sum,n}. \quad (55)$$

## IV. THEORY - CO-SIMULATION

### A. General

This subsection is giving insight into the general concept behind co-simulations. The idea of co-simulation is to integrate loosely coupled stand-alone subsystems with each other. Co-simulation utilizes the exchange of data between each independent, stand-alone system. Co-simulation can also make it convenient to hide internal dynamics and protect sensitive information, which is attractive for the industry. Co-simulation enables a holistic system simulation [31].

Each sub-software time integration is assumed to be independent in between each discrete *communication points*  $t_i \in \{t_0, t_1, \dots, t_N\}$  [31]. The exchange of data between each stand-alone system is only happening at time these times in general [31] also for LiveLink [53]. The mathematical description between each subsystem coupling variables is given by Equation 56

$$\mathbf{u}(t_i) = \mathbf{C}\mathbf{y}(t_i) \quad (56)$$

where  $\mathbf{C}$  is the connection graph matrix and related to the input  $\mathbf{u}$  from Simulink to Comsol and the outputs between Comsol and Simulink  $\mathbf{y}$ . In [31], the connection graph matrix is denoted  $\mathbf{L}$ . This notation is used to describe the inductance matrix [8]. Also  $\mathbf{C}$  stands for *connection*. The communication

time step happens at a rate of the *macro time step* called *communication time step* in LiveLink. In this thesis the communication time step is denoted  $\Delta t_i = 1 \cdot 10^{-4}$  in Simulink, with an equivalently defined parameter  $dt = 1 \cdot 10^{-4}$  in Comsol. The next time step in the co-simulation is denoted  $t_{i+1} = t_i + \Delta t_i$ . It is not given that each stand-alone system performs as desired. Correct time stepping and data exchange are important tasks to consider, and effective communication time between each stand-alone calls for adequate understanding of the software architecture. The advice is to select coupling method and  $\Delta t_i$  with caution.

### B. Time Stepping

It is unknown to Comsol what Simulink is computing in between each communication point. It is also unknown to Simulink what Comsol is solving in between communication steps. Hence, the time step needs to be approximated and constant within limited time intervals. This is a trade-off between computational time, accuracy, and stability of the solvers [31]. For users of power electronic converters, the accuracy of the converter design has to be reduced [25]. In [28] the converter was reduced into an equivalent first-order transfer function with an equivalent  $T_{delay}$  to minimize the computational time [28]. In [20] it was used ideal switching, but it is feasible to include dead time and blanking effects from the transistors. In [22] it is stated that a proper mesh should be utilized for accuracy, but at the same time, the computational time can take up to several hours.

It is pointed out by several authors that one should select a suitable timestep before the co-simulation [24],[25]. In [24] it was included a SVPWM. The switching period was  $T_{sw} = 0.0001$  s, and the selected co-simulation time step is  $1/10^{th}$  of that  $\Delta t_i = 0.00001$  s. This value was obtained by trial and error with several experiments. In the SINTEF report about co-simulation *Sadjina et al.* [31], it is remarked that the macro time steps for linear systems (like the LPM) can be selected from their eigenfrequencies, but for non-linear systems like FEM, it "may be very difficult to find a good choice."

### C. Softwares, Standards, Functional Mock-up Unit

The FMI standard allows subsystems to be binary compatible with each other. This is the case for the LiveLink for Simulink code. The FMI is a standard, with the first version published in 2010. It is assumed that the LiveLink co-simulation block uses a low-level interface since the FMU block does not discriminate if it is the unit V or the unit A that is applied at  $\mathbf{u}$  or  $\mathbf{y}$ . On the other hand, a high-level interface discriminates between the units [31].

## V. METHOD - FEM MODELLING

### A. Introduction

*This chapter is describing how the co-simulation is set up from the Comsol Desktop side. Several modeling techniques were applied in this thesis to converge on sufficient communication between Comsol and Simulink. This section describes the coupling of the finite element model used in this thesis*



for all the co-simulation results. The machine design and definitions in Comsol was an extensive aspect to set up for co-simulation.

### B. Reverse Engineering

The motor used in this project is reverse engineered from the laboratory at NTNU. The motor was opened and taken geometric measurements with the parameters in Table X. The material, winding layout, turn number, and the remanent flux density  $B_r = 1.24$  T were used to obtain the parameters listed in Table II. The stator is a single layer and distributed winding machine with  $Q_s = 36$ ,  $p = 3$ ,  $m = 3$  and  $q_s = 2$ . The magnetization pattern is radial. This can be verified by looking at Figure 8. The coils between each pole pitch  $\tau_p$  are series-connected and no parallel paths in the stator windings. The materials used in this project co-simulation is given in Table III.

TABLE II: Datasheet of the machine

Description	Symbol	Value	Unit
Output power	$P_{out}$	314	kW   hp
Full load torque	$T_{mech}$	28.70	Nm
Inertia	$J_{rotor}$	0.027	kgm <sup>2</sup>
Line voltage	$V_{LL}$	400	V <sub>RMS</sub>
Phase voltage	$V_n$	230	V <sub>RMS</sub>
Rated speed	$n_s$	1000	RPM
Full load current	$I_n$	4.930	A
d-axis inductance	$L_{d2}$	30.803	mH
q-axis inductance	$L_{q2}$	56.611	mH
Saliency ratio	$L_q/L_d$	1.838	pu
Phase EMF at $N_n$	$k_e = 2\pi f_n \Psi_m$	214.1	V <sub>RMS</sub> /krpm
Flux linkage from PM	$\Psi_m$	0.96355	Wb
Measured in Comsol	$R_{coil}$	1.89	$\Omega$

TABLE III: Material properties used in this project.

Description	Symbol	Value	Unit
Remanent flux density	$\bar{B}_r$	1.24	T
Conductivity of PM	$\sigma_{PM}$	$7.14 \cdot 10^5$	S/m
Conductivity of copper	$\sigma_{Cu}$	$5.99 \cdot 10^7$	S/m
Conductivity of 50NGO350 steel	$\sigma_{Fe}$	10.00	S/m

The physics and material settings used in the Comsol Desktop model are shown in Figure 7. The material list is given in Table III. It is used two different materials settings for the electrical steel in the stator and the rotor. This is because it is set an electrical conductivity in the stator as  $\sigma_{stator} = 10$  S/m, and electrical conductivity in the rotor steel of  $\sigma_{rotor} = 1000$  S/m for some simulations. The conductivity in the rotor is 1000 S/m to emulate a damper winding in some FEM simulations. This conductivity was used when the machine was designed to fit the given parameters from the datasheet. This setting was used when it was applied a rated voltage at the terminals in synchronous speed to reduce the transient period of the torque and the current indicated in Figure 53a. However, for every co-simulations depicted in this thesis the conductivity is  $\sigma_{rotor} = 10$  S/m. This is to avoid a damper winding effect in the drive simulations [43].

### C. Coils and Phase Sequence

The coils are defined as it is described in section II. It is built one sector for the field solution to reduce computational

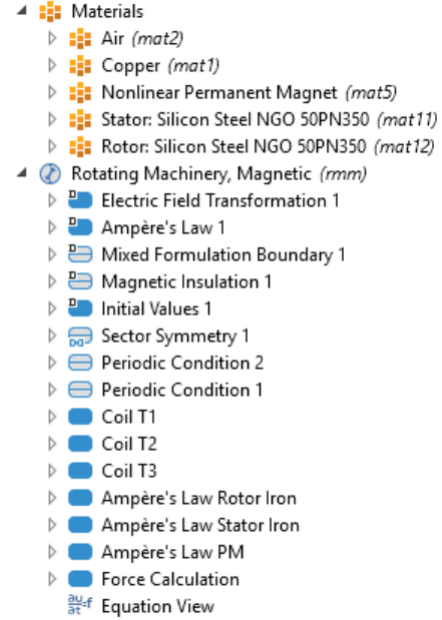


Fig. 7: Physics and material list used in the co-simulation model. It is used the additional **reverse current direction** setting in Phase A (T1) and Phase B (T2), but not in Phase C (T3).

time and cost and reduce finite elements. At the same time, it is a compromise between the number of elements and accuracy [35]. In this thesis, it is required that the sector is working as the expected whole machine. This is because the excitation mechanism is a voltage supply, not a current supply. A too-short coil length will result in a partially "short circuit." The number of coil turns are  $N_{coil} = 50$  to attain the correct back EMF from the specifications in no-load mode, and the correct applied terminal voltage. The sector number  $n_{sect} = 2 \cdot p = 6$ . The windings are a series winding (no parallel paths) the machine length  $d$  in the settings for RMM under **Thickness: Out-of-plane thickness** is multiplied with the number of sectors  $d = n_{sect} L_s = 2p L_s = 2 \cdot 3 \cdot 80.0$  mm = 484.8 mm. This is the active length per coil without the end windings. This is possible to do for this machine since the windings are series-connected. For other machines, it has to be considered how the winding layout is.

For all the coil domains, it is defined coil groups and selected **homogenized multi-turn coils** to include the number of turn in each phase coil  $N_{coil} = 50$ . It is also used the feature **coil group** to be able to select the sub-domain **reverse current direction** where this is needed [35]. This is indicated in Figure 8. When a positive voltage is applied to the voltage parameter  $U_{sa} > 0$  V, the current in coil domain  $-A$  will have a negative current density value  $J_z$  in A/mm<sup>2</sup>.

It is experienced - after several simulations and troubleshooting - that it is extremely important that phase A is aligned properly with the d-axis. The importance of this can not be emphasized enough or overstated. The alignment used for all the results in section VII is shown in Figure 8. It is mentioned that it is important to know the rotor position when applying vector control in section II [36]. A description of a

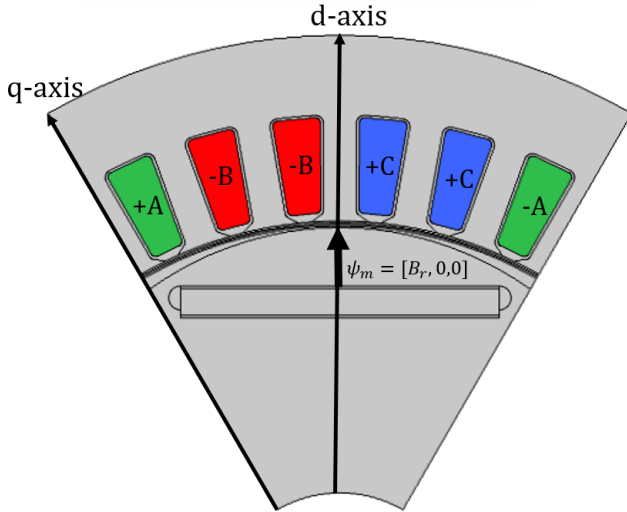
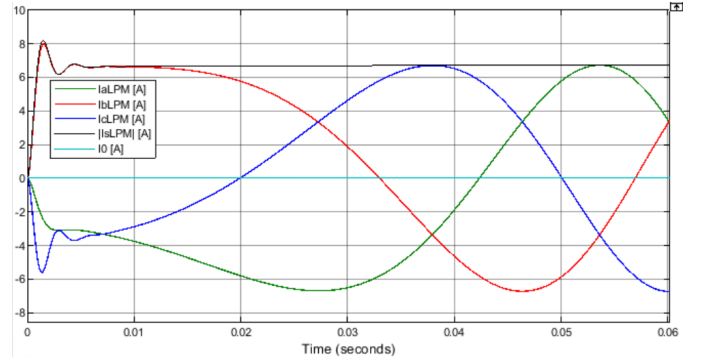


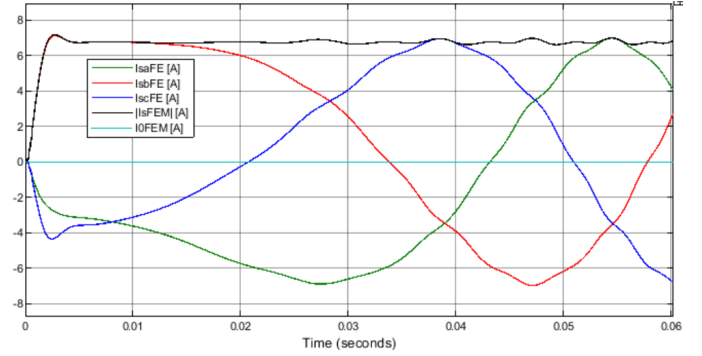
Fig. 8: In order for phase A to be aligned with the d-axis at start (standstill) with respect to the vector of the remanent flux density of the north pole of the PM  $B_r$ . The rotation is counter-clockwise for a positive applied torque in Simulink.

FEM PMSG alignment for co-simulation can also be found in [7, pp. 70–71], although the phase sequence is not included on those pages. The phase sequence directions for the three coil groups  $a$ ,  $b$  and  $c$  are defined as depicted in Figure 8. This was the last problem solved out of several before it was possible to run a co-simulation experiment that worked on the date 18<sup>th</sup> of April 2021.

The phase sequence was properly set by trial and error after several simulations, with a combination of the physical understanding of how the d- and q-axis can be determined by looking into the FEA model using the bi-directional interface from LiveLink for Simulink. The correct rotor position was at this stage determined by comparing the initial current waves in the regular LPM simulations with the FEM co-simulation model in Figure 9a and Figure 9b, respectively. The applied current signals can almost be described as DC currents when the motor is just starting at  $\omega_r \approx 0$  rad/s. It is applied a torque reference signal with MTPA  $\tau_{eref}$  pu. The load torque disturbance was  $\tau_L = 0$  pu for the correct rotor position. The exact equal control parameters were used for the LPM and FEM co-simulation comparison. The controllers are in pu-reference, and the LPM motor is also in pu-values. The comparison is  $I_b \approx 8$  A with a descending trend, phase  $I_a \approx -3$  A with a descending trend, and  $I_c \approx -5$  A with an ascending trend. Remember that a motor rotor reference frame is used, where the q-axis is leading the d-axis by  $90^\circ$  electrically. It is the rotor position in Comsol that has to be aligned properly with the phases depicted in Figure 9b, obtained with the setup in Figure 8. The corresponding voltage plots are shown in Figure 10a and Figure 10b respectively. There are some differences in the transients at the start between co-simulation and LiveLink.



(a) DC-current inception for the LPM motor.



(b) DC-current inception from the FEA LiveLink simulation.

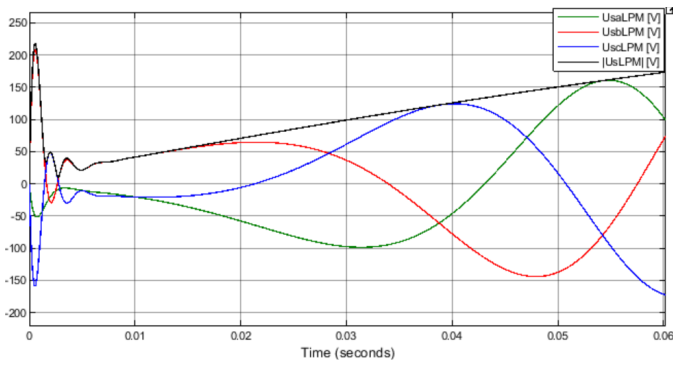
Fig. 9: Three-phase currents.

#### D. Moving Mesh Rotating Domain

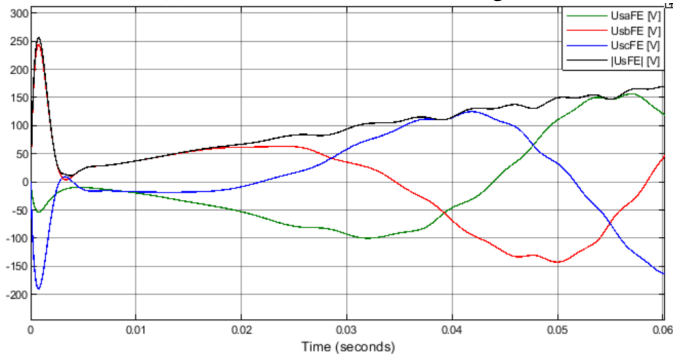
1) *General Angular Velocity*: It is used one **rotating domain** for all the sectors that are in the rotor. It is four air gap lines. Two air gap line domains belong to the rotor, and two air gap lines belong to the stator, indicated in Figure 5.

The co-simulation input parameter from Simulink to Comsol is named  $\omega_r$  in this thesis. This input parameter is defined in the section where the rotating domain is placed shown in Figure 11a.

Comsol has several options in the setting of the **Rotating Domain**. In this thesis, it is used **Rotation type: Specified rotational velocity** and other settings **Rotational angular expression: General angular velocity**. When this option is selected, Comsol assumes that the angular velocity value that is defined by the user  $\omega_r$  is in the unit rad/s. The counterpart to this is if it is selected **Rotational angular expression: Constant angular velocity**. The last-mentioned option is **NOT** used. The equation view of the two mentioned settings is shown in Figure 11b and Figure 11c. Here it is clear that the setting Figure 11c have the factor  $2 \cdot \pi$  defined in addition and hence not used because the feedback speed to Comsol will be  $2\pi$  higher value than what is calculated by the load in Simulink. That will yield a large and incorrect error. Although, Comsol usually recommends using the constant angular velocity settings [44]. The decision to use the general rotating mesh setting may seem like a trivial and logical problem. It is not, and an amount of effort was made to make this definition clear. Remember that this is a modeling problem that is on top of many other new definitions. It is not clear to understand the



(a) Start transient of the DC-voltage.



(b) Start transient of the DC-voltage from the LiveLink simulation.

Fig. 10: Three-phase voltages.

logic and user-friendliness behind the constant angular velocity term defined in Comsol. The constant angular velocity is actually less user-friendly, by experience. The Comsol function **Equation view** had to be used extensively to get to the root of the problem. By experience and troubleshooting in this project, it is clear that the mechanical model in Simulink is calculating  $\Omega_n$  in the unit rad/s and not the frequency  $\Omega_n/(2\pi)$  in 1/s. This unit conversion was an issue that needed to be solved to ensure a 1:1-ratio between Comsol and Simulink in speed and position.

To be clear: Simulink is calculating the speed in [rad/s]. When **General angular velocity** is used, the rotor speed with the unit [rad/s] from Simulink is multiplied, in Comsol, with the factor 1 instead of the factor  $2\pi$ .

2) *Position Integration*: Note that it is the speed that is the feedback variable from Simulink to Comsol. For motor drives applications, it is also required to know the position. A discussion has been if the integration for the position  $\vartheta/p$  should be done in Comsol or Simulink. From trial, it is experienced that the integration from speed to position should be done in Simulink. The co-simulation was even slower with position integration in Comsol. However, this problem can be investigated in a later project.

The reason is probably since the load model is defined in Simulink. This means that the integration from Arkkio's torque  $T_e$  to rotor speed  $\Omega$  is done in Simulink, by Newton's 2<sup>nd</sup> law for rotational force and should also continue the integration to position in Simulink.

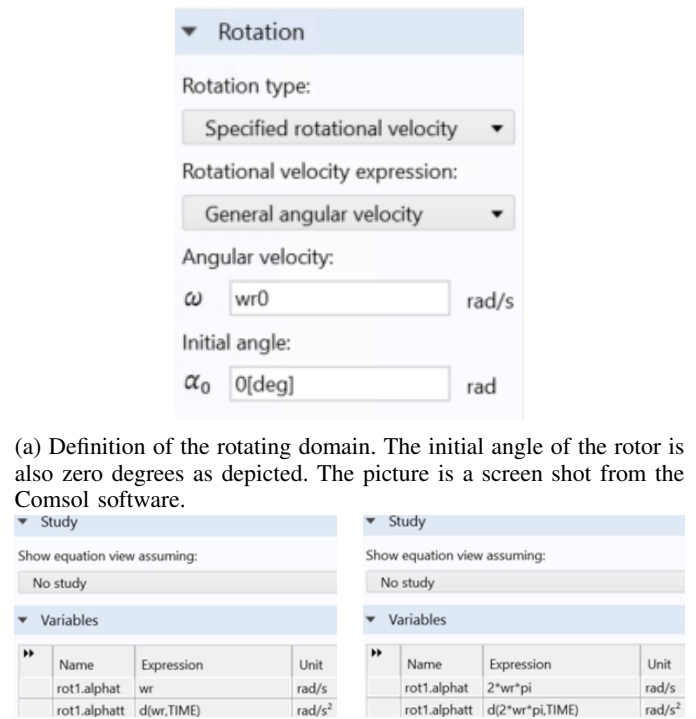


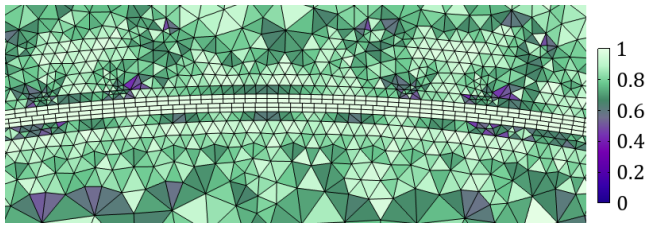
Fig. 11: Rotating domain settings.

### E. Mesh Refinement

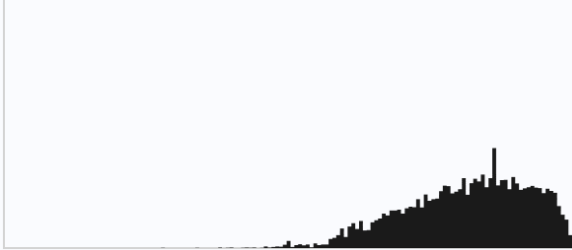
A part of the troubleshooting process was to adjust the mesh. It was assumed that an ill-conditioned mesh could be a potential convergence problem. The main focus was on having an accurate and roughly symmetrical mesh in the air gap but also other parts of the machine like the slots  $b_{su}$ , the teeth  $b_{st}$ , in the **coil domains** and other curved **domains** [35]. The mesh in the machine in *Kanerva* [33] appears to be very symmetric and evenly distributed. In this thesis, some of the elements on the rotating side are smaller than on the stationary side, and the total mesh is not as symmetrical but assumed sufficient [44]. The skewness of the elements is in the higher range scale 0.0 to 1.0, where 1.0 is the highest Figure 12a. The two middle layers of the air gap are assumed to be most important and hence concentrated most to get a sufficient mesh. It was also used several edge refinements and mapped elements techniques. In the stator yoke and the pole shoe, it was for instance, used coarser elements. A fraction of the elements are in the lower range shown in the skewness statistics of the mesh Figure 12b. The number of elements is 11830, the minimum element quality is 0.2799, and the average element quality is 0.8222 from Comsol Desktop mesh statistics.

### F. External Circuit

It is possible to apply co-simulation voltages from Simulink directly to the **RMM: Coils**. Directly applying voltages to the **RMM**-coils, without making the **EC** isolated neutral, are



(a) Mesh skewness factor.



(b) Skewness mesh statistics.

Fig. 12: Mesh in Comsol.

causing circulating currents shown in section C. This issue was also extensively addressed in the FEM-modelling phase. Neglecting the **EC** modeling with the isolated neutral point, will cause three separate circuits. One circuit for each coil. When the **RMM: Coils** are used, the connection can be viewed as three-separate coils, or the connection can be viewed as a star-connected machine with a grounded neutral point  $R_N = 0 \Omega$ . Several simulations with connecting the **RMM: Coils** directly to LiveLink was done. The results were that there were circulating currents in the machine when a voltage signal was directly applied to **coils** in **RMM**.

This means that the voltages were in phase during nominal load conditions and that there are distinct cancellations of the peak of the current in the solution shown in section C.

This problem was solved by connecting an isolated neutral with the impedance  $R_N = 1000 \Omega$  to the circuit. The circuit layout is shown in Figure 13.  $R_N = 10 \text{ k}\Omega$  can also be used as depicted, but this will cause a more stiff system.  $R_N = 1000 \Omega$  is used for all the co-simulations, and it is seen that from co-simulation results not included in this thesis, that  $I_0 < 1 \cdot 10^{-6} \text{ A}$ , assumed negligible. However it is clearly depicted in, e.g., Figure 31a that  $i_0$  is negligible.

In Figure 13 it is depicted that the voltage sources are **DC-sources**. The setting for the **DC-source** in Comsol is shown in Figure 14. The voltage in the coils is constant between each co-simulation communication time  $\Delta t_i$ . It is assumed that the constant voltage value is sufficiently accurate (although constant) between each  $\Delta t_i = 1.0 \cdot 10^{-4} \text{ s}$ . This time constant was determined after trial and error.

Further, it should be noted that it is connected to an Ohmic resistance on each side of the **RMM Coils**. It is needed to have a small resistance in series with the **RMM: Coils** to avoid convergence errors [55]. It should be added end winding inductances in the **EC**. This was initially done but later removed to eliminate a potential anti-convergence cause from the co-simulation. An earlier circuit is depicted in Figure 15. It was suspected that the leakage inductance could cause a

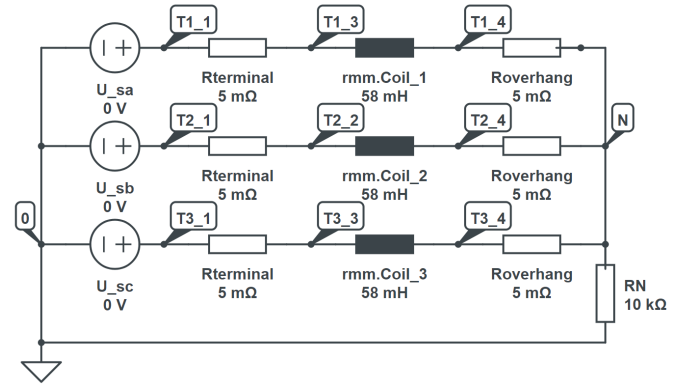


Fig. 13: The external circuit in Comsol with initial voltage values. The coil resistance of the effective machine length is  $R_s = rmm.RCoil_1 = 1.9 \Omega$ , and the synchronous reactance obtained from the field solution is  $X_s = 58 \text{ mH}$  from Table IV. The parameter values are of minor importance. This circuit is drawn with the circuit tool Circuitlab [54].

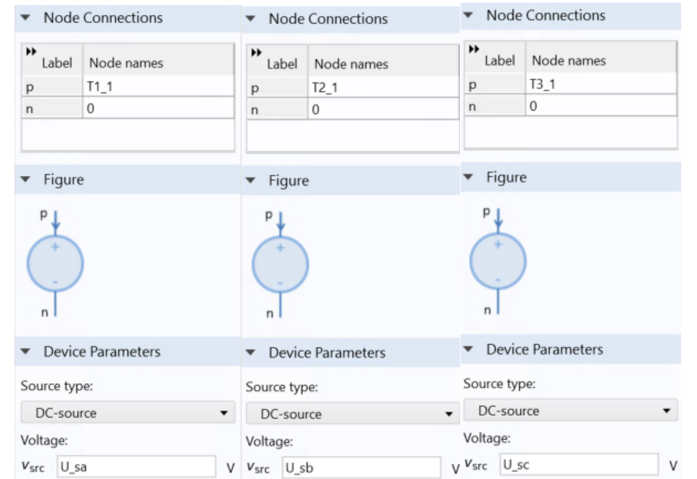


Fig. 14: DC-sources in Comsol Desktop. The *input parameter*  $U_{sa}$  is changing its value for each time step according to the value from Simulink. The corresponding method is valid for the two other phases.

simulation divergence. The issue was addressed when the co-simulation stopped on error time  $t_\epsilon = 0.0023 \text{ s}$  with an errors message in the .fmu that the co-simulation had stopped because a singularity was reached. The suspicion was that the end winding inductance could cause an additional stiffness to the system [43]. This exact problem at  $t_\epsilon$  persisted for approximately a month. It was concluded that the leakage inductance stiffness contribution was not the cause of the problem, but a hanging node caused the error in the circuit that Comsol was unable to detect. The error in the modeling has probably been made because the circuit was changed several times. The description of this error for the circuit in Figure 15 is:

- 1) The rmm.coil\_2 was by mistake connected to T2\_2 and T2\_4.
- 2) The coil in T2\_2 to T2\_3 must have been a hanging

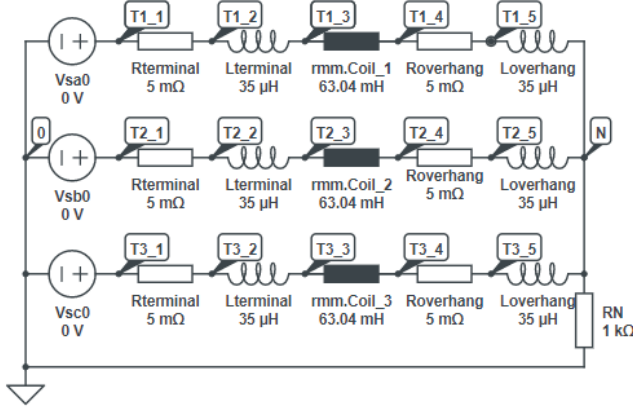


Fig. 15: A circuit used earlier in the modelling phase. These parameters are not used for co-simulations.

node that Comsol was not able to detect. T2\_3 was not connected to any node/external component.

This issue could potentially have been detected earlier if Comsol had a circuit layout interface as other FEM software have. These results persisted for several weeks, at the same time instant in the co-simulation. Several things were tried: Refinement of the mesh, improving the solver in Comsol. This was a very time-consuming task, and it was nothing apparent that told that this was the mistake; The Comsol model is a relatively large model with many definitions. The error could be due to the mesh, solvers in Comsol, solver in Simulink, an error with the .fmu-block, or the coil definitions.

### G. Parameters for the Regulators

The parameters that are obtained from the field solution are given in Table IV. It is seen that the inductance is reduced with a higher current loading, especially in the d-axis flux linkage vector from the PMs that is present at all times. The presence of the PMs is easily recognized at, e.g., a current load of  $I_s \cdot 0.05$  where the flux linkages  $\Psi_q \ll \Psi_d$ .

In a late stage of the project period it was concluded that the current loading for determining  $L_d$  should approximately rated MTPA condition for the d-axis  $L_d(i_d = -0.4, i_q = 0.0)$  pu and for the q-axis  $L_q(i_d = 0.0, i_q = +0.9)$  pu given in the second last row in Table IV. How this issue was reached will be described section VIII, and the difference will be seen from the results in section VII. All the results had to be computed a second time, denoted co-simulation 2 (CS2) and described with parameters  $L_{d2} = 30.8030$  mH and  $L_{q2} = 53.6110$  mH. The old results denoted co-simulation 1 (CS1) was calculated with parameters  $L_{d1} = 23.4048$  mH and  $L_{q1} = 53.0932$  mH.

## VI. METHOD - CO-SIMULATION SET UP

### A. Co-Simulation Set Up in COMSOL

Further details about the general setup of the co-simulation model is given in [56], [53], [57], [58]. The specific co-simulation for this model is defined with the following **input**

TABLE IV: After running several parameter determination tests with different load in the d- and q-axis with Figure 13.

d-axis test			q-axis test		
$I_q = 0$	$\Psi_d$ [Wb]	$L_d$ [mH]	$I_d = 0$	$\Psi_q$ [Wb]	$L_q$ [mH]
$I_d = 5\%I_s$	0.9729	27.9687	$I_q = 5\%I_s$	0.0197	56.4257
$I_d = 7\%I_s$	0.9767	27.8663	$I_q = 7\%I_s$	0.0275	56.4286
$I_d = 10\%I_s$	0.9824	27.6962	$I_q = 10\%I_s$	0.0393	56.4200
$I_d = 50\%I_s$	1.0526	25.6681	$I_q = 50\%I_s$	0.1934	55.4791
$I_{d1} = 100\%I_s$	1.1263	<b>23.4048</b>	$I_{q1} = 100\%I_s$	0.3702	<b>53.0932</b>
$I_d = 150\%I_s$	1.1863	21.3404	$I_q = 150\%I_s$	0.5271	50.4001
$I_{d2} = -40\%I_s$	0.87830	30.8030	$I_{q2} = 90\%I_s$	0.3364	53.6110

Inputs		
Parameter na1	Initial value	Unit
U_sa (Usa)	0[V]	V
U_sb (Usb)	0[V]	V
U_sc (Usc)	0[V]	V
w_r (wr [ra	0[rad/s]	rad/s

(a) The three-phase input voltages are taken from the pre-defined parameter list.

Block Parameters		
Parameter na1	Initial value	Unit

Outputs		
Expression	Unit	Name
I_sa		I_sa [A]
I_sb		I_sb [A]
I_sc		I_sc [A]
T_e		T_e [Nm]
Psi_sa		Psi_sa [Wb]
Psi_sb		Psi_sb [Wb]
Psi_sc		Psi_sc [Wb]

(b) Output to Simulink.

Co-simulation	
	I_sa (I_sa)
	I_sb (I_sb)
	I_sc (I_sc)
	Torque (T_e)
	Psi_sa (Psi_sa)
	Psi_sb (Psi_sb)
	Psi_sc (Psi_sc)

(c) Defined probes.

Fig. 16: LiveLink setup up in COMSOL.

**parameters** shown in Figure 16a. The input parameters are placed in each coil for the corresponding phase shown in Figure 14.

The **output variables** in this thesis is shown in Figure 16b. The output variables are defined as measurement probes shown in Figure 16c. The currents are the measured currents in the coils **RMM: Coil** and not in the **EC** to ensure the correct current direction. The axial torque is calculated with Arkkio's method. The flux linkages are used for measurements only and do not affect the feedback to the control system. The flux linkages should be removed since they are not used for any results. The flux linkage results were obtained by using Comsol Desktop. It is only possible to import one study for LiveLink to Simulink [57], [53]. The exported study is depicted in Figure 17. **Study 2: Time-dependent study** is used in the LiveLink. The initial values are solved with the study **Study 1: Stationary Solution** in a separate study [56], [57], [53]. The initial values in study 2 are then selected from Study 1. Each time something was changed in the Comsol model, new initial values with **Study 1** were re-computed. It is selected to store the solution at the end of the communication step

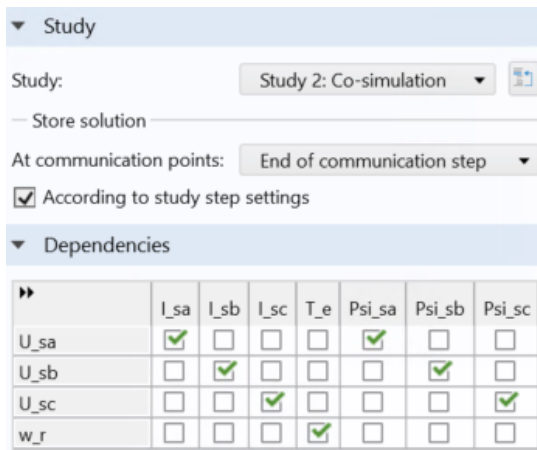


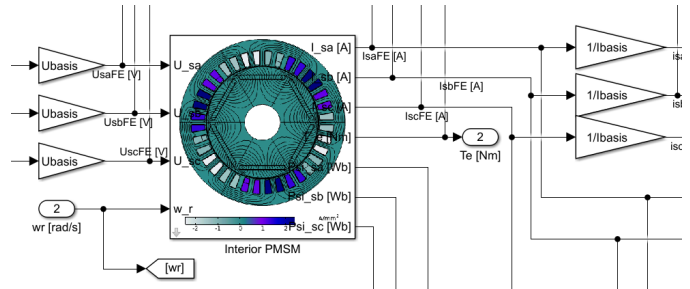
Fig. 17: Study selection and dependencies. **Study 2: Time dependent study.**

to reduce the amount of data stored after each co-simulation. **According to study step** settings are checked. The time step in Comsol  $dt$  is set equal to the communication step  $\Delta t_i = dt$  in the co-simulation block in Simulink. It is also specified by Comsol [57],[53] that any dependencies between the input parameters and the output variables have to be specified if necessary shown in Figure 17. The diagonal dependency list are checked for all simulations. The co-simulation should, in principle, be ready to be performed from the Comsol side. It is ensured that the **RMM** file and the **FMU** file have the same name, e.g. *impsm\_v15.mph* and *impsm\_v15.fmu*, respectively. It is recommended that the two files are stored in the same directory folder, although not necessary [56], [57],[53]. The .fmu directory path was copied from the Comsol message log and pasted to the co-simulation block in Simulink.

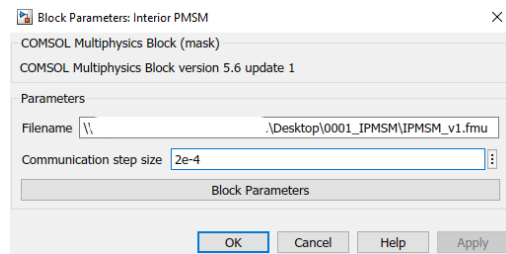
*B. Co-Simulation Settings in Simulink*

To start the co-simulation, double click on the LiveLink for Simulink symbol on the computer Windows Desktop. The user is asked to write a user name and define a password the first time in the black LiveLink window. It is an idea to write something in that window called *COMSOL Multiphysics with Simulink* for the LiveLink to initiate. If it is not typed in the window, the LiveLink sometimes hangs there without opening Matlab. After that, the LiveLink for Simulink is started. The co-simulation .slx-file has to be opened with the Matlab opened when clicking on the LiveLink with Simulink icon. It is not possible to perform a co-simulation by double-clicking on the .slx file directly from the file in the folder. With the LiveLink Matlab version running, click open and browse through the user’s documents and open the relevant .slx file. It should be mentioned that it is possible to run the Matlab-commands clear all; close all; clc; without the co-simulation window shutting down, even though the text in the command window at LiveLink Matlab startup gets deleted. That is the case in this work since the controller parameters are loaded from a .m file to Simulink. The Matlab script in also needs to run with the LiveLink Matlab.

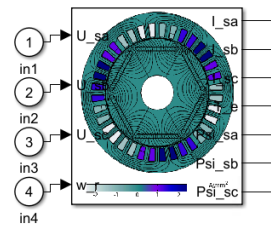
After Matlab/Simulink is opened with LiveLink for Simulink, it is possible to browse the Library Browser in Simulink and select the co-simulation block for Comsol. The block version used in this project is named **COMSOL 5.6: COMSOL Co-simulation**. This block only appears if LiveLink is activated. It is not possible to find the co-simulation block in the Simulink Library Browser when opening the regular Matlab/Simulink. The resulting co-simulation block in this project is shown in Figure 18a. Here it is shown the input parameters into Comsol from Simulink and the output variables from Comsol into Simulink outlined in section V. To use the previously exported .fmu file, the user



(a) Co-simulation FMU block for the IPMSM used in this project.



(b) The whole directory of the **FMU**-file have to be written. The communication step used for all the co-simulations is  $\Delta t_i = dt = 1 \cdot 10^{-4}$  s.



(c) Block below the co-simulation mask.

Fig. 18: LiveLink settings in Simulink.

has to enter its directory obtained from Comsol Desktop or found in the directory folder. The communication step also needs to be defined equal to the time-dependent step in Comsol  $\Delta t_i = dt = 1 \cdot 10^{-4}$  s in this thesis. This is shown in Figure 18b. If the export is done correctly, the previously defined input parameters and output variables must be connected with Simulink lines. If the export is unsuccessful, the user will get an error message when clicking "OK" in Figure 18b.

The layout below the co-simulation mask is shown in Figure 18c. If the user double click the icon below the mask,

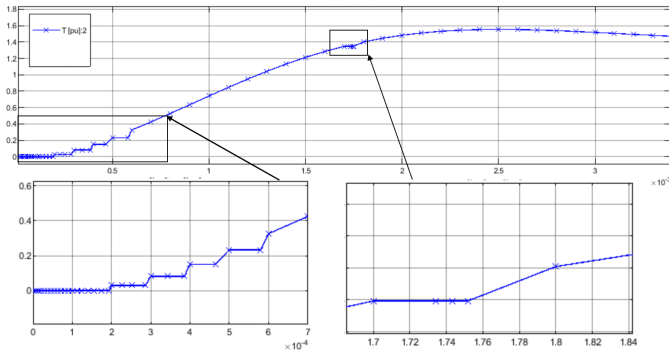


Fig. 19: Constant communication steps, with the internal Simulink solver *ode23tb*.

it is possible to get more information about the .fmu-setup, like version number, some code lines, and more.

When all the steps in section V and section VI were done, the FEA motor and controllers were ready for co-simulation.

### C. Time Stepping

Figure 19 shows that even though it is a strict data exchange between Comsol and Simulink in the time intervals  $\Delta t_i$ , the internal solvers in Simulink are using variable time steps at some points. The variable steps are shown at the start of the simulation and the other time in the co-simulation. This is indicated within the black boxes in Figure 19. This is because the solver settings *ode23tb* with minimum relative error  $1 \cdot 10^{-6}$  is used. The variable step solver in Simulink can be a reason for convergence error and poor utilization of the CPU.

### D. Notes on Post-Processing

This section mentions practical considerations that can potentially save time for the user. The user has to stop the Simulation in Simulink with the **stop** button in Simulink. Avoid pressing **cancel** in the co-simulation LiveLink window. Pressing cancel will shut down the co-simulation ineffectively. After the simulation has stopped, it is possible to run the command »mphlaunch in the Matlab command window to open the Comsol Desktop and view the results from the last simulation. The co-simulation should stop completely before running the »mphlaunch command. If not, it will be stored two or sometimes even more Comsol models on the server. The user is then requested to specify to run either mphlaunch('SimModel1') or mphlaunch('SimModel2'). Both are the same models locked on the server to each other. The user usually wants to make changes to the model after using »mphlaunch. After any applied changes, the user has to compute new initial values, export the new .fmu file and save the .mph-file. After that, the user may want to run a new simulation without closing and restarting LiveLink. The problem is that when multiple simulation models are stored on the server, the user is not able to save the changes in the model after co-simulation. In this case, new initial values were changing the phase sequence or the initial rotor position.

When it is not possible to save the new initial values, changes are not applied to the model. The consequence of

this is that the user has to close the .mph model, close the LiveLink for Simulink connection, open the regular Comsol Desktop, apply the changes in the regular Comsol Desktop, export the .fmu-file, save the .mph-file, ensure that the regular Comsol desktop file is closed, open the LiveLink for Simulink connection, open the .slx-model, and then perform the desired co-simulation with the new initial conditions. This sequence of steps can take up to several minutes.

Another solution is to close LiveLink, reopen Livelink, run the co-simulation for 1-2 time steps to "make the LiveLink connection", stop the simulation, write the »mphlaunch command apply the desired changes, save, close, and run a co-simulation.

This sequence made searching for failures and improving the model, take a very long time. This is on top of the relatively long simulation intervals required to get usable results for further evaluating the troubleshooting process.

## VII. RESULTS

### A. Introduction

In this section the results from the co-simulation FEM model with the LPM model in a separate simulation is presented. Details about the simulation models are depicted in the model used in Figure 55 and below the grey FEA IPMSM mask in Figure 56. This section is mainly focusing on the simulation results with parameter  $L_{d2}$ , called co-simulation 2 (CS2). The results from the first co-simulation with parameter  $L_{d1}$  is called co-simulation 1 (CS1). CS1 is mentioned less than CS2, although also included in this section. The results from CS1 are included in the appendix and will be a part of the discussion chapter in section VIII. Appendix: The results from CS2 is given in Figure 26a-Figure 36d. The results for CS1 are given in Figure 37a-Figure 47d.

In the first part of this section it is performed a stability and frequency response analysis to validate the controller tuning.

### B. Control, Stability and Frequency Response

The controller parameters that is used in this thesis is shown in Table V. The parameter  $L_d$  was too low during these calculations. However, a new frequency analysis with the correct parameter  $L_{d2} = 30.803$  mH have no effect on the frequency response and the Bode diagram. It is the old  $L_{d1} = 23.4048$  mH that is used in Figure 20a and Figure 20b. This is feasible since the  $dq$  transfer functions are only dependent on the converter and filtering parameters due to parameter cancellation of the reactants shown in the OL transfer-function  $h_{oid}$  in Equation 51 and gain parameter  $K_{pd}$  in Equation 49. This can also be verified with the script in section D by changing values.

The parameters in Table V are however changed indicated with subscript <sub>2</sub> and indicated with <sub>1</sub> for the old parameters. The basis values are also included in Table V. Some of the values have been listed in other places in this thesis but are included here for convenience. The switching frequency  $f_{sw}$  has been used from the start of the thesis and for all the results. It is assumed that [1/s] and [rad/s] are the same unit in the Bode diagrams.

TABLE V: Parameters of the current loop and the speed loop system with the LPM transfer functions. When it is denoted e.g.  $d1$  in the description this is the parameter from the case with  $L_{d1}$ . For the Bode diagrams, it is assumed that 1/s is equal to rad/s.

Description	Parameter	Value	Unit
<b>Basis values</b>			
Voltage	$U_{s,basis}$	230	V
Current	$I_{s,basis}$	4.93	A
Flux linkage	$\Psi_{s,basis}$	1.0354	Wb
Power	$S_n$	3400	VA
Torque	$T_{basis}$	32.484	Nm
Impedance	$Z_{s,basis}$	46.6531	$\Omega$
Nominal frequency	$f_n$	50.0	Hz
Nominal speed	$\Omega_n$	104.7	rad/s
Load constant	$k_L$	0.0028	
<b>Linearized converter</b>			
Switching frequency	$f_{sw}$	1000	Hz
Switching period	$T_{sw}$	1.000	ms
Converter delay	$T_{delay}$	0.333	ms
Current filter delay	$T_{fd} = T_{fq}$	0.200	ms
<b>Current controllers (modulus optimum)</b>			
PM flux linkage	$\psi_m$	0.9302	pu
Reactance ( $d2$ )	$x_{d2}$	0.2072	pu
Reactance ( $d1$ )	$x_{d1}$	0.1576	pu
Reactance ( $q2$ )	$x_{q2}$	0.3610	pu
Reactance ( $q1$ )	$x_{q1}$	0.3575	pu
Stator resistance	$r_s$	0.0408	pu
Gain ( $d2$ )	$K_{pd2}$	0.6190	pu
Gain ( $d1$ )	$K_{pd1}$	0.4703	pu
Electric time ( $d2$ )	$T_{d2} = T_{i,d2}$	0.0162	s
Electric time ( $d1$ )	$T_{d1} = T_{i,d1}$	0.0123	s
Zero CC ( $d2$ )	$1/T_{d2}$	61.728	rad/s
Zero CC ( $d1$ )	$1/T_{d1}$	81.301	rad/s
Gain ( $q2$ )	$K_{pq2}$	1.0773	pu
Gain ( $q1$ )	$K_{pq1}$	1.0668	pu
Electric time ( $q2$ )	$T_{q2} = T_{i,q2}$	0.0282	s
Electric time ( $q1$ )	$T_{q1} = T_{i,q1}$	0.0279	s
Zero CC ( $q2$ )	$1/T_{q2}$	35.46	1/s
Zero CC ( $q1$ )	$1/T_{q1}$	35.85	1/s
Small time	$T_{sum}$	0.533	ms
Pole of $T_{sum}$	$1/T_{sum}$	1876	1/s
Rise time	$4.7 \cdot T_{sum}$	2.500	ms
Settling time	$8.4 \cdot T_{sum}$	4.500	ms
Equivalent time	$T_{eq,i}$	1.066	ms
Crossover	$\omega_{c,id} \approx \omega_{c,iq}$	853	rad/s
Gain margin	$ h_{oid}(j\omega_{180^\circ}) _{dB}$	$\infty$	dB
Phase margin	$\angle h_{oid}(j\omega_{0dB})$	65.5	$^\circ$
Resonance CL $\omega_0$	$1/(\sqrt{2}T_{sum})$	1325.8	rad/s
<b>Speed controller (symmetrical optimum)</b>			
Gain	$K_{pn}$	14.192	pu
Mechanical time	$T_m$	87	ms
Tacho filter time	$T_{f,n}$	2	ms
Small time	$T_{sum,n}$	3.1	ms
Pole of $T_{sum,n}$	$1/T_{sum,n}$	323	1/s
Parameter	$\beta$	4	pu
Regulator time	$T_{i,n} = \beta T_{sum,n}$	12.3	ms
Zero of $T_{i,n}$	$1/T_{i,n}$	81	1/s
Torque limit	$\tau_{e,max}$	1.6	pu
Crossover	$\omega_{c,n}$	163	rad/s
Gain margin	$ h_{0,n}(j\omega_{180^\circ}) _{dB}$	$-\infty$	dB
Phase margin	$\angle h_{0,n}(j\omega_{0dB})$	36.9	$^\circ$

It is performed a frequency-response analysis of the d-axis only with Equation 51 since the Bode-diagram the OL  $h_{oid}(s) = h_{oiq}(s)$ . The q-axis system have the same crossover frequency  $\omega_{c,iq} = \omega_{c,id} = 853$  rad/s, phase margin  $\angle h_{oiq}(j\omega_{0dB}) = 65.5^\circ$  and is identical from the bode plots. The OL speed system  $h_{0,n}(s)$  from Equation 53 is also analysed. The results from the frequency analysis are depicted in Figure 20a.

First let us start with  $h_{oid}(s)$ . It is one pure integrator in the denominator (Norwegian: "nevner")  $n_0$  of the inner current loop. That implies that the system is having a phase of  $\angle h_{oid}(1.00) = -90^\circ$  at low frequencies for instance  $j\omega = 1.00$ . The phase is  $-90^\circ$  at even lower frequencies e.g.  $j\omega = 0.01$ , but the amplitude  $|h_{oid}(0.01)|$  will approximately be 40 dB higher since  $j\omega = 1/100 = 0.01$  1/s is reduced by 2 decades. The amplitude is decreasing by  $|h_{oid}(1.00)|_{dB} = 20$  dB/decade until the pole of the small time constant  $1/T_{sum}$  is reached. At this frequency the phase is shifted to  $\angle h_{oid}(1/T_{sum}) = -180^\circ$  asymptotically. That is a  $-90^\circ$  reduction of the phase. The amplitude is decreasing approximately  $|h_{oid}(1/T_{sum})|_{dB} = 40$  dB/decade. The phase lift of the PI-controller with  $T_{i,d}$  or decrease in phase from the electrical time constant  $T_d$  is not shown in the Bode-diagram, because of pole/zero cancellation.

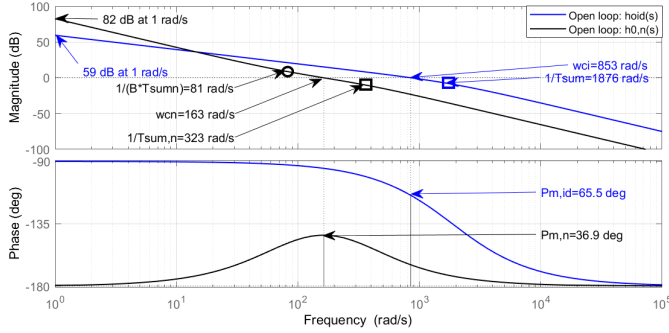
For the speed loop it is two pure integrators in the denominator (Norwegian: "nevner")  $n_0$ . The phase at low frequencies are  $\angle h_{0,n}(0.01) = -180^\circ$ . The amplitude is decreasing with  $|h_{oid}(1.0)|_{dB} = 40$  dB/decade. Then it is a phase lift first at the zero  $1/T_{i,n}$  from the PI speed controller. The phase is lifted from  $180^\circ$  to  $\angle h_{0,n}(1/T_{i,n}) = -90^\circ$ . From here the amplitude is decreasing with  $|h_{oid}(1/T_{i,n})|_{dB} = 20$  dB/decade. The parameter  $\beta = 4$  determines when this phase lift is happening. If the parameter  $\beta$  is higher the phase lift from the PI-controller will happen at lower frequencies. This will also give a higher phase margin, but the cost is a lower bandwidth, since the cutoff-frequency will be shifted to lower frequencies. The frequency for the process  $1/T_{sum,n}$  is a pole and the phase is asymptotically reduced to  $\angle h_{0,n}(1/T_{eq,n}) = -180^\circ$  and the amplitude is falling with  $|h_{oid}(1/T_{eq,n})|_{dB} = 40$  dB/decade.

It is investigated if the systems are stable with a Nyquist diagram. It is zero poles  $N_p = 0$  in the right half plane for the open loop systems of  $h_{oid}$  Equation 51,  $h_{oiq}$  Equation 52 and  $h_{0,n}$  Equation 53. This is apparent from Rouths stability criterion. The coefficients of the 2<sup>nd</sup> order characteristic polynomials in the denominators  $n_0$  of the open loop transfer functions  $h_0 = t_0/n_0$  are greater than 0 (equal sign on the coefficients). The three systems  $h_{oid}$ ,  $h_{oiq}$  and  $h_{0,n}$  is therefore *open stable*. From Figure 20b we are counting that the number of rotations of the vector around  $-1$  on the real axis is  $\Delta \angle(1 + h_{oid}) = \Delta \angle(1 + h_{oiq}) = \Delta \angle(1 + h_{0,n}) = 2 \cdot \pi \cdot (N_p - N_n) = 0$ . Only Equation 52 and Equation 53 are included in Figure 20b. The number of poles in the closed loop system is  $N_n = 0$ . The systems is by this analysis confirmed to be stable.

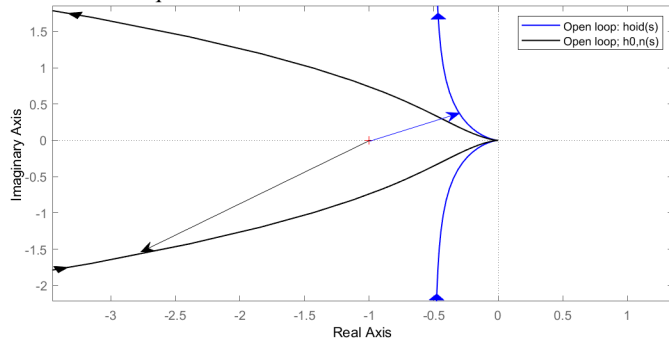
The frequency response in Figure 20a and stability analysis in Figure 20b is performed with the LPM representation of the motor and regulators with usual transfer functions in Matlab. Hence, linearized parameters around a working point. The



inner loops are the first tuned controllers, and the second stage is the cascade-connected outer loop speed controller. The disturbance is decoupled for stability analysis by the principle of superposition, and the transfer functions are at zero-speed  $n = 0.0$  pu. Hence, no cross-coupling disturbance in the d-axis and q-axis inner loop control and no torque load  $\tau_L = 0$  pu disturbance.



(a) Frequency response of the inner loop (torque control) and outer loop (speed control). Zeros are denoted with circles, and poles are denoted with square brackets.



(b) Nyquist stability diagram with  $\Delta\angle(1 + h_0(s)) = 0$ .

Fig. 20: Bode-diagram and Nyquist stability diagram.

### C. MTPA Rated Torque reference

This co-simulation is comparing the step response between the FEM motor and the regular LPM motor in a separate simulation with equal parameters for the control system with the concept shown in Figure 54. The applied signal is at start with the rated torque reference of the machine  $\tau_{e,n} = T_n/T_{basis} = 0.8835$  pu with the parameters from the new co-simulation CS2 in Table V.

Figure 21a/Figure 26a compares the electromagnetic torque between the FEM motor and the LPM motor. The time for each peak is indicated with black markers, and the crossing time  $\tau_e = \tau_{eref}$  is indicated with blue markers. The calculated rise time for current controllers is  $T_{rise} = 2.5$  ms in Table V. The settling time for the FEM motor is estimated to be approximately  $T_{settlingFEM2} = 8.75$  is 4.25 ms longer than the calculated value  $T_{settling} = 4.5$  ms in Table V. The peak values of the currents  $i_{dq}$  is shown in Figure 37b. The peak values in this section are retrieved from the Simulink peak measurement tool. Other values are also written in Figure 21a.

### D. MTPA Rated and Negative Value

This co-simulation is comparing the step response between the FEM motor and the regular LPM motor in a separate simulation with an equal control system in Figure 54. This is the whole co-simulation from the previous subsection. It is applied four different reference steps  $\tau_{eref}$  in this simulation shown in Figure 21b/Figure 27a. The rated torque reference  $\tau_{e,n} = T_n/T_{basis} = 0.8835$  pu is applied from start  $t = 0.0$  s to  $t = 0.070$  s. Then a torque reference of  $\tau_{eref} = 0.0$  pu is applied to  $t = 80.0$  ms. After that it is applied a torque reference  $\tau_{eref} = -0.5 \cdot T_n/T_{basis} = -0.4418$  pu to  $t = 120.0$  ms. It is applied a torque reference  $\tau_{eref} = 0.00$  pu for the rest of the simulation up to  $t_{CS2} = 200.0$  ms.

The torque from the FEM motor have a low amount of cogging torque and torque ripples up to about  $t = 0.025$  s in the speed range below  $n \approx 0.3$  pu.

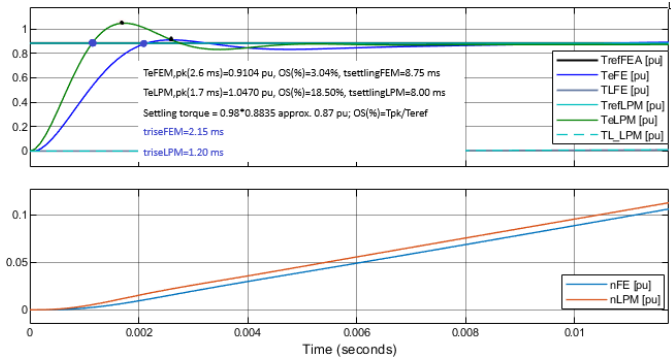
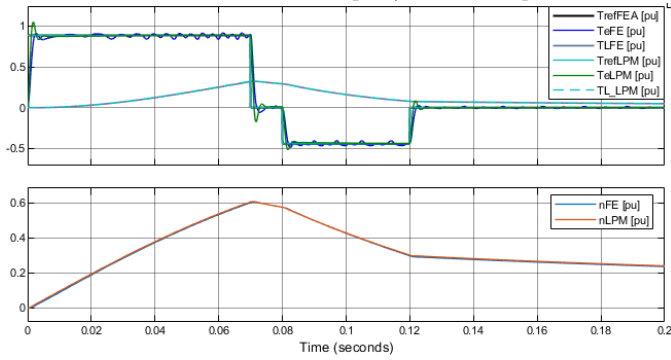
The corresponding period for the  $i_{dq}$  currents are shown in Figure 21c/Figure 27b. The LPM model is approaching  $i_d = 0$  pu and  $i_q = 0$  pu in a short amount of time when  $\tau_{eref} = 0.00$  pu from  $t = 0.12$  s. For the FEM model  $i_q$  is reaching 0.0 pu at approximately the same time as the LPM model. The current  $i_d$  for the FEM motor is evidently oscillating around the current reference in the period from  $t = 0.12$  s to the end  $t_{CS2} = 200.0$  ms. The  $i_d$ -current have ripples below  $n = 0.3$  pu, while the q-axis current generates few ripples in the whole  $t_{CS2} = 200.0$  ms simulation. The three-phase currents of the FEM motor is shown in Figure 27c. In Figure 27c  $i_{sFEM}$  is decaying from  $t = 0.120$  s to the end of CS2, but not reaching zero. The three-phase voltage is shown in Figure 27d. In Figure 27d  $|u_{sLPM}|$  higher overshoots while  $|u_{sFE}|$  have higher undershoot values in the transitional phase  $t = 0.07$  s and  $t = 0.08$  s. It is also shown that the  $u_{saFE}$  is lagging  $u_{saLP}$  from  $t = 120.0$  ms to  $t_{CS2} = 0.2$  s.

### E. MTPA 1.6 pu and 1.0 pu Torque Reference

This co-simulation is comparing the step response between the FEM motor and the regular LPM motor in a separate simulation with an equal control system shown in Figure 54. It is applied a torque reference limit  $\tau_{emax} = 1.6$  pu from start to  $t = 0.080$  s. This is to reduce the acceleration time up to steady-state speed. The time  $t = 0.08$  s was estimated from a regular LPM simulation for  $\tau_L$  to reach  $\tau_e = 1.0$ . For the rest of the simulation, the torque reference is  $\tau_{eref} = 1.0$  pu. The estimated time shift for the torque reference shift was estimated the time for this shift with a regular Simulink simulation.

Table VI shows values from the figures that are listed in the subtitles of the table. All values are measured with Simulink measurement tools. In appendix, Table IX is a similar table for the case CS1.

Starting with the analysis of the mechanical output. The complete mechanical period is shown in Figure 22a/Figure 28a. Figure 28b shows the transitional phase from  $\tau_{emax} = 1.6$  pu to  $\tau_{eref} = 1.0$  pu in torque reference. The FEM motor is having a similar sub-transient response. In Figure 28c steady state, the electromagnetic torque of the LPM model is approximately equal to the reference torque.


 (a) Mechanical rise step  $\tau_{e,n} = 0.8835$  pu.


(b) Rated and negative step

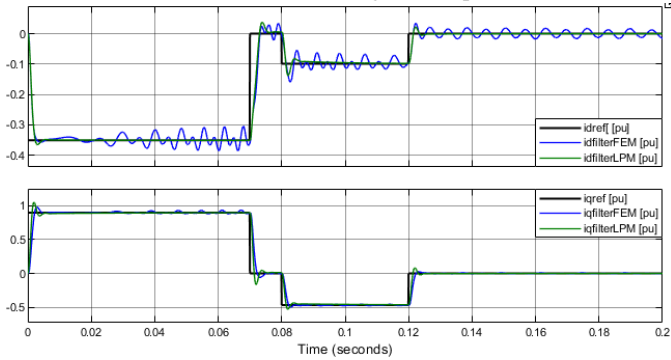

 (c) Current waves with 3<sup>rd</sup> quadrant operation.

Fig. 21: Rated step and negative step torque.

Based on this it is assumed that the mean torque of the Comsol model and the load torque is equal in equilibrium  $\tau_{eFEM} = \tau_{L,FEM}$ . This implies that the torque difference between the electromagnetic torque and the FEM motor  $\Delta\tau = (\tau_{eFEM} - \tau_{eref}) / \tau_{eref} \cdot 100 = (0.987 - 1.000) / 1.000 \cdot 100\% = -1.60\%$  under estimation of the torque. The speed  $n_{FE}$  is  $\Delta n_{F-S} / n_F (\%) = (1.056 - 1.066) / 1.066 \cdot 100\% = -0.94\%$ .

Next is the analysis of the electrical transients. Figure 29a shows that the FEM model phase current is lagging the LPM phase current. This difference is amplified with time. The phase shift time of the positive peak of the FEM and LPM is listed with values in Table VI. From Figure 29a the current magnitude  $|i_{sFEM}|$  is slightly higher than  $|i_{sLPM}|$ . Only Phase B is included for clarity. Figure 29b shows the  $i_{dq}$  transitional phase from  $\tau_{eref} = 1.6$  pu to  $\tau_{eref} = 1.0$  pu step. Here  $i_q$  in the FEM machine is slower with a lower overshoot than the LPM model. Figure 29b shows that the overshoot for

TABLE VI: MTPA control  $\tau_{eref} = 1.6 \rightarrow 1.0$ . Data points are retrieved from the measurement function in Simulink Scope. F = FEM and S = LPM. F-S = difference between LPM and FEM results. OS = overshoot value obtained from Simulink scope.

Description	Symbol	Value	Unit	Time
<b>From the beginning in Figure 28a</b>				
Reference	$T_{ref}$	1.600	pu	0.000 s
Peak start	$T_{eF}$	1.640	pu	0.0024 s
OS start	$T_{eF}$	1.025	%	0.0024 s
Peak start	$T_{eS}$	1.887	pu	0.0018 s
OS start	$T_{eS}$	1.1794	%	0.0018 s
<b>Torque steady state in Figure 28c</b>				
Load torque	$T_{L,F}$	0.987	pu	0.1766 s
Load torque	$T_{L,S}$	1.003	pu	0.1766 s
Load diff.	$\Delta T_{L,F-S}$	-0.0382	pu	0.1766 s
Speed	$n_F$	1.057	pu	0.1766 s
Speed	$n_S$	1.065	pu	0.1766 s
Speed diff.	$\Delta n_{F-S}$	-0.0200	pu	0.1766 s
<b>Peak phase current in the last el. period of Figure 29a</b>				
Peak	$ \hat{i}_{sbF} $	1.130	pu	0.1490 s
Peak	$ \hat{i}_{sbS} $	1.094	pu	0.1470 s
Difference	$\Delta \hat{i}_{sb,F-S}$	+0.036	pu	
Phase lag	$\Delta t_{F-S}$	-2.102	ms	
<b>Current dq in Figure 29b</b>				
Peak	$ i_{dfF} $	-0.3480	pu	0.0830 s
Peak	$ i_{dfS} $	-0.3913	pu	0.0840 s
Peak	$ i_{qfF} $	0.9500	pu	0.0822 s
Peak	$ i_{qfS} $	0.8940	pu	0.0819 s
<b>Voltage dq in Figure 29c</b>				
Average	$u_{qF}$	0.9134	pu	0.1766 s
Average	$u_{qS}$	0.9381	pu	0.1766 s
Difference	$\Delta u_{q,F-S}$	-0.0247	pu	0.1766 s
Underest.	$\Delta u_{q}/u_{qS}$	-2.6300	%	0.1766 s
<b>Error in Figure 29d</b>				
Difference	$\Delta e_d$	0.1068	pu	0.1766 s
Difference	$\Delta e_q$	0.0640	pu	0.1766 s

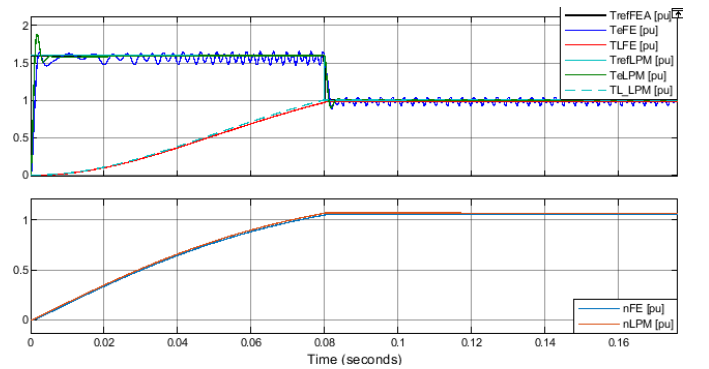
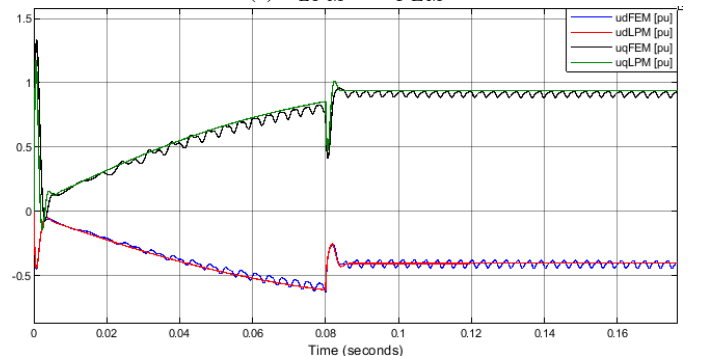

 (a)  $n_{LPM} > n_{FEM}$ 

 (b) Offset voltage  $\Delta u_{q,FEM-LPM} / u_{qLPM} = -2.63\%$  pu.

 Fig. 22:  $\tau_{emax} = 1.6$  pu and  $\tau_{eref} = 1.0$  pu.

$i_d$  in the FEM motor is larger compared to the LPM motor.

Now results between the cases *CS1* and *CS2* will be compared. In the second case, *CS2*, shown in Figure 22b/Figure 29c, the d-axis voltage  $u_{dCS2}$  is approximately equal for the LPM model and the FEM model, in both magnitude and dynamic response. This is also the case for the first case *CS1* with  $u_{dCS1}$  in Figure 40c. However, the voltage  $u_{qCS1}$  have an offset between the FEM model and the LPM model with  $\Delta u_{q1,F-S}/u_{q1,S} = (0.8800 - 0.9381)/0.9381 \cdot 100\% = -6.19\%$  listed in Table IX. For  $u_{qCS2}$ , with the new parameter  $L_{d2}$ , the offset between LPM and FEA is smaller with the value  $\Delta u_{q2,F-S}/u_{q2,S} = -0.0247/0.9381 \cdot 100\% = -2.63\%$ . That is an improvement in coltage accuracy of  $6.19\% - 2.63\% = 3.56\%$ . It is an error in the measurements from *CS1*. The voltage  $u_{q1}$  was only read in a zoomed scope, while  $u_{q2}$  was measured with an average operator. It makes sense to use the "voltage requirement" reference to be  $u_{qLPM}$ , since this is the voltage that meet the voltage requirements.

Figure 29d shows the steady state error  $e_{dq} = i_{dq,ref} - i_{dq,filter}$  into the d-axis and q-axis controllers from the FEM machine with peak-to-peak values listed in Table VI.

#### F. MTPA Stair reference

This co-simulation is comparing the step response between the FEM motor and the regular LPM motor in a separate simulation with an equal control system. Explaining case *CS1*: The original time limit of the co-simulation was 250.0 ms for the *CS* with  $L_{d1}$ . However, it was assumed  $t_{CS1} = 210.0$  ms was sufficient. *CS1* had to be interrupted due to server overload on NTNU, and the simulation time was more than 24 hours in this case. For *CS2*, the simulation time was  $t_{CS2} = 0.250$  s because this simulation was performed on a Windows 10 computer without other users, leading to a decreased computational time.

A trade-off between simulation time and steady-state values were evaluated. The motor is not reaching steady-state between each new step reference with the load disturbance  $T_L = k_L \cdot \omega_r^2$ , seen by  $\tau_e \neq \tau_L$ . The electromagnetic torque is assumed to reach an approximate steady-state value. However, the electromagnetic torque value from Comsol will evidently from several previous simulations decrease by an amount as the speed increases depicted in i.e. Figure 23a.

For this case it is applied a new reference torque every  $\Delta t = 50$  ms, with magnitudes from  $\tau_{eref} = \{0.25, 0.75, 1.25, 1.75, 2.00\}$  pu shown in Figure 23a/Figure 30a. Figure 30b is taking a closer look when  $\tau_{eref} = 2.0$  pu. Figure 30c shows a zoomed figure when the machine is unsaturated. The saturation level is low at the steps  $\tau_e = \{0.25, 0.75\}$  pu illustrated in Figure 30c. Figure 30d shows how many radians the rotor is rotating during this simulation period.

Next in the analysis is the electrical performance. Figure 31a shows the three-phase currents  $i_{abc}$ ,  $i_d$ ,  $i_q$  and  $i_s$  processed in Comsol. Figure 31b shows the flux linkage in the whole period, with the zero-sequence  $\psi_0 \neq 0$  pu also processed in Comsol. It is seen that the flux linkage level decreases with overload. Figure 31c shows how the voltage is increasing with

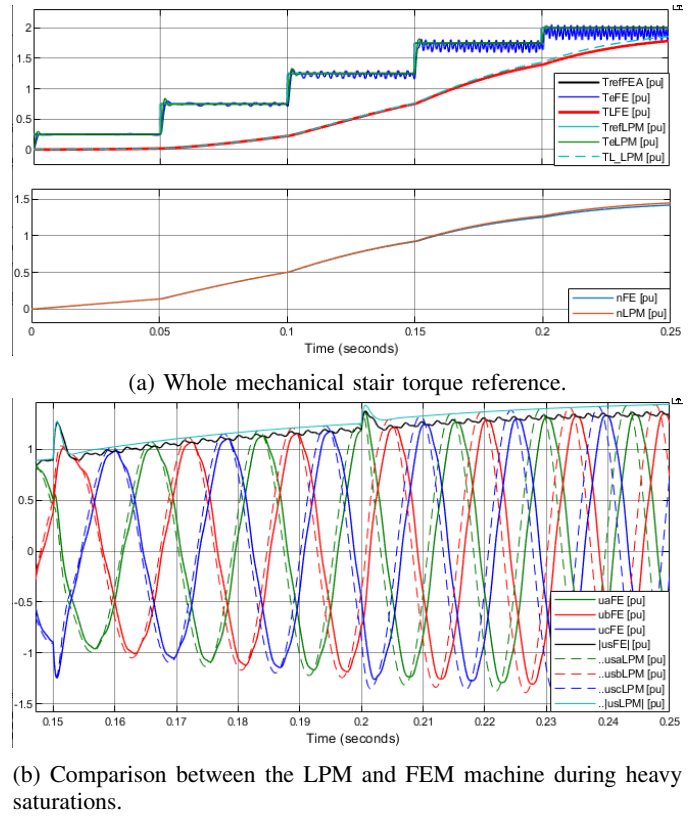


Fig. 23: MTPA Stair

speed. This is illustrated further in Figure 23b/Figure 32a. Figure 31d shows the steady state error in the feedback signal from the current controllers.

Figure 43a shows how  $i_d$  and  $i_q$  changes with the torque step. This is only included for co-simulation time  $t_{CS1}$ , because the scope was not activated during time  $t_{CS2}$ . However, it is assumed that the relation  $i_{dqFEM}/i_{dqref}$  will be approximately equal because it is evident that it is the voltage that is contributing to the underestimation of the torque in several results. It is apparent that  $i_{dFE}$  current will have a transient overshoot for the first ripple periods, before the mean value of  $i_{dFEM}$  is reaching the reference value. Figure 43b shows  $i_d$  and  $i_q$  waves when  $\tau_{eref} = 2.00$  pu is applied. The  $i_{dq}$ -currents are replaced by the voltages in Figure 32a and Figure 32b to illustrate how the voltage is underestimated and lagging compared to the LPM motor. This trend is amplified with higher overload.

Table VII shows the average electromagnetic torque with  $\tau_{eref} = \{0.25, 0.75, 1.25, 1.75, 2.00\}$  pu and the electrical performance at  $\tau_{eref} = \{0.25, 2.00\}$  pu. The waves are measured at the three last periods of the peak ripple before a new step reference is applied. This is to obtain the torque values that are closest to the steady-state values. The load is not reaching steady-state between each new  $\tau_{ref}$  and should, in principle, do this for more accurate results and data.

The electromagnetic performance  $\tau_e$  in Table VII will first be explained. Results from both *CS1* and *CS2* are included for comparison. The average torque  $T_A$  Nm is computed in Comsol in the time interval  $t_1$  s and  $t_2$ . This procedure is

TABLE VII:  $T_A$  is the average torque of the FEM motor,  $T/T_B = T_A/T_{basis}$ ,  $T/T = T_{eFEA}/T_{basis}$ ,  $\tau = \tau_{e,ref}$ ,  $i/i = i_{avg}/i_{ref}$ .

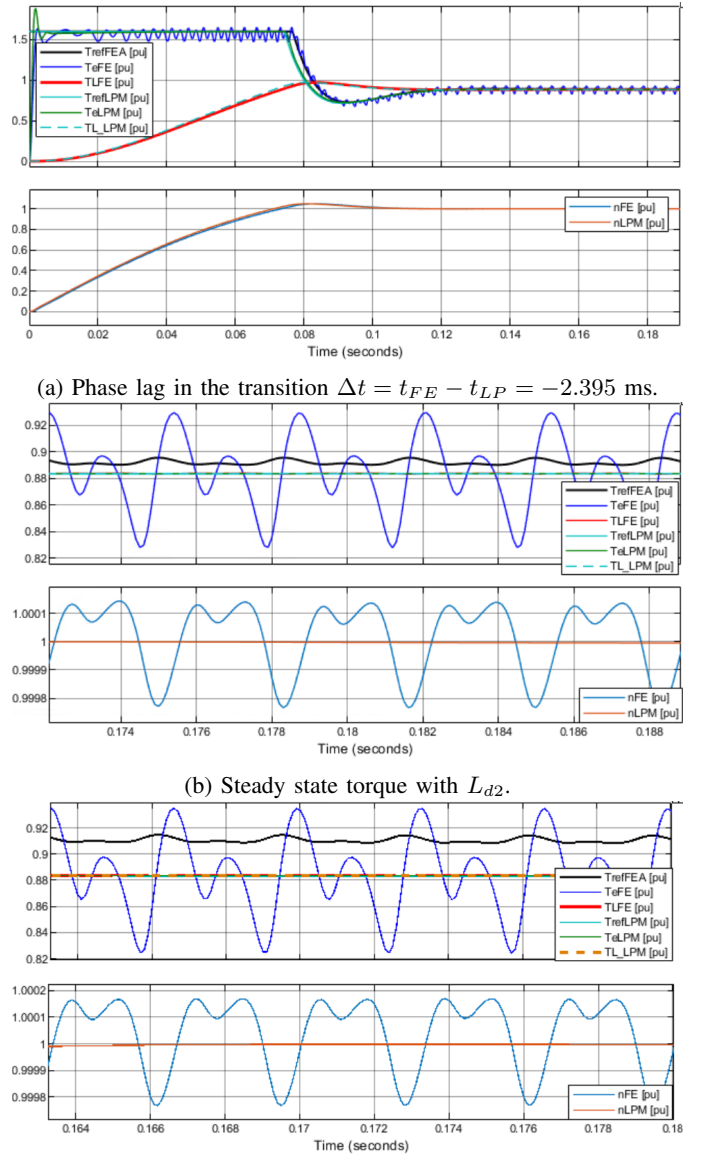
Electromagnetic with $K_{pd2}$						
$\tau$ [pu]	$t_1$ [s]	$t_2$ [s]	$T_A$ [Nm]	$T/T_B$ [pu]	$T/T$ [pu]	
0.25	0.0027	0.0498	8.1012	0.2490	0.998	
0.75	0.0611	0.0981	24.2756	0.7473	0.997	
1.25	0.1357	0.1472	40.0480	1.2329	0.986	
1.75	0.1932	0.1986	55.1080	1.6965	0.970	
2.00	0.2432	0.2479	62.2300	1.9158	0.958	
Electromagnetic with $L_{d1}$						
$\tau$ [pu]	$t_1$ [s]	$t_2$ [s]	$T_A$ [Nm]	$T/T_B$ [pu]	$T/T$ [pu]	
0.25	0.0028	0.0455	8.12020	0.2500	1.000	
0.75	0.0788	0.0983	24.0370	0.7400	0.987	
1.25	0.1362	0.1478	39.1190	1.2043	0.963	
1.75	0.1915	0.1998	53.0890	1.6344	0.934	
2.00	0.2129	0.2155	59.9840	1.8466	0.923	
Electrical with $L_{d1}$						
$i_d$ [pu]	$t_1$ [s]	$t_2$ [s]	$i_{avg}$ [pu]	$i_{ref}$ [pu]	$i/i$ [-]	
2.00	0.2129	0.2155	-9.7176	-9.2241	1.0535	
0.25	0.0028	0.0455	-0.2955	-0.2940	1.0051	
$i_q$ [pu]	$t_1$ [s]	$t_2$ [s]	$i_{avg}$ [pu]	$i_{ref}$ [pu]	$i/i$ [-]	
0.25	0.0028	0.0455	1.85710	1.85460	1.0014	
2.00	0.2129	0.2155	11.5440	11.6715	0.9891	

done for all the other steps-references in Table VII. The ratio  $T/T_B = T_{eFEM}/T_{basis}$  is the pu value of the electromagnetic torque. The ratio  $T/T = T_{eFEM}/T_{eref}$  is included to see how far the torque of the FEM motor is underestimated the reference torque. The torque estimation is clearly improved in the case with  $L_{d1}$  compared to the case with  $L_{d2}$ . At  $\tau_{eref} = 2.00$  pu, the electromagnetic torque is 8.42% lower with  $L_{d2}$  and 15.34% with  $L_{d1}$ . Next is the electrical performance from the case *CS1*. The difference in the average feedback current  $i_{avg}$  and the reference current  $i_{ref}$  is calculated with the ratio  $i/i$  in Table VII.

### G. Speed Control with LPM

This co-simulation compares the step response between the FEM motor and the regular LPM motor in a separate simulation with an equal control system. For this co-simulation Figure 54 with the speed control is used. The LPM model and the FEA motor are applied with a speed reference step signal  $n_{ref} = 1.0$  pu at the same time. The torque limit from the output of the PI-speed controller is  $\tau_{emax} = 1.6$  pu.

Figure 24a/Figure 33a shows the electromagnetic torque and mechanical part of the simulation in the case with *CS2*. Figure 33c shows the transitional phase when the drive is decreasing the reference  $\tau_{eref}$ . The torque reference value in the speed control LPM is starting the torque reduction from 1.6 pu at  $t = 0.07421$  s, while the torque of the FEM motor is starting the torque reduction from 1.6 pu at  $t = 0.07661$  s. That is a time difference between the LPM model and the FEM model of  $\Delta t_2 = 2.395$  ms seen in the transitional phase of the torque for *CS2*. For the first case *CS1* in Figure 33c the difference is 3-5 ms, not accurately measured. However, it is obvious that the FEA motor is lagging the LPM less in the case *CS2*. Figure 33b compares the start of the simulation to get an overview of the response of the applied torque at the inception.



(c) Steady state torque with  $L_{d1}$ . Added to compare the difference in steady-state torque between the two parameters.

Fig. 24: Speed Control with  $n_{ref} = 1.0$  pu.

Figure 24b/Figure 33d shows the electromagnetic performance at steady state. The FEM model is applying the required torque to reach steady state speed  $n_{FE} = n_{ref} = 1.0$  pu, and the reference torque is estimated higher  $\tau_{e,ref} \approx 0.89$  pu to reach this value. The FEM model  $\tau_{eFE}$  is lower than the reference torque by  $\Delta\tau_{e,ref} = 0.0083$  pu. It is also added the torque error from *CS1* in Figure 24c from the simulation with  $L_{d1}$  to show the difference in the steady-state error torque for speed control.

Figure 34a shows that the LPM simulation is leading the phase current of the FEM model. Figure 34b shows the difference between the applied reference voltage to the terminals of the machine. It is also here shown that  $u_{dqLPM}$  is leading  $u_{dqFE}$ .

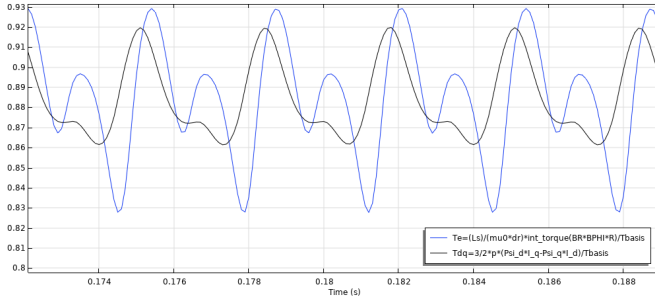


Fig. 25: Arkkio's torque versus torque with the flux linkage equation. Steady state values from a co-simulation post-processed in Comsol.

### H. Speed Control with LPM with Feed-back from FEM

Figure 34c shows the results when it is added an LPM in parallel with the FEM co-simulation. That is, the LPM motor is applied with the same reference values  $u_d$  and  $u_q$  and feedback speed  $n$  as the FEM motor. See the block *LPM in parallel with LiveLink* in Figure 54 for further details. When the torque reference due to the torque limit is  $\tau_{emax} = 1.6$  pu, the peak torque  $\tau_{eLPM||FEM2}/T_{basis} \approx 2.92$  pu for *CS2* in Figure 34c and  $\tau_{eLPM||FEM1}/T_{basis} \approx 3.69$  pu for *CS1* in Figure 45c. This is the results from the same co-simulation in the last subsection with speed control. The results are added to illustrate how the overshoot value in the LPM motor will respond with this connection.

### I. Comparison of Arkkio's method and Co-Energy Torque

Figure 25/Figure 35a is comparing the waves of the steady-state torque calculated with Equation 8 and Equation 9 after the speed controllers is in equilibrium. The plot in Figure 25/Figure 35a is processed in Comsol.

The ripple components between the co-energy method and Arkkio's method are the main difference. This is depicted in Figure 35a. It is used Arkkio's method as the output torque from Comsol to Simulink (to the control system) in all the co-simulations as the torque state variable. It is used an average calculation of the data in Comsol to calculate the average torque in the time interval  $t = 0.16$  s to  $t = 0.18$  s for both Equation 8  $\tau_{Arkkio2} = 0.8835$  pu and Equation 9  $\tau_{dq2} = 0.8844$  pu. It may be a measurement error for  $\tau_{dq2}$ , because the average value was not measured from peak-to-peak. The measurement in  $T_{dq2}$  is actually measured from peak-to-peak. The summarized difference in the torque components is shown in Table VIII. These values are calculated with the operators for maximum, minimum, and average values in Comsol Desktop. Figure 35b is comparing the co-energy principle with a load of  $\tau_{eref} = 2.0$  pu. The average values are not calculated since the motor is not reaching the state of equilibrium.

### J. Harmonic Analysis, Motor Saturation and Inductances

It is also performed a Fourier analysis of the IPMSM in Comsol when  $\tau_{eref} = \tau_n = 0.8835$  pu and  $n = 1.0$  in

TABLE VIII:  $\tau_A$  is the average torque.  $\tau_{max}/\tau_{min}$  is the maximum/minimum points.  $\Delta\tau = \tau_{max} - \tau_{min}$ .

Arkkio's method				Co-energy method			
Name	Symbol	Value	Unit	Name	Symbol	Value	Unit
Avr.	$\tau_A$	0.8833	pu	Avr.	$\tau_A$	0.8844	pu
Max.	$\tau_{max}$	0.9294	pu	Max.	$\tau_{max}$	0.9199	pu
Min.	$\tau_{min}$	0.8277	pu	Min.	$\tau_{min}$	0.8614	pu
Rip.	$\Delta\tau$	0.1017	pu	Rip.	$\Delta\tau$	0.0585	pu
Rip.%	$\Delta\tau/\tau_A$	11.514	%	Rip.%	$\Delta\tau/\tau_A$	6.615	%

Figure 47a to Figure 47d for *CS1*. This is from another co-simulation with extreme current loading of  $\tau_{eref} = 3.0$  pu, for a short time to obtain steady state  $n = 1.0$  pu quickly. It is only the values when  $\tau_e = 0.8835$  pu and the motor is reaching steady state  $n_{FE} = 1.0$  pu that is considered to be important. Further analysis from that particular co-simulation is not included.

Figure 36a-Figure 36c is showing  $\mu_r$  as a function of different current loading for *CS2*. The permeability is calculated in Comsol with  $\mu_r = rmm.normB/(mu0.const * rmm.normH)$ . Figure 36d shows the inductance in mH from the speed control case in Figure 24a. Here it is clear that the inductance values are varying with saturation and rotor position  $x_{dq}(i_d, i_q, \vartheta_m)$ .

## VIII. DISCUSSION

### A. Introduction

The first parts of this chapter is describing a summary of the co-simulation model and strengths with co-simulations. The next parts are discussing the results from the co-simulations. Some results from, e.g., speed control, will be discussed with torque control when this seems logical, although each simulation case, for the most part, is divided into separate subsections. Then the potential and limitations with co-simulation are discussed. After that, the results from the frequency response analysis are discussed.

### B. Modeling for Co-Simulation Summary

This thesis targets a modeling approach for a three-phase IPMSM using the co-simulation software Comsol LiveLink for Simulink. This target is obtained. Further, it is investigated the drives aspect and the dynamic response of an FEA IPMSM connected to a control system in Simulink. It is modeled one pole of the machine in Comsol with anti-periodic boundary conditions [44] to reduce the computational time in the co-simulation. This is needed due to the inherent heavy computational power needed for co-simulation [31], [25], [26], [27]. However, the processor power in this project is not fully utilized due poor documentation of optimal solver setup between Comsol and Simulink in the Comsol LiveLink for Simulink documentation. The length of the machine is modeled with a length of  $d = n_{sect} \cdot L_s$  to obtain the whole active coil length of the machine with only making one pole  $p/2$ . This is possible for the windings in this machine, but the winding configuration in other FEA motors has to be considered when setting up the co-simulation model. The mesh is also targeted to be accurate and at the same time

have coarse elements where this is sufficient. In the **RMM: Coil** domain it is used **Conductor model: Homogenized multivert** with a defined number of stator turns  $N_s = 50$  and  $B_r = 1.24$  T to obtain the no-load voltage  $k_e = 214.1$  V/krpm at rated speed  $N_n = 1000$  RPM. The setting **Coil group** is enabled. It is used **Coil Excitation: Circuit (current)** coil excitation mechanism. This leads to the next step where **External Couplings: External I vs. U** is used to connect **EC** to **RMM**. The **Voltage Source** in **EC** is the source type **DC-source**, where the voltage parameter in phase A  $U_{sa}$  is the input parameter from Simulink to Comsol. This is also the case for phases B and C. This parameter sets a new value for each communication step  $\Delta t_i = dt = 1.0 \cdot 10^{-4}$  calculated from the reference signals from the PI-controllers in Simulink. The control system is in per unit, and the FEM model following the natural laws is modeled in SI-units, each phase is then multiplied with  $U_{basis}$  at the terminals. The additional physics **EC** is used to make an isolated neutral star connected circuit with  $R_N = 1000 \Omega$ . For the rotating domains (rotor) it is used the settings **Rotation type: Specified rotational velocity** and **Rotational velocity expression: General angular velocity**. It is important that the expression **Rotational velocity expression: General angular velocity** is used and not **Rotational velocity expression: Constant angular velocity** to have the same unit in Comsol and Simulink for rotor speed. The angular velocity parameter  $\omega = \omega_r$  and the initial angle  $\alpha_0 = 0^\circ$ . It is extremely important with the correct phase alignment of phase A and the rotor d-axis shown in Figure 8 [4]. The predefined parameter value  $\omega_r$  is the connection point between Simulink and Comsol for the speed, where  $\omega_r$  gets a new reference signal at each communication step  $\Delta t_i = dt = 1.0 \cdot 10^{-4}$  that is calculated from the control system in Simulink. The sum total of input signals from Simulink to Comsol is four, and these are defined as *Global parameters*. The initial values are zero for all input parameters in **Study 1: Stationary Solution**  $\omega_r = 0.0$  rad/s,  $U_{sa} = 0$  V,  $U_{sb} = 0$  V and  $U_{sc} = 0$  V (initial conditions standstill and open circuit). For the output variables from Comsol to Simulink it is used seven measurement probes: Three-phase currents  $I_{ABC}$  in unit A (where it is divided with  $I_{basis}$  before the control system to get per unit values), the torque from Arkko's method  $T_e$  in Nm and three-phase flux linkages  $\Psi_{ABC}$  in Wb. The setup up of the co-simulation experiment is done according to the users manual in the guidelines from Comsol [57],[56], [53].

The control system is built with standard procedures, and a linearized and normalized model of the power converter [8]. The control system used in this thesis is shown in Figure 55. Since it is built a relatively basic co-simulation drive platform with LiveLink for Simulink in this work, it should be feasible to make more complex drives using the procedure in this thesis as a basis.

It is challenging to make a co-simulation model work. However, when the co-simulation model is established, it is easy to apply different motors and co-simulation operational characteristics, allowing for flexible load situations and accurately determining the FEM machine's characteristics, illustrated through the results.

### C. Potential of Co-Simulations

The linearized converter is decoupling any converter harmonics from the spatial harmonics in the machine. Only spatial torque ripples, cogging torque, machine saturation, and machine cross-coupling influence the drive system. Converter torque and current ripples are out of scope. The linearized converter and a continuous control system imply that the voltage references  $u_d$  and  $u_q$  in principle is sinusoidal. Although, time delay constants are added. This is added to include an equivalent real drives systems response.

The co-simulation has targeted varying load conditions to an extent. The LPM model was added for the sake of comparison. A real motor could have been used in addition to compare the results between the FEA, LPM, and real IPMSM. However, a real motor will, in principle, be connected to a converter topology [33]. To compare the results with a real motor, using an inverter and using discrete controllers is a reasonable next step if this project were to be extended.

The tuning of the motor and load was done with regular LPM simulation before the co-simulation with parameters obtained from the FEM tests. The co-simulation approach can mitigate and address some of the limitations with the constant-parameter lumped model drive. This is, for instance, a wrongly estimated voltage requirement from the constant parameter model also mentioned in [25] for an asynchronous drive. In that reference, [25] it is proposed that future co-simulation studies include setting up flux models closer to the machine behavior.

Cogging torque in a motor may be undesired in many applications [47], [27], but the influence of the reluctance and the cogging torque is highlighted in the control system shown in section VII. To use a motor with high cogging and reluctance was discussed from the beginning to evaluate the performance with reluctance. Other PMSM typologies also can be used [35]. The ferromagnetic material was selected close to a typical real motor. End windings resistance and inductance can be added to improve the accuracy of the drive further. It is not considered important in this work [48] but should be used in the future if accurate loss calculations [35] in a dynamic load situation is the goal.

It is possible to include non-linearity, space harmonics, cross-coupling terms by the use of FEA generated look-up tables and avoid performing co-simulation to reduce the simulation time [6]. However, when co-simulation is included, it may be possible to investigate a more accurate dynamic performance, which is not captured if only LUT is used and co-simulation omitted, which is proposed in [6]. A hypothesis is that co-simulation can capture some effects that are not possible to attain with other methods, although this is a highly untested hypothesis. This can for instance be the PM induced current that is oscillating around  $\tau_{e,ref} = 0.0$  pu depicted in Figure 21c. A combination of using LUT and co-simulation may be feasible in the future. This can for instance be methods used in [11, 10, 9, 6].

#### D. Limitations with Co-Simulations

Only a handful of publications on the topic co-simulated in this thesis used 8-36 hours per co-simulation and needed large data storage. Other references also mention these challenges. It seems like LiveLink for Simulink have particular limitations compared to other co-simulation software [7], [14]. It was no instruction on how to model a complex system like IPMSM control in the Comsol documentation. It is not instructed how to set up the solvers in Simulink and Comsol for optimal convergence in co-simulation and the best possible utilization of processor capacity. It was not tried to improve the solvers from the user either. It is also experienced that the FMU software can be further improved. At the start of a co-simulation, the processors used an average 10% of the server CPU. At the end of a, e.g., 0.2 s simulation, the CPU averages below 0.5%. It is assumed that this is because of convergence errors that will increase further in the simulation because of increasing numerical inaccuracies between Comsol and Simulink. A potential source of this can be due to two position integrators (one in Comsol and one in Simulink), although this was tested and is most likely not the case. It is also experienced that the co-simulation takes a particularly long time when other Python users are using 90% of the CPU on the NTNU server. The constant communication time-step solvers are "interrupting" the simulation in each communication time step, making it easier for other software to override LiveLink for other software. This "interruption" appears to diminish its own simulation performance. In [14] the simulation time was 2 hours and the required storage was 8 GB for  $t = 1.0$  s. Comsol has to, in reality, improve their instruction and potentially the software for further use. Several e-mails were sent to Comsol about solving issues with co-simulations, but the reply resolution from Comsol was low. The service provided by Comsol is not the best in this experience.

Although converter design has to be simplified in co-simulations, it is possible to include blanking time and dead time effects in the converters [20]. Fault cases can also be analyzed [16], [20]. Few other references go into detail on how to set up their co-simulation model. An exception is the Ph.D. thesis of *Quintal* [7], not discovered until a few days before the delivery date. *Quintal* also published at least one paper with co-simulation in [14]. Another exception is in the dissertation from *Kanerva* [33], but that approach is not that relevant for the software used in this thesis. The FMU standard is from 2010 [31]. The Flux2D manual from 2010 has a description on how to set up co-simulation for motor control [59].

#### E. MTPA Step Reference

The rise time  $T_{rise}$  is when  $\tau_e$  is crossing  $\tau_{eref} = 0.8835$  pu. This is considered to be the equivalent to 1.0 pu in the torque value, because saturation have to be considered. This is also the equilibrium torque when a reference speed  $n_{ref} = 1.00$  pu is applied seen in the results from speed control. It is noted that the FEM model have a small overshoot in the torque reference for *CS2*, where the LPM model have considerable overshoot of  $\Delta\tau_{pk,LPM2}/\tau_{e,n} = (1.0470 - 0.8835)/0.8835 \cdot 100\% = 18.505\%$ , while  $\Delta\tau_{pk,FEM2}/\tau_{e,n} =$

$(0.9104 - 0.8835)/0.8835 \cdot 100\% = 3.044\%$  in Figure 37a. At the same time the FEM model have a slower dynamic response compared to the LPM model also depicted in Figure 37a and Figure 26b. This is evidently the case for most co-simulations, except for the case when  $\tau_{e,ref} = 1.25$  in Figure 30c. For this particular step the overshoot value of  $\tau_{eFEM2}$  is approximately in line with the overshoot value of  $\tau_{eLPM2}$ . This can be due to the timing of the torque peak at the time.

#### F. MTPA Rated Negative

This load scenario was included to look into the effects of driving the FEM motor to 3<sup>rd</sup> quadrant operation and with zero torque reference in Figure 21b. In this case, the ripple components are mainly induced in the d-axis at low speeds below  $n \approx 0.3$  pu. It is with higher speeds that the ripples appear in both axed seen from the results. The d-axis current is oscillating around the reference in Figure 38b when it is applied a torque reference of  $\tau_{eref} = 0.0$  pu in the last step. For the  $i_{dFE}$ -current, the ripples persist at very low speeds. This is assumed to be the field current excitation from PMs  $\psi_m$  during rotation and no load. This is probably not that important, but it is readily noticed in the results. The frequency of  $i_{dFE}$  around the  $i_{dref} = 0.0$  pu is decreasing with lower speed. The current  $i_{qFE}$  has a similar response as the LPM current. It is also noted that the voltage signal  $\|u_{sFE2}\|$  in the time interval  $t = 0.08$  s to  $t = 0.12$  s is canceling some of its ripple components in Figure 27d. From the case in *CS1* in Figure 38d it seems like the q-axis voltage have the opposing ripples.

#### G. MTPA 1.6 pu and 1.0 Pu

The torque limit  $\tau_{e,max} = 1.6$  pu was included to investigate how the machine will respond in an overload situation that is not unreasonable in real applications. This number is taken from [8]. However  $\tau_{e,max} = 1.6$  pu is almost 2 times the rated torque reference  $\tau_{e,n} = 0.8835$  pu. This could have been reduced to a value of  $\tau_{e,max} = 1.6 \cdot 0.8835 = 1.4$  pu estimated to be more realistic. On the other hand, that will cause a longer co-simulation time not desired.

In Figure 28c the speed from the Comsol motor is  $(n_{FE2} - n_{LPM2})/n_{FE2}(\%) \approx (1.056 - 1.066)/1.056 \cdot 100\% = -0.94\%$  below  $n_{LPM}$ . For the LPM motor  $\tau_{eLPM} = \tau_{eref}$  in both speed control and MTPA control. The underestimate voltage with FOC is also highlighted in *Leonardo et al.* [25] for an induction machine with SV-PWM. An underestimated torque value below the reference is also shown in *Di Leonardo et al.* [28] for a PMSM.

It is important to roughly estimate correct inductance parameters. The phase voltage and phase current is lagging in the FEM model compared to the LPM motor in all results. The delay is happening because of an underestimated value in the  $u_{qFE}$  voltage seen from several simulations. This delay is evident for both the higher speed range in Figure 29a and the lower speed range in Figure 27d. It is shown that the  $u_q$  voltage for the Comsol machine  $u_{qFEM} < u_{qLP}$ . This difference is mostly clear for the  $L_{d1}$  parameter in Figure 40c where  $\Delta u_{q1} = -0.0581$  and  $\Delta u_{q2} = -0.0247$  pu for the

$L_{d2}$ -parameter in Figure 29c. The  $L_{d1}$  results are for the most part included to illustrate and highlight the voltage error and torque error at equilibrium.

Further, the voltage  $u_q$  is dependent on the parameter  $L_d$  shown by the cross-coupling term in Equation 42. The calculated  $L_{d2}$  parameter with a  $-40 \cdot i_d$  current load, yielded evidently a smaller voltage error in the co-simulations which should correspond to be the case since the feed-forward term in Equation 42 is larger. The d-axis voltage error  $\Delta u_{dFE}$  is not that affected by the change in the parameters, seen from Equation 41 and in the results with both *CS1* and *CS2*. This can be because the feed-forward term from the q-axis  $u_{dII} = n \cdot x_q \cdot i_q$  in Equation 42 is approximately equal for  $L_{q1}$  and  $L_{q2}$ .

The presence of speed ripples is seen in both Figure 24b and Figure 39d. When co-simulations with *CS1* was measured that  $\Delta n_F / \Delta t_F = 0.4489$  pu/s in Table VI is probably an exaggeration and measured in the wrong time interval. This error was corrected in the simulation with  $L_{d2}$  and  $\Delta n_F / \Delta t_f = 0.185$  pu/s with the measured interval shown in Figure 28d.

It is an error to use a 1.0 pu torque reference to compare the voltage requirements, and the reference value that should have been used is a torque reference 0.8835 pu, since this is the rated torque. The 1.6 pu to 1.0 pu test was the first test, and this issue was not thoroughly investigated at the time.

#### H. MTPA Stair

This section illustrates how the FEM machine is responding when unsaturated and when heavily saturated. It is depicted in Figure 23a that the electromagnetic torque  $\tau_e$  never is operating in steady-state. This is because  $\tau_L \neq \tau_{e,ref}$ . In addition, it is observed that the electromagnetic torque is also declining slightly after the sub-transient in each new step. This is a limitation of the results. It was done a trade-off between steady-state values and performing a simulation with stair load. It is also included a plot of the rotor position that shows how short the rotor is rotating in reality due to the short simulation time Figure 30d.

From Table VII key performance of the machine is considered. Here it is apparent that although the current magnitude in the FEM machine is approximately equal to the LPM machine, the motor is not able to reach a torque reference  $\tau_{eref} = 2.0$  pu. It is the voltage requirements that are too low in the q-axis. This is seen from comparing the FEA model with the LPM motor in several results. Unfortunately, the  $i_{dq}$ -current results were not obtained in *CS2*. It is, however, assumed it would be a similar response in the drive for *CS2*. It is also observed that the flux linkage is getting lower for each time the torque reference is higher in Figure 31b, further validating the effect of saturation in the FEM model.

#### I. Speed Control

In the case where speed control is applied in Figure 24b the reference torque is higher than the electromagnetic torque from Comsol  $\tau_{eFE} \approx 0.8835$  to reach  $n_{ref} = n_{FE} = 1.0$  pu. The speed transition from 1.6 pu to 1.0 pu will be lagging

less with the new parameter  $L_{d2}$  in Figure 29a compared to the old parameter  $L_{d1}$  Figure 40a.

#### J. Parameters

It is proposed to calculate  $L_{d2} = 30.8030$  mH/ $x_{d2} = 0.2072$  pu with  $i_{d1} = -0.4$  pu and  $L_{q2} = 53.6110$  mH with and  $i_{q2} \approx 0.9$  pu in Comsol opposed to  $10 \cdot \%I_s$  loading mentioned *Bianchi* [37] for the motor in this work. That particular load situation was estimated from Figure 37b. This was determined from realizing that the parameters calculated with  $I_d = 100\%I_s$  or  $I_q = 100\%I_s$  made  $L_d$  a saturated value, and hence what appears to be a poor dynamic response. The overshoot value with  $L_{d1}$  was  $\tau_{eFEM1} = -0.995\%$ , while  $\tau_{eLPM1} = 25.900\%$ . The wrong parameter is assumed to be the cause of the larger under-estimated voltage where  $\Delta u_{q2}/u_{qLPM} = (0.9134 - 0.9381)/0.9381 \cdot 100\% = -2.63\%$  and  $\Delta u_{q1}/u_{q1LPM} = (0.88 - 0.9381)/0.9381 \cdot 100\% = -6.19\%$ . It makes sense to use the LPM voltage requirement in the denominator, because the control system is based on the constant LPM model. The computed  $L_{d2}$  parameter was increased by  $\Delta L_d/L_{d1} \cdot 100\% = (30.803 - 23.4034)/23.4034 \cdot 100\% = 31.60\%$ . The  $L_{q2}$  parameter was increased by  $\Delta L_q/L_{q1} \cdot 100\% = (53.6110 - 53.0932)/53.0932 \cdot 100\% = 0.98\%$ . The different  $L_q$  parameter is considered to have a negligibly influence in the drive.

An alternative approach is to use LUTs for a more accurate calculation dependent on the saturation level and rotor position. LUTs have not been considered in this work. This is because of the project time and scope. LUTs should be considered in the future for co-simulation for a more accurate description of the magnetic circuit in the control system, thus mentioned [6]. The torque have a lower steady-state error with  $L_{d2}$  shown in Figure 24b and Figure 24c. It is also assumed that reluctance torque, slotting, rotor topology, and other design factors can contribute to underestimating the voltage level. This is mentioned in [6].

For the idealized linear system with the gain parameter  $x_d$  in Equation 49 will cancel out the  $x_d$  term in the denominator in  $h_{oid}(s)$  in Equation 51. However, the results show that the inductance will be changed with different current loading and rotor position shown in Figure 36d. The controller parameter  $x_{dPI}$  is constant while varies with  $x_{dFEM}(i_d, i_q, \vartheta_m)$ . Since the first calculated  $L_{d1}$  used in the PI controller is lower than the actual inductance value from the FEA motor when the applied  $i_{dref} = -0.4$  pu, this will cause a slower response due to a lower gain in the d-axis, readily verified in the comparison between  $L_{d1}$  and  $L_{d2}$ . This comparison is highlighted because this was an issue and misinterpretation for a long time in this thesis. It is also a realization of how important it is to select the correct magnetic parameters for co-simulation.

#### K. Frequency Response, Stability and Switching Frequency

It is performed a stability analysis of  $h_{oid}(s)$ ,  $h_{oiq}(s)$  and  $h_{0,n}(s)$ . The purpose of these results is to investigate if the systems are stable with the tuning. First of all, the inner loop is discussed. The d-axis open-loop system  $h_{oid}(s)$  is analysed in the Bode diagram of Figure 20a. The phase margin is above the



minimum requirement of  $\angle h_{oid}(j\omega_{0dB}) = 65.5^\circ$  for the torque control. The bandwidth is also sufficient. In a real system, the phase margin will eventually have a more negative phase than  $\angle h_{oid}(s) < -180^\circ$  for higher frequencies. Hence a gain margin will never reach infinity [38]. However for the phase margin for the speed loop  $\angle h_{0,n}(j\omega_{0dB})$  is below  $45^\circ$ . This will cause a larger overshoot. The OS can be decreased by decreasing increasing the parameter  $\beta$ . This is not needed since the system is stable seen in the results and Nyquist diagram in Figure 20b, and a higher  $\beta$  will cause a lower bandwidth. Nothing in the results from the co-simulation is implying that the system is at the limit of instability. It is recommended to investigate the drive response with regular LPM simulation before using co-simulation. The frequency response analysis is also only including the unsaturated, fundamental wave motor and is not the frequency response of the FEM model. In addition to this, the transfer functions are derived from zero-speed. Cross-coupling is by then disregarded [8]. However, for stability analysis, one can decouple the disturbance [38].

The switching frequency  $f_{sw}$  has been used from the start of the thesis and for all the results. The tuning and investigating the effects of this parameter on the co-simulation is not investigated and should be done in the future. A higher switching frequency  $f_{sw}$  means that  $\Delta t_i$  have to be reduced [31]. This approach was tried on some occasions and lead to inaccuracy in the co-simulations. It was then decided that  $f_{sw} = 1000$  Hz should be used to avoid the further trial-and-error of a  $\Delta t_i < 1 \cdot 10^{-4}$  s. A smaller communication time step will further increase the co-simulation time and the number of simulation points, i.e., more data stored. Because of data storage levels and poor utilization of the NTNUs servers CPU, it was decided to use a lower switching frequency/eigenvalue [31]. It is noted that the resonance frequency of the current loop  $\omega_0 = 1325.8$  1/s is close to the switching frequency. This should be avoided, and the switching frequency could be increased to, for instance, 5.0 kHz for this machine [49].

## IX. CONCLUSION

### A. Conclusion

It is explained a method to perform a motor drive co-simulation with a 2D FEA IPMSM. The software that is used is Comsol LiveLink for Simulink. The method is described in detail in the combination of section II, section V and section VI. It is also written a summary of the modeling approach in section VIII. It is not known of any similar Comsol LiveLink for Simulink projects covering motor control prior to this project. To write a detailed modeling approach for co-simulation is considered to be the main target in this thesis. The results highlight the difference using a more accurate FEA motor representation compared to the equivalent conventional idealized LPM model of the same IPMSM drive. The two drive models are compared in most of the results.

It is used a linearized model of a power electronic converter with the first-order transfer function  $1/(1 + T_{delay} \cdot s)$  and continuous controllers. The applied reference voltages are, in principle, sinusoidal. The influence on current ripples and torque ripples generated from PWM converters on the motor

drive is not included. This enables decoupling of the space harmonics in the machine and the harmonics from the PWM signal in the converter. Effect of saturation in the ferromagnetic material, cross-coupling between the d- and q- axis, cogging torque, and reluctance torque from the machine is seen in the results.

The PI controllers with constant parameters are unable to estimate a high enough voltage when reaching a more saturated state. This is causing a deviation between the reference torque and the electromagnetic torque. This further translates into a lower speed in the FEM model compared to the LPM motor. This again is causing the phase voltage and phase current of the FE motor to be lagging the LPM motor. This is seen both in MTPA control and speed control. The dynamic response when new reference signals are applied to the FE motor is generally slower than the response in the LPM motor.

An accurate calculation of the controller parameters is needed for co-simulations. It is concluded that the parameter  $L_{d1}$  was estimated to be too low because this parameter was calculated while saturated. The solution to mitigate this error was discovered after all the results from the first co-simulation round were completed and the discussion nearly completed. The new parameter  $L_{d2} = 30.8039$  mH and  $L_{q2} = 53.6110$  mH was recomputed, and the co-simulations had to be performed for a second time. The calculated  $L_{d2}$  parameter increased with 31.61% compared to  $L_{d1}$ . The increase in  $L_{q2}$  from  $L_{q1}$  is 0.97%, assumed negligible.  $L_{d2}$  and  $L_{q2}$  were calculated in the finite element software by loading the machine with  $i_{dref} = -0.4$  pu and  $i_{qref} = 0.9$  pu, respectively. This current load was determined by looking at the reference  $i_{dq}$  in Figure 38b. The new parameter improved the voltage from  $-6.19\%$  to  $-2.63\%$  underestimation of the FEM model compared to the LPM model when reference torque  $\tau_{e,ref} = 1.0$  pu. This is an improved voltage accuracy of 3.56%, further reducing the torque and speed errors.

It is further seen that the FEM model is dependent on saturation, most apparent when a heavy torque reference is used up to  $\tau_{eref} = 2.0$  pu. The average FEM model torque is  $\tau_{eFEM2} \approx 1.92$  pu,  $\tau_{eFEM1} \approx 1.85$  pu while the LPM model torque  $\tau_{eLPM} = 2.00$  pu. The deviation between the LPM and FEA motor is negligible in an unsaturated state with an applied torque reference of  $\tau_{e,ref} = 0.25$  pu. Ripples components from the FEA motor are small in the speed range below  $n \approx 0.3$  pu.

Although limitations with co-simulation motor control are only a handful of references, high amount of required data storage, convergence problems further out in the simulation, simulation time, and a need to simplify converters and controllers, co-simulation can offer interesting design approaches in the future and potentially limit the number of prototypes to be tested in the design phase. Co-simulation is including not negligible non-linearities from the motor in dynamic drives simulations seen in the results. It was challenging to build the co-simulation model because it was practically no references within drives co-simulations. It is obvious that Comsol is required to improve the documentation and support regarding numerical co-simulation solver implementation and computer utilization. Nevertheless, Comsol LiveLink for Simulink can

be a feasible tool for accurate drive systems designs in the future. After the model was established, it was easy to apply various load situations for the FEM LiveLink motor. The bidirectional FMU interface between Comsol and Simulink allows using the flexible post-processing tool in Comsol.

Stability analysis and a frequency response analysis of the idealized open-loop system of the current controllers and the speed controllers have been performed.

### B. Further Work

Further work is to

- 1) Include a three-phase inverter with switches in a dynamic analysis for additional torque ripples, current ripples, and additional converter losses.
- 2) Use co-simulation to investigate electromagnetic losses in a dynamic drive situation.
- 3) Use co-simulation in, e.g., long step-out drives if effects on cables are to be evaluated.
- 4) Include discrete controllers.
- 5) Use co-simulation for sensorless control.
- 6) Use flux weakening with co-simulation since flux-weakening is one motivation to use IPMSM.
- 7) Connect the advanced drive developed in the Power Electronic System and Component group on NTNU with Comsol LiveLink for Simulink. However, it is assumed that the drive model is too difficult for LiveLink for Simulink. A simpler idealized converter without the complex Matlab algorithm may be suitable for co-simulation.
- 8) Improve the IPMSM model used in this thesis to be delta connected with the same  $L_{dq}$ -parameters that are on the drive nameplate in the NTNU-laboratory.
- 9) Set up solvers in a more optimal way for co-simulation between Comsol and Simulink to ensure better convergence, stability, optimal CPU use, and optimal storage.
- 10) For NTNU students: Reproduce the model in this thesis, and make the motor more correct with the one in the lab.
- 11) Look into possibilities to integrate look-up tables in the control system with corresponding  $i_d$ , and  $i_q$  loading since a motivation of doing co-simulation is for better control system design.

### ACKNOWLEDGMENT

Most of all, I want to acknowledge that supervisor Robert Nilssen's knowledge of FEM rotating electrical machines, many hours of cooperation during troubleshooting and suggesting solutions are very important reasons for realizing the co-simulation model.

Roy Nilsen and Aravinda Perera for being willing to be co-supervisors in this co-operation project between the PESC and EME group and giving the advanced PESC drive model on request.

Astrid Røkke and Stev Skaar from Rolls-Royce Electrical Norway for solutions on electromagnetic modelling the past year.

Dominik Häger and Morten Flå for opening the IPMSM motor in the NTNU laboratory.

Raghendra Tiwari for sending the Simulink model from the exercise about PMSM in TET4120.

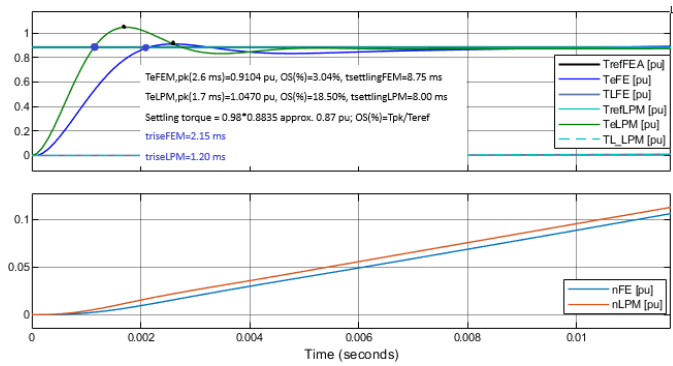
### REFERENCES

- [1] Gianmario Pellegrino et al. "Performance Comparison Between Surface-Mounted and Interior PM Motor Drives for Electric Vehicle Application". In: *IEEE Transactions on Industrial Electronics* 59.2 (2012), pp. 803–811. DOI: 10.1109/TIE.2011.2151825.
- [2] Silong Li et al. "High-Speed Electric Machines: Challenges and Design Considerations". In: *IEEE Transactions on Transportation Electrification* 2.1 (2016), pp. 2–13. DOI: 10.1109/TTE.2016.2523879.
- [3] Giorgio Sulligoi, Andrea Vicenzutti, and Roberto Menis. "All-Electric Ship Design: From Electrical Propulsion to Integrated Electrical and Electronic Power Systems". In: *IEEE Transactions on Transportation Electrification* 2.4 (2016), pp. 507–521. DOI: 10.1109/TTE.2016.2598078.
- [4] Juha Pyrhonen, Valeria Hrabovcova, and R. Scott Semken. *Electrical Machine Drives and Control. An Introduction*. First Edition. Chichester, United Kingdom: John Wiley & Sons, Ltd., 2016, pp. 1–527. ISBN: 9781119260455.
- [5] Jacek F. Gieras. *Permanent Magnet Motor Technology: Design and Application*. Third Edition. CRC Press Taylor & Francis Group, 2010, p. 603. ISBN: 978-1-4200-6440-7 (Hardback).
- [6] Silong Li, Di Han, and Bulent Sarlioglu. "Modeling of Interior Permanent Magnet Machine Considering Saturation, Cross Coupling, Spatial Harmonics, and Temperature Effects". In: *IEEE Transactions on Transportation Electrification* 3.3 (2017), pp. 682–693. DOI: 10.1109/TTE.2017.2679212.
- [7] Roberto Quintal. "Operation and faults analysis of energy-saving permanent magnet synchronous generator for small wind turbine". PhD thesis. Jan. 2020. DOI: 10.13140/RG.2.2.27528.03847.
- [8] Roy Nilsen. *TET4120 Electric Drives Compendium*. 1st edition. NTNU - Department of Electric Power Engineering, 2018, p. 255.
- [9] Marko Hinkkanen et al. "Observers for Sensorless Synchronous Motor Drives: Framework for Design and Analysis". In: *IEEE Transactions on Industry Applications* PP (July 2018), pp. 1–1. DOI: 10.1109/TIA.2018.2858753.
- [10] M. Hinkkanen et al. "Sensorless self-commissioning of synchronous reluctance motors at standstill". In: *2016 XXII International Conference on Electrical Machines (ICEM)*. 2016, pp. 1174–1180. DOI: 10.1109/ICELMACH.2016.7732673.
- [11] N. Bedetti, S. Calligaro, and R. Petrella. "Stand-Still Self-Identification of Flux Characteristics for Synchronous Reluctance Machines Using Novel Saturation Approximating Function and Multiple Linear Regression". In: *IEEE Transactions on Industry Applications* 52.4 (2016), pp. 3083–3092. DOI: 10.1109/TIA.2016.2535413.

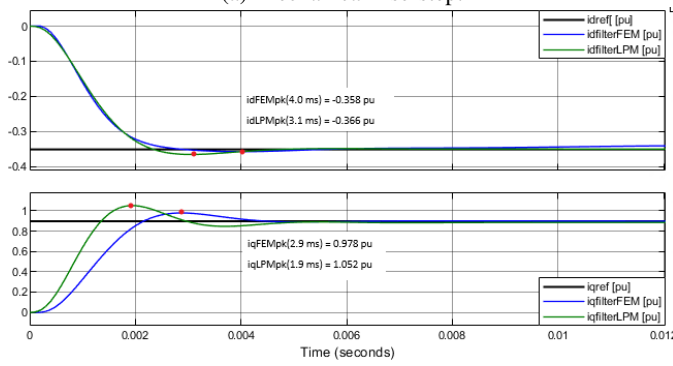
- [12] Gaizka Almandoz et al. “Matlab-Simulink Coupling to Finite Element Software for Design and Analysis of Electrical Machines”. In: Sept. 2012, pp. 161–184. ISBN: 978-953-51-0751-4. DOI: 10.5772/46476.
- [13] G. Scelba et al. “A co-simulation platform for evaluation of sensorless control techniques for IPMSMs”. In: *The XIX International Conference on Electrical Machines - ICEM 2010*. 2010, pp. 1–7. DOI: 10.1109/ICELMACH.2010.5607912.
- [14] Roberto Quintal, Maciej Gwoździewicz, and M. Dybkowski. “Modelling and co-simulation of a permanent magnet synchronous generator”. In: *COMPEL - The international journal for computation and mathematics in electrical and electronic engineering ahead-of-print* (July 2019). DOI: 10.1108/COMPEL-12-2018-0501.
- [15] C. M. Apostoia. “AC machines and drives simulation platform”. In: *2013 International Electric Machines Drives Conference*. 2013, pp. 1295–1299. DOI: 10.1109/IEMDC.2013.6556308.
- [16] C. M. Apostoia. “Multi-domain system models integration for faults detection in induction motor drives”. In: *IEEE International Conference on Electro/Information Technology*. 2014, pp. 388–393. DOI: 10.1109/EIT.2014.6871795.
- [17] Constantin M. Apostoia and Mihai Cernat. “Fault detection in synchronous motor drives, a co-simulation approach”. In: *2015 Intl Aegean Conference on Electrical Machines Power Electronics (ACEMP), 2015 Intl Conference on Optimization of Electrical Electronic Equipment (OPTIM) 2015 Intl Symposium on Advanced Electromechanical Motion Systems (ELECTROMOTION)*. 2015, pp. 617–622. DOI: 10.1109/OPTIM.2015.7426970.
- [18] Muhammad Salman. “Analysis, design and control aspects of linear machines using co-simulations”. Royal Institute of Technology. Department of Electrical Energy Conversion., 2012.
- [19] Peter Makolo. “Wind generator co-simulation with fault case analysis”. Chalmers University of Technology, 2013.
- [20] Yemna Bensalem and Abdelkrim Mohamed Naceur. “Modeling and Simulation of Induction Motor based on Finite Element Analysis”. In: *International Journal of Power Electronics and Drive Systems (IJPEDS)* 7 (Dec. 2016), p. 1100. DOI: 10.11591/ijpeds.v7.i4.pp1100-1109.
- [21] M. Ruba et al. “Analysis of a switched reluctance machine for EV application with torque smoothing strategy”. In: *2015 International Conference on Electrical Drives and Power Electronics (EDPE)*. 2015, pp. 266–271. DOI: 10.1109/EDPE.2015.7325304.
- [22] Lorand Szabo and Mircea Ruba. “Study of Light Electric Vehicles Propulsion Solutions by Means of Finite Element Method Based Co-Simulations”. In: Oct. 2014. DOI: 10.1109/CINTI.2014.7028710.
- [23] F. Parasiliti, M. Villani, and A. Tassi. “Dynamic Analysis of Synchronous Reluctance Motor Drives Based on Simulink® and Finite Element Model”. In: *IECON 2006 - 32nd Annual Conference on IEEE Industrial Electronics*. 2006, pp. 1516–1520. DOI: 10.1109/IECON.2006.347814.
- [24] Bing Hang et al. “Co-simulation of field oriented control in induction motor drive system”. In: *2016 IEEE 11th Conference on Industrial Electronics and Applications (ICIEA)*. 2016, pp. 1955–1958. DOI: 10.1109/ICIEA.2016.7603908.
- [25] L. Di Leonardo et al. “Finite Elements Model Co-Simulation of an Induction Motor Drive for Traction Application”. In: *IECON 2019 - 45th Annual Conference of the IEEE Industrial Electronics Society*. Vol. 1. 2019, pp. 1059–1065. DOI: 10.1109/IECON.2019.8926853.
- [26] C. Schulte and J. Böcker. “Co-simulation of an electric traction drive”. In: *2013 International Electric Machines Drives Conference*. 2013, pp. 974–978. DOI: 10.1109/IEMDC.2013.6556215.
- [27] C. Schulte and J. Böcker. “Co-simulation of an interior permanent magnet synchronous motor with segmented rotor structure”. In: *IECON 2014 - 40th Annual Conference of the IEEE Industrial Electronics Society*. 2014, pp. 437–442. DOI: 10.1109/IECON.2014.7048537.
- [28] L. Di Leonardo et al. “Transient analysis of PM synchronous motor drives by finite element model co-simulation”. In: *IECON 2013 - 39th Annual Conference of the IEEE Industrial Electronics Society*. 2013, pp. 6834–6840. DOI: 10.1109/IECON.2013.6700264.
- [29] Muhammad Irfan et al. “A design of electrical permanent magnet generator for rural area wind power plant”. In: *International Journal of Power Electronics and Drive Systems* 9 (Mar. 2018), pp. 269–275. DOI: 10.11591/ijpeds.v9n1.pp269-275.
- [30] Sung Chan Ahn, Jung Ho Lee, and Dong Seok Hyun. “Dynamic characteristic analysis of LIM using coupled FEM and control algorithm”. In: *IEEE Transactions on Magnetics* 36.4 (2000), pp. 1876–1880. DOI: 10.1109/20.877811.
- [31] Severin Sadjina et al. “Distributed Co-simulation of Maritime Systems and Operations”. In: *Journal of Offshore Mechanics and Arctic Engineering* 141.1 (Sept. 2018). 011302. ISSN: 0892-7219. DOI: 10.1115/1.4040473. eprint: [https://asmedigitalcollection.asme.org/offshoremechanics/article-pdf/141/1/011302/6374941/omae\\_141\\_01\\_011302.pdf](https://asmedigitalcollection.asme.org/offshoremechanics/article-pdf/141/1/011302/6374941/omae_141_01_011302.pdf). URL: <https://doi.org/10.1115/1.4040473>.
- [32] Lars Ivar Hatledal et al. “A Language and Platform Independent Co-Simulation Framework Based on the Functional Mock-Up Interface”. In: *IEEE Access* 7 (2019), pp. 109328–109339. DOI: 10.1109/ACCESS.2019.2933275.
- [33] Sami Kanerva. “Simulation of Electrical Machines, Circuits and Control Systems Using Finite Element Method and System Simulator”. PhD thesis. Helsinki University of Technology. Department of Electrical and Communications Engineering., 2005. ISBN: 951-22-7610-0. URL: <http://lib.tkk.fi/Diss/2005/isbn9512276100/>.

- [34] Mariusz Jagiela and Tomasz Garbiec. "Coupling electromagnetic (FE) models to multidomain simulator to analyse electrical drives and complex control systems". In: *Archives of Electrical Engineering* 59 (Dec. 2010). DOI: 10.2478/s10171-010-0015-y.
- [35] Kristoffer Stabell Andersson. "Power Dense High Speed Motor for Air-Craft Propulsion using COMSOL Multiphysics". Specialization project. Norwegian University of Science, Technology. Faculty of Information Technology, and Electrical Engineering. Department of Electric Power Engineering, 2020.
- [36] Juha Pyrhonen, Tapani Jokinen, and Valeria Hrabovcova. *Design of Rotating Electrical Machines*. Second Edition. New Delhi, India: John Wiley & Sons, Ltd., 2014, pp. 1–584. ISBN: 978-81-265-6560-3.
- [37] Nicolas Bianchi. *Electrical Machine Analysis Using Finite Element Method*. Second Edition. The United States of America, Boca Raton: Taylor & Francis Group, 2005, pp. 1–584. ISBN: 0-8493-3399-7.
- [38] Jens G. Balchen, Trond Andresen, and Bjarne A. Foss. *Reguleringsteknikk*. 6th Edition. NTNU Institutt for teknisk kybernetikk (Print by: NTNU Grafisk Senter), 2016, p. 611. ISBN: 978-82-7842-202-1.
- [39] Olga Tolochko. "Energy Efficient Speed Control of Interior Permanent Magnet Synchronous Motor". In: Feb. 2019. ISBN: 978-1-78984-826-7. DOI: 10.5772/intechopen.80424.
- [40] Liuping Wang et al. *PID and Predictive Control of Electrical Drives and Power Converters using MATLAB / Simulink*. First Edition. New Delhi, India: John Wiley & Sons Singapore Pte.T, Ltd., 2015, pp. 1–584. ISBN: 9781118339442.
- [41] Lesics. *Tesla Model 3's motor - The Brilliant Engineering behind it*. YouTube. December 18th 2020. URL: <https://www.youtube.com/watch?v=esUb7Zy5Oio>.
- [42] *AC/DC Module*. COMSOL Multiphysics. 2020. URL: <https://doc.comsol.com/5.6/doc/com.comsol.help.acdc/ACDCModuleUsersGuide.pdf>.
- [43] Robert Nilssen. *Professor supervisor*. 01-06/2021.
- [44] COMSOL Multiphysics 5.5. *Generator in 2D (Online)*. COMSOL Multiphysics. 2020. URL: [https://www.comsol.com/model/download/629771/models.acdc.generator\\_2d.pdf](https://www.comsol.com/model/download/629771/models.acdc.generator_2d.pdf).
- [45] Astrid Røkke and Stev Skaar. *Meetings*. 01-03/2021.
- [46] *Neodymium Iron Boron Magnet Catalog*. Arnold Magnetic Technologies. URL: <https://www.arnoldmagnetics.com/wp-content/uploads/2019/06/Arnold-Neo-Catalog.pdf>. (Downloaded: 03/15/2021).
- [47] Njål Rotevatn. "Design and testing of Flux Switched Permanent Magnet (FSPM) Machines". Norwegian University of Science, Technology. Faculty of Information Technology, and Electrical Engineering. Department of Electric Power Engineering, 2009.
- [48] Stanislav Kocman, Petr Orsag, and Pavel Pecinka. "Simulation of Selected Induction Motor Operating Conditions Using COMSOL Software". In: *Advances in Electrical and Electronic Engineering* 16 (Sept. 2018). DOI: 10.15598/aeec.v16i3.2824.
- [49] Aravinda Perera and Roy Nilsen. "A Sensorless Control Method for IPMSM with an Open-Loop Predictor for Online Parameter Identification". In: *2020 23rd International Conference on Electrical Machines and Systems (ICEMS)*. 2020, pp. 1983–1988. DOI: 10.23919/ICEMS50442.2020.9290964.
- [50] A. Perera and R. Nilsen. "A Framework and an Open-Loop Method to Identify PMSM Parameters Online". In: *2020 23rd International Conference on Electrical Machines and Systems (ICEMS)*. 2020, pp. 1945–1950. DOI: 10.23919/ICEMS50442.2020.9291135.
- [51] Texas Instruments. *Keynote: Designing Permanent Magnet Motors for Sustainable Transport*. Texas Instruments. URL: <https://www.ti.com/lit/an/bpra048/bpra048.pdf>.
- [52] Shoudao Huang et al. "Maximum torque per ampere and flux-weakening control for PMSM based on curve fitting". In: *2010 IEEE Vehicle Power and Propulsion Conference*. 2010, pp. 1–5. DOI: 10.1109/VPPC.2010.5729024.
- [53] COMSOL Multiphysics. *LiveLink™ for Simulink® - User's Guide*. 2020, pp. 1–60.
- [54] Circuitlab. *Circuitlab*. Circuitlab. URL: <https://www.circuitlab.com/>.
- [55] *COMSOL Documentation (Online)*. COMSOL Multiphysics. 2020. URL: [comsol.com](https://www.comsol.com).
- [56] COMSOL Multiphysics. *Introduction to LiveLink for Simulink*. URL: <https://doc.comsol.com/5.6/doc/com.comsol.help.lsimulink/IntroductionToLiveLinkForSimulink.pdf>. (accessed: 22.01.2021).
- [57] *Introduction to LiveLink™ for Simulink®. Video*. COMSOL Multiphysics. URL: <https://www.comsol.com/video/introduction-to-livelink-for-simulink>. (Accessed online: 04.01.2020).
- [58] COMSOL Multiphysics. *Integrate COMSOL Multiphysics into Simulink with LiveLink for Simulink*. URL: <https://www.comsol.com/livelink-simulink>. (accessed: 26.02.2021).
- [59] *New features regarding co-simulation Flux-Simulink*. Cedrat's Flux. 2010. URL: <http://www.tianyuantech.com/download/Simulink.pdf>.

APPENDIX A  
CO-SIMULATION RESULTS

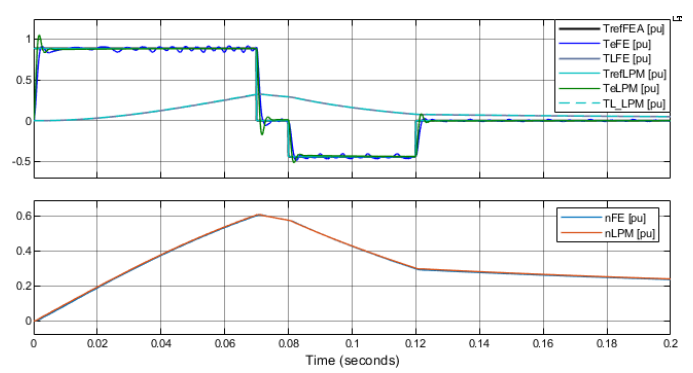


(a) Mechanical rise step.

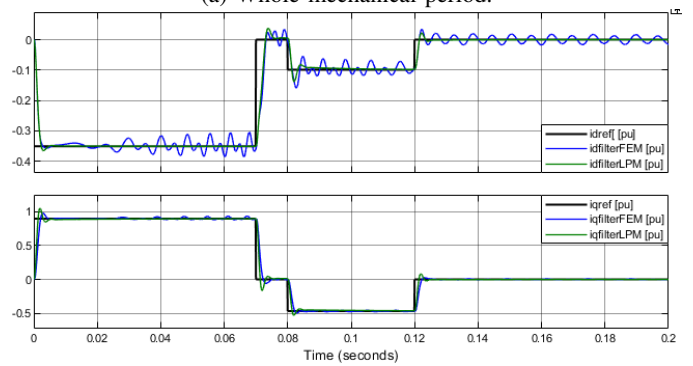


(b) Current rise steps. Peak values indicated with orange dots.

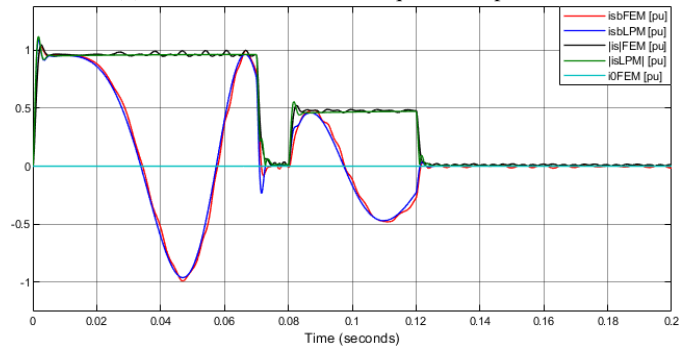
Fig. 26: Start with step reference  $\tau_{e,n} = T_n/T_{basis}$  with  $L_{d2}$ .



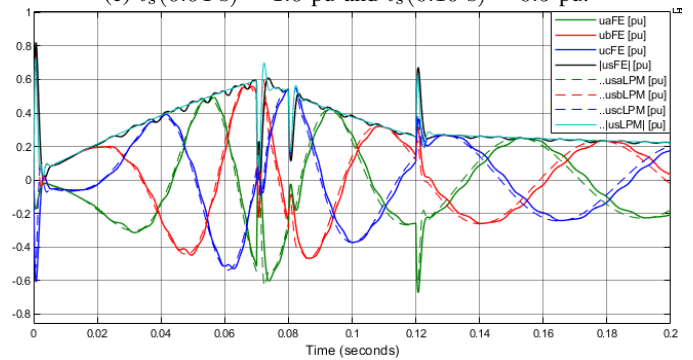
(a) Whole mechanical period.



(b) Current waves with 3<sup>rd</sup> quadrant operation.

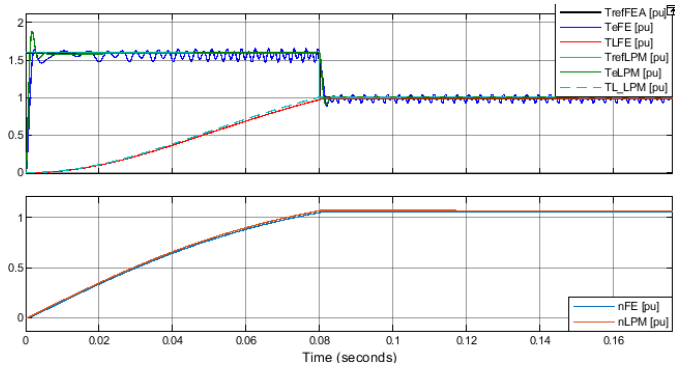


(c)  $i_s(0.04 \text{ s}) \approx 1.0 \text{ pu}$  and  $i_s(0.10 \text{ s}) \approx 0.5 \text{ pu}$ .

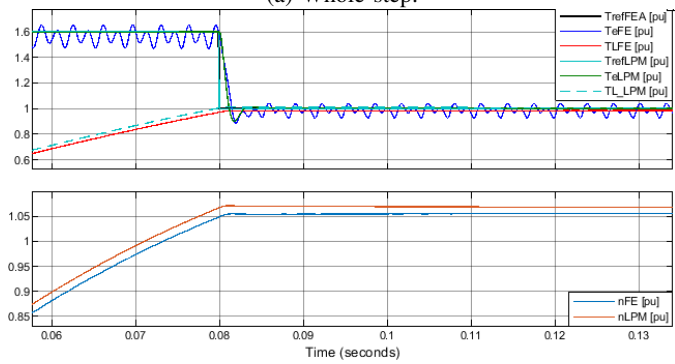


(d) Opposing voltage ripples of  $u_q$  between  $t = \{0.08\text{s}, 0.21\text{s}\}$ .

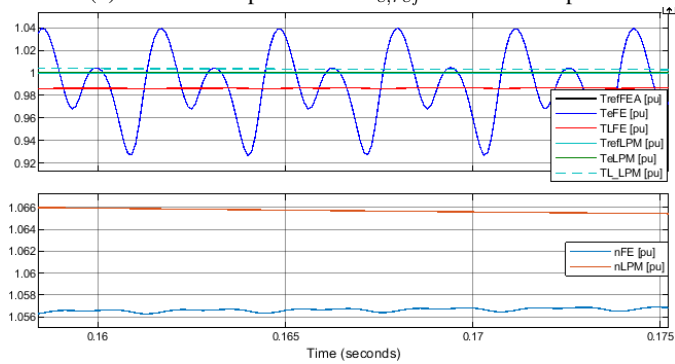
Fig. 27: Rated Step and Negative Torque with  $L_{d2}$ .



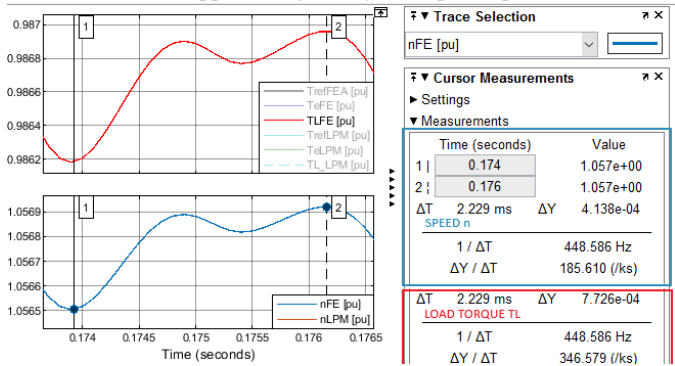
(a) Whole step.



(b) Transitional phase from  $\tau_{e,ref} = 1.6 \rightarrow 1.0$  pu.

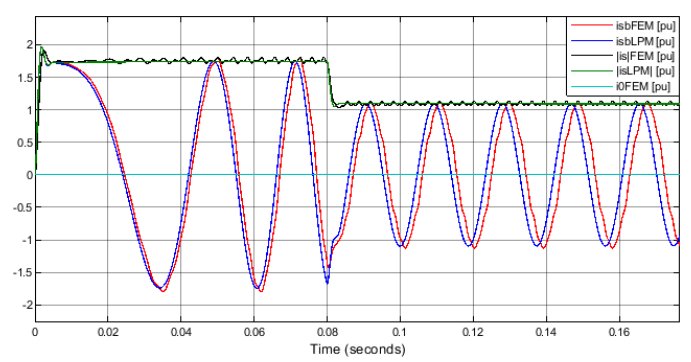


(c) Approaching steady state pu torque.

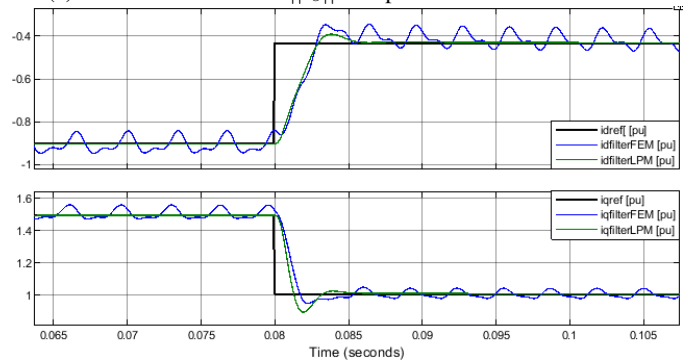


(d) Derivative of the speed approaching steady state.

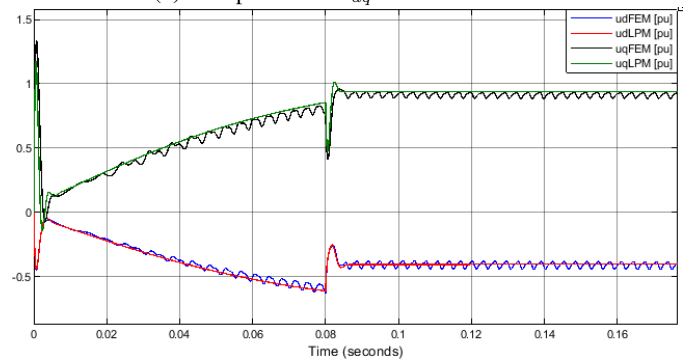
Fig. 28: MTPA 1.6 pu and 1.0 pu - Mechanical with  $L_{d2}$ .



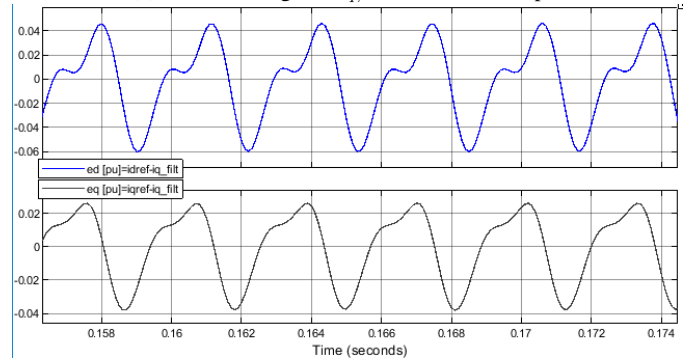
(a) Phase B current and  $\|i_s\|$  comparison of LPM and FEM.



(b) Comparison of  $i_{dq}$  in the transition.

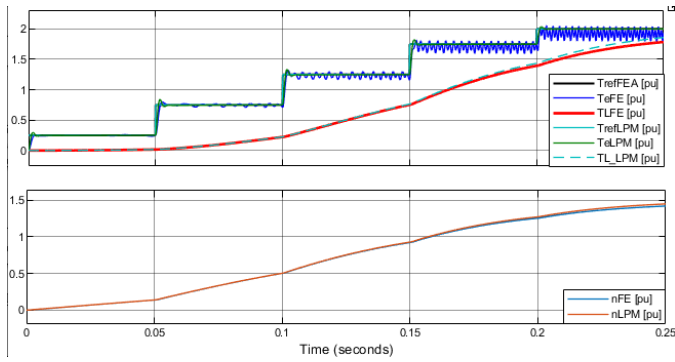


(c) Offset voltage  $\Delta u_{q,F-S} = -0.0581$  pu.

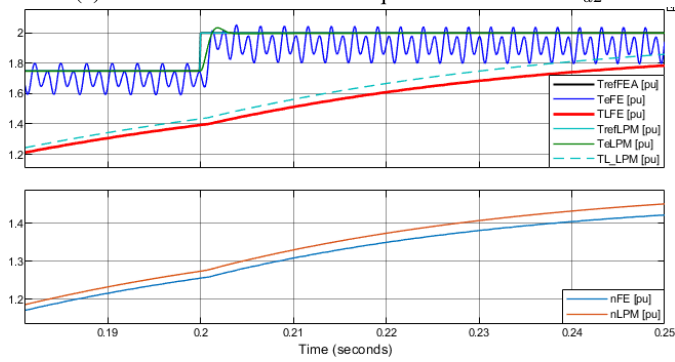


(d) Error in the feedback during steady-state.

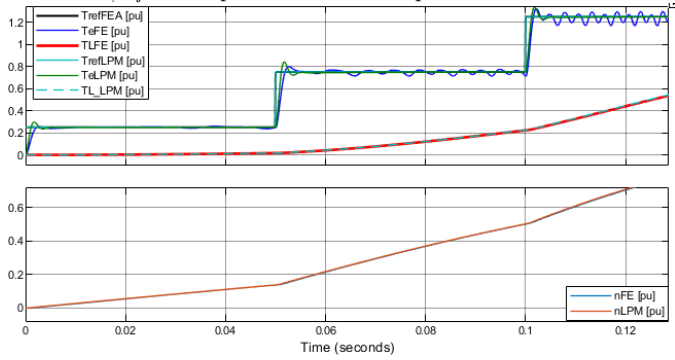
Fig. 29: MTPA 1.6 pu and 1.0 pu - Electrical with  $L_{d2}$ .



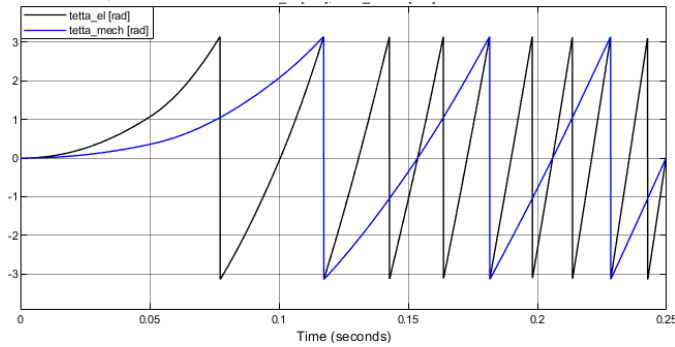
(a) Whole mechanical stair torque reference with  $L_{d2}$ .



(b)  $\tau_{e,ref} = 2.0$  pu,  $\tau_{eFEM} = 1.85$  pu and  $\tau_{eLPM} = 2.0$ .

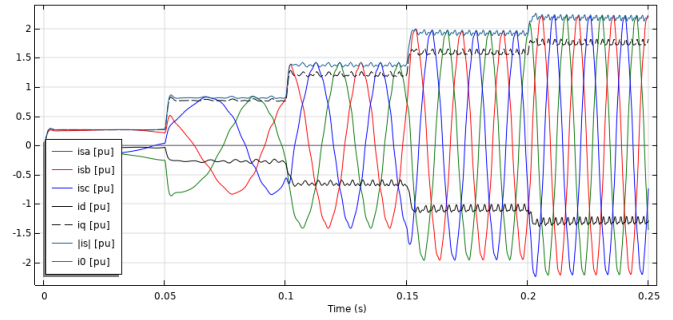


(c)  $\tau_{e,ref} = 0.25$  pu,  $\tau_{eFEM} = 0.25$  pu and  $\tau_{eLPM} = 0.25$  pu.

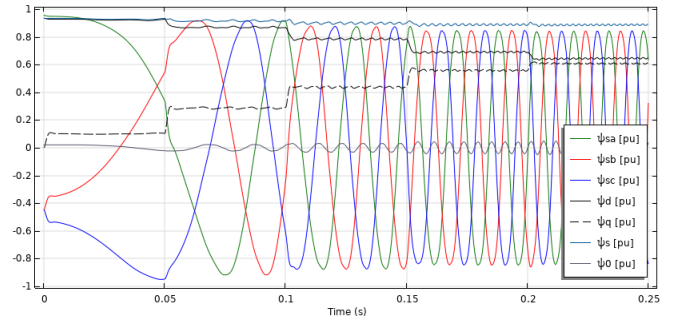


(d) Rotor is rotated below 2.5 rounds in the co-simulation.

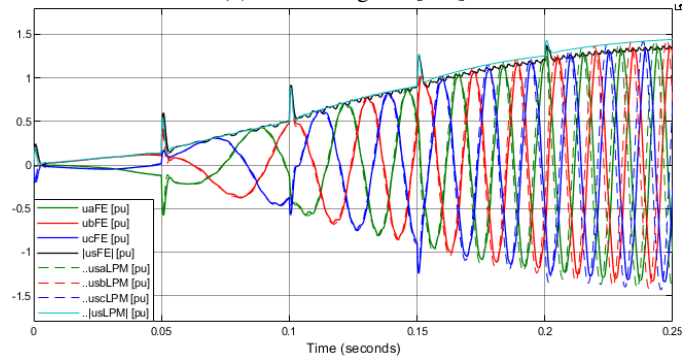
Fig. 30: MTPA Stair Load with  $L_{d2}$ .



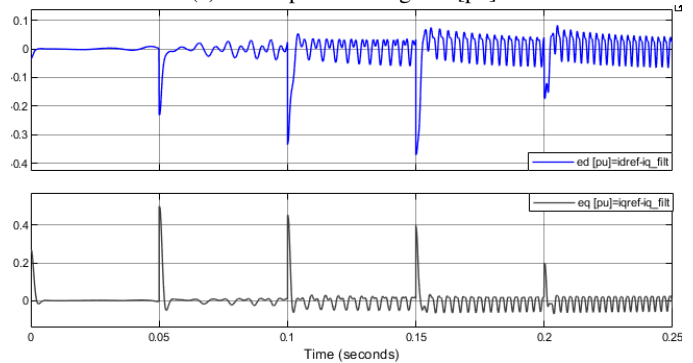
(a) Three phase current in [A].



(b) Flux linkage in [Wb].

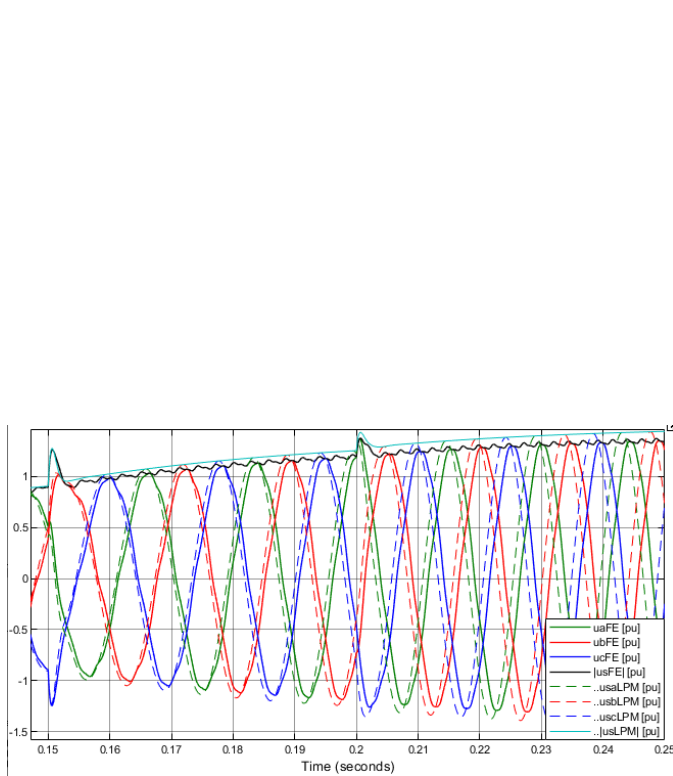


(c) Three phase voltage in [pu].

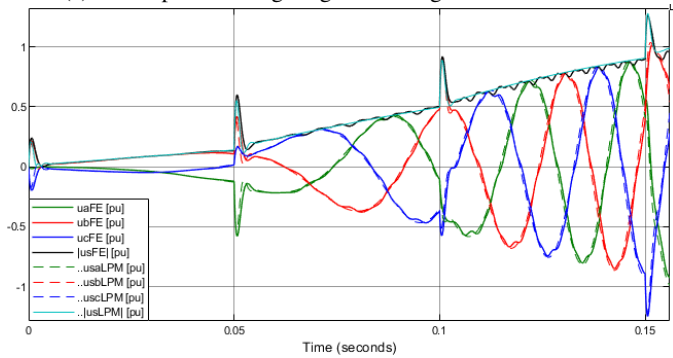


(d) Error in the whole period.

Fig. 31: MTPA Stair Load with  $L_{d2}$ .

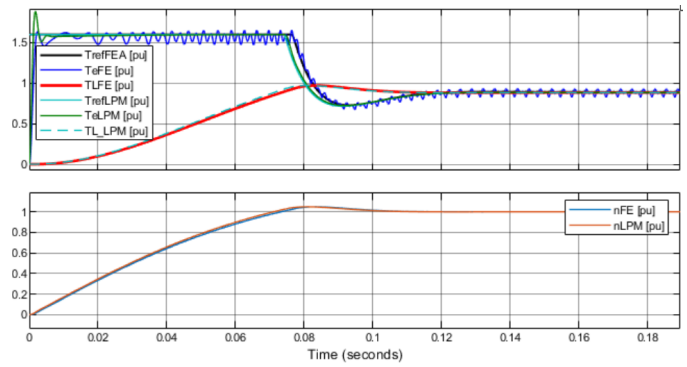


(a) Three-phase voltage lag and voltage underestimation.

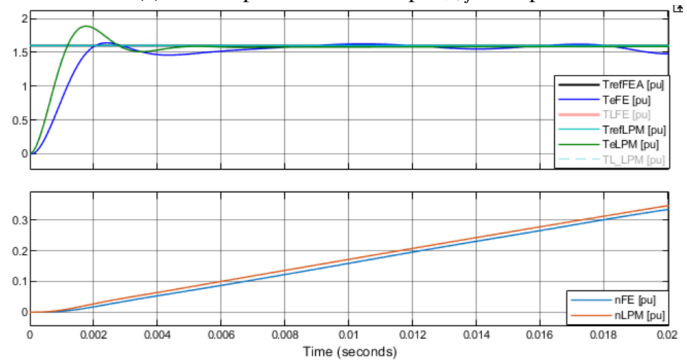


(b) Low error between LPM and FEM at the inception.

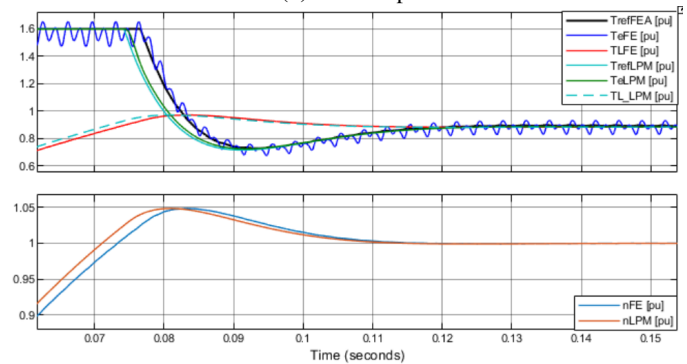
Fig. 32: MTPA Stair Load with  $L_{d2}$ .



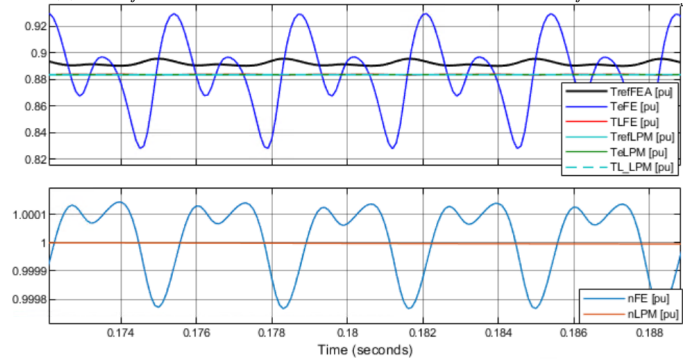
(a) Whole period with a step  $n_{ref} = 1$  pu.



(b) Start step.



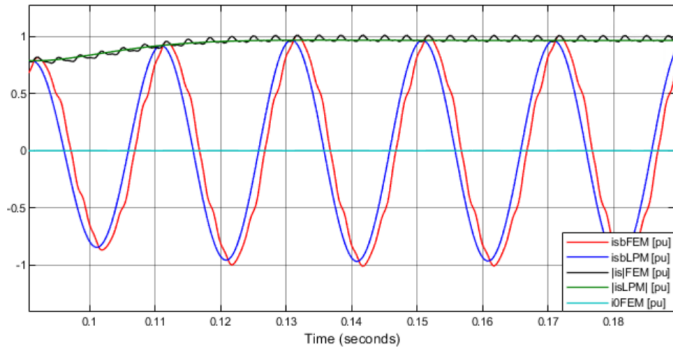
(c)  $T_{refLPM}$  decreases  $\Delta t = 2.395$  ms before  $T_{refFEM}$ .



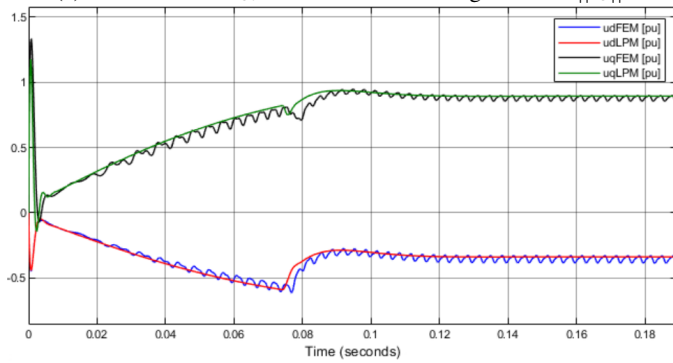
(d) Mean equilibrium:  $\tau_{refFE} = 0.8913$ ,  $\tau_{eFE} = 0.8836$ ,  $\tau_{L,FE} = 0.8835$ ,  $\tau_{FE}^*/\tau_{eFE} = 1.009$

Fig. 33: Speed Control with  $L_{d2}$ .

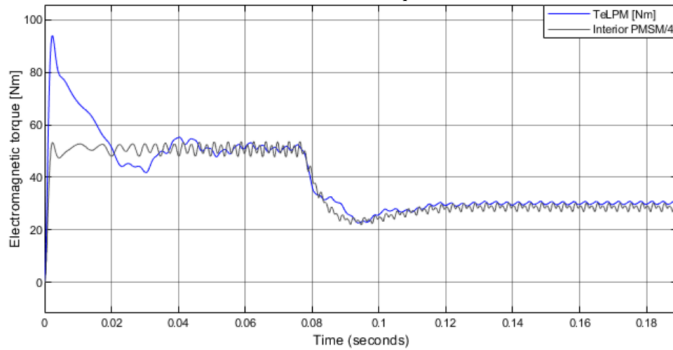




(a) Phase shift in  $i_{sb}$  and an increased magnitude in  $\|i_s\|$ .

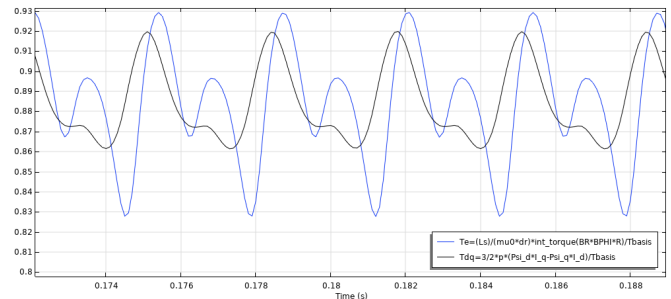


(b) Difference between  $u_d$  and  $u_q$  for FEM and LPM.

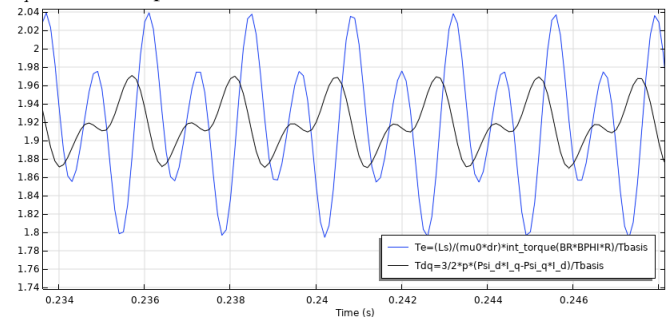


(c) LPM with equal feed-back voltage and speed.

Fig. 34: Speed Control with  $L_{d2}$ .

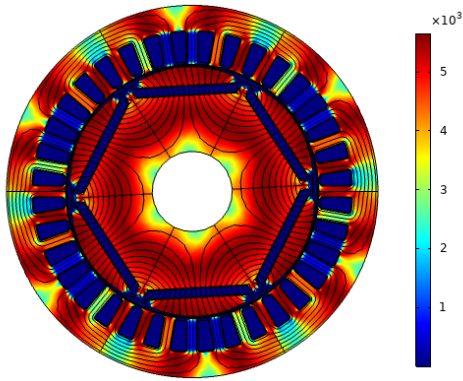


(a) Steady state results average  $\tau_{eFEM} = 0.8833$  pu and average  $\tau_{dq} = 0.88438$  pu.

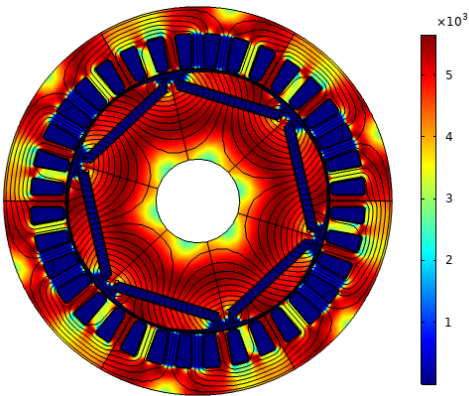


(b) From the "Stair load" case with  $\tau_{eref} = 2.0$  pu in Figure 41b.

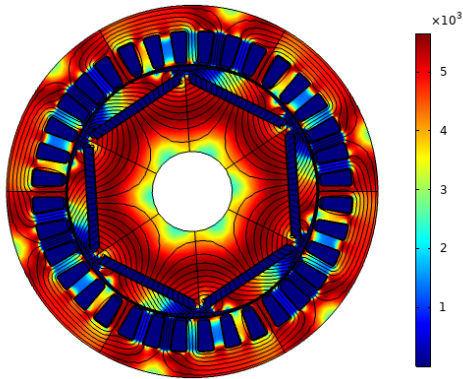
Fig. 35: Arkkios torque and co-energy torque. Obtained from Comsol Desktop with  $L_{d2}$ .



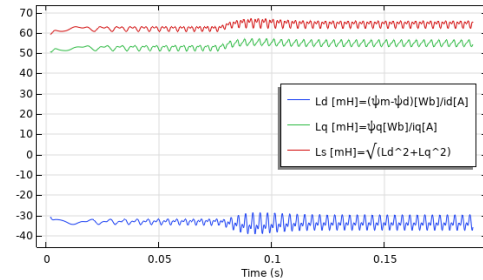
(a)  $\mu_r = rmm.normB / (\mu_0.const * rmm.normH)$  at  $\tau_{eref} = 0.25$  pu.



(b)  $\mu_r$  at  $\tau_{eref} = 0.8835$  pu.



(c)  $\mu_r$  at  $\tau_{eref} = 2.0$  pu. Saturated in the q-axis.



(d) Inductance from the speed control case  $L_{d2}$  etc.

Fig. 36: Saturation and inductance from  $L_{d2}$  simulation.

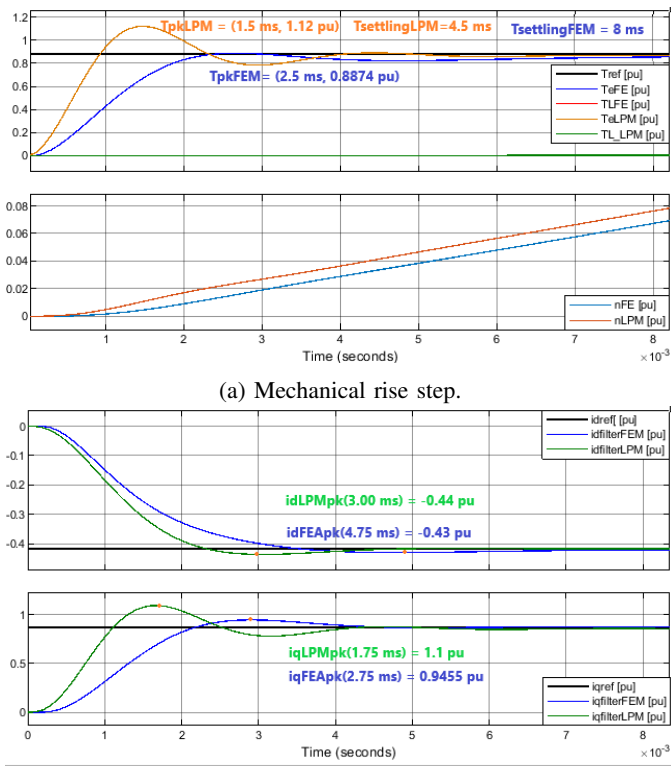


Fig. 37: Start with Step Reference  $\tau_{eref} = T_n/T_{basis}$  with  $L_{d1}$ .

Table IX is showing data from this simulation. It is listed what figures correspond to the results in Table IX. In the column to the right it is denoted **Time**. This is the time the value is measured or read from the figures referred to in the table. In the row called "**Derivative of the speed in (...)**" the  $\Delta$ -value is between time  $t = 0.207 \text{ s}$  to  $t = 0.208 \text{ s}$  indicated in the rightmost column. Values that are measured with measurement tools is denoted  $\nabla$ . Some values was estimated by using the zoom function of the Simulink scope reading from the graph, denoted with  $\diamond$ . When no indicator is used, the values are the calculated difference with a calculator. It is used abbreviations listed in the table text. Figure 39d shows the derivative of the load torque and the speed with values listed in Table IX. The derivative is measured from the lowest point at  $t_1 \approx 0.207 \text{ s}$  to the nearest peak at  $t_2 \approx 0.208 \text{ s}$ . Other places in the waves could be more correct to evaluate this. It is also clear that the speed is not exactly at equilibrium. These can be causes of the high derivative values in Table IX.

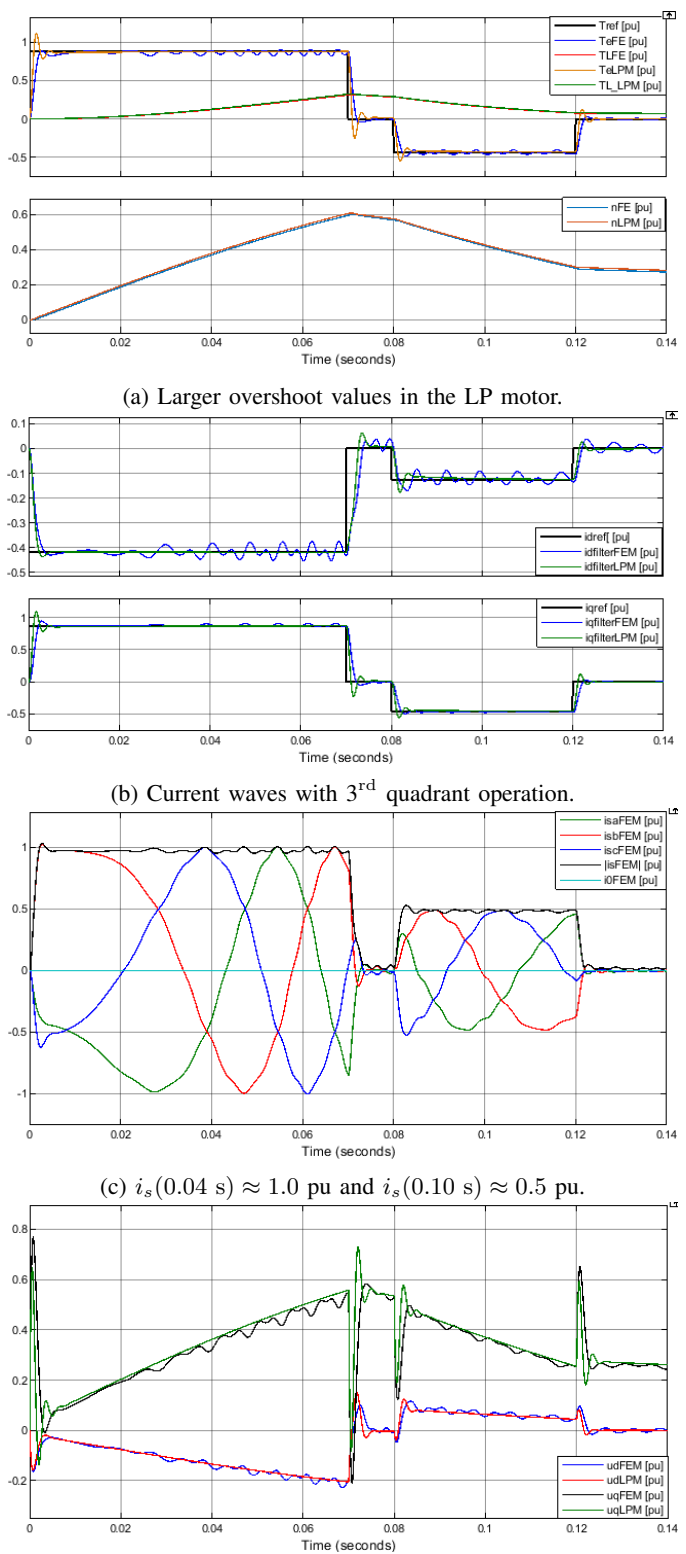
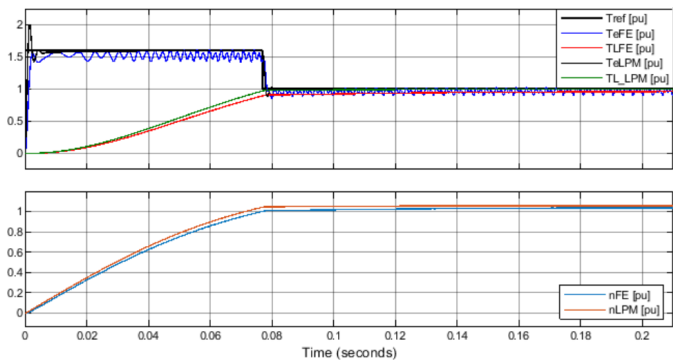
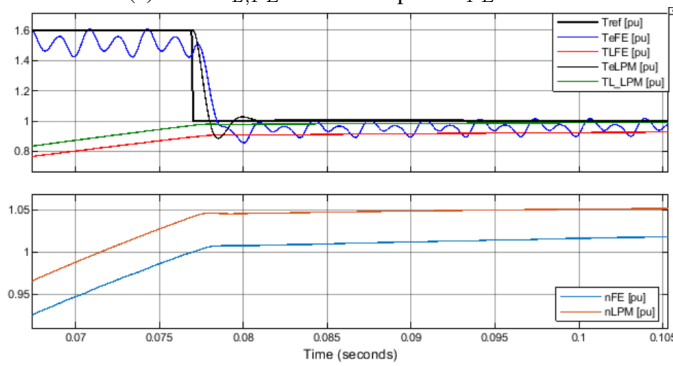


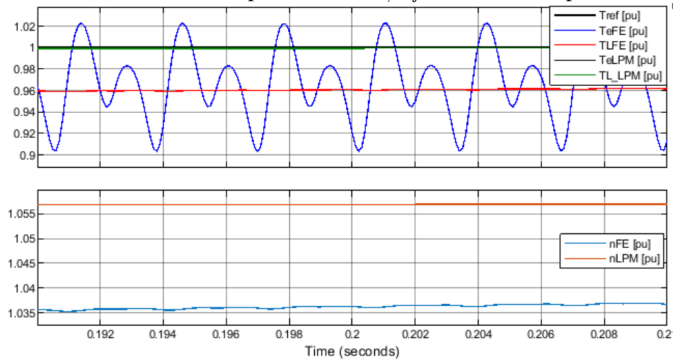
Fig. 38: Rated Step and Negative Torque with  $L_{d1}$



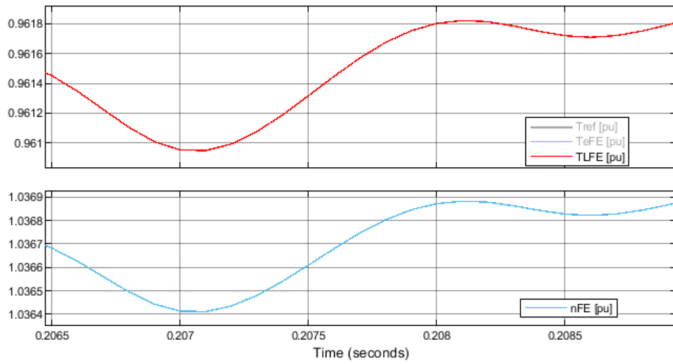
(a) Load  $\tau_{L,FE}$  error and speed  $n_{FE}$  error.



(b) Transitional phase from  $\tau_{e,ref} = 1.6 \rightarrow 1.0$  pu.

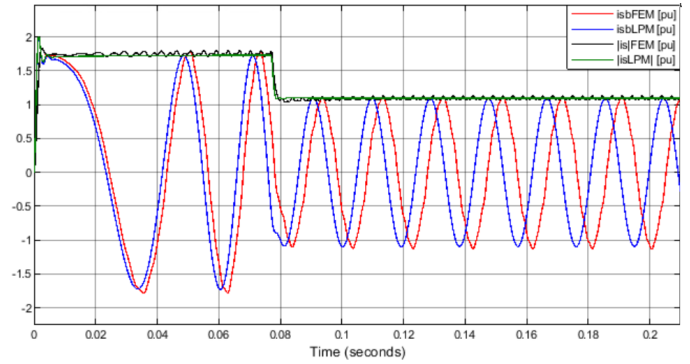


(c) Approaching steady state pu torque.

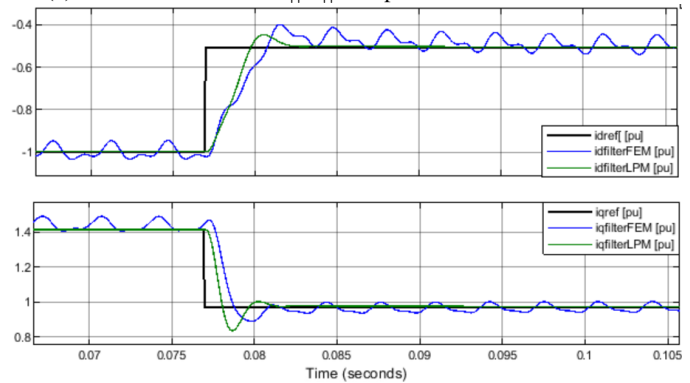


(d) Derivative of the speed approaching steady state.

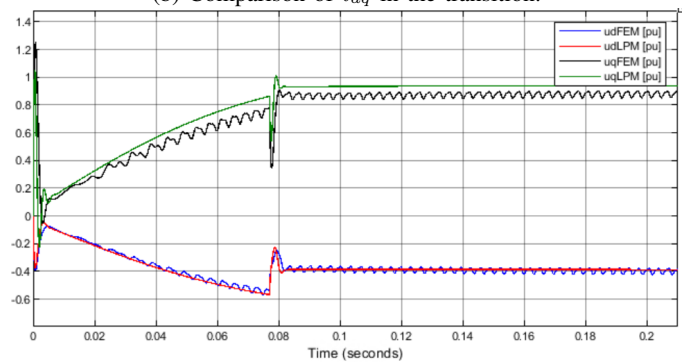
Fig. 39: MTPA 1.6 pu and 1.0 pu - Mechanical with  $L_{d1}$ .



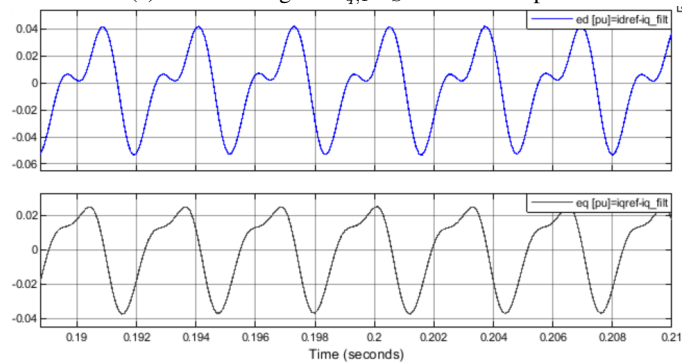
(a) Phase B current and  $\|i_s\|$  comparison of LPM and FEM.



(b) Comparison of  $i_{dq}$  in the transition.



(c) Offset voltage  $\Delta u_{q,F-S} = -0.0581$  pu.

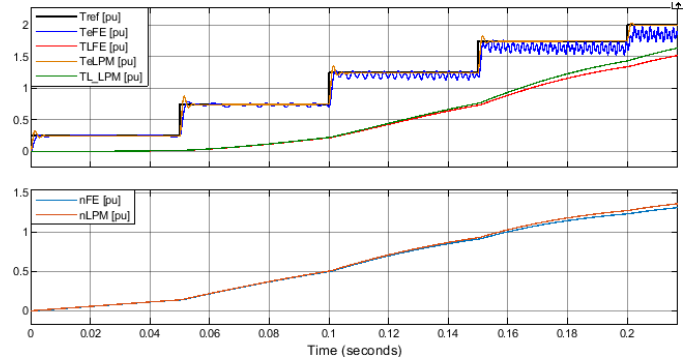


(d) Error in the feedback during steady-state.

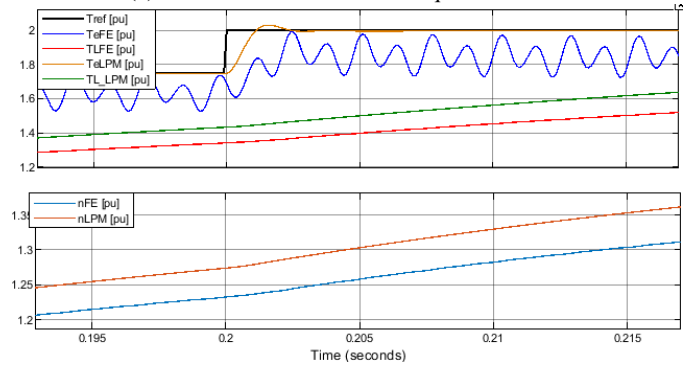
Fig. 40: MTPA 1.6 pu and 1.0 pu - Electrical with  $L_{d1}$ .

TABLE IX: MTPA control  $\tau_{ref} = 1.6 \rightarrow 1.0$ . Data points are retrieved from the measurement function in Simulink Scope. F = FEM and S = LPM. F-S = difference between LPM and FEM results. OS = overshoot value obtained from Simulink scope.

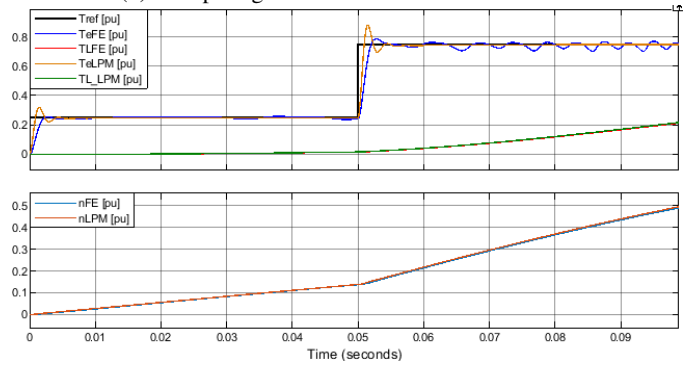
Description	Symbol	Value	Unit	Time
<b>From the beginning in Figure 39a</b>				
Reference	$T_{ref}$	1.600	pu	0.000 s
▽Peak start	$T_{eF}$	1.576	pu	0.011 s
▽OS star	$T_{eF}$	-0.995	%	0.011 s
▽Peak start	$T_{eS}$	1.998	pu	0.002 s
▽OS start	$T_{eS}$	25.900	%	0.002 s
<b>Torque steady state in Figure 39c</b>				
◇Load torque	$T_{L,F}$	0.9618	pu	0.209 s
◇Load torque	$T_{L,S}$	1.0000	pu	0.209 s
Load diff.	$\Delta T_{F-S}$	-0.0382	pu	0.209 s
◇Speed	$n_F$	1.0370	pu	0.209 s
◇Speed	$n_S$	1.0570	pu	0.209 s
Speed diff.	$\Delta n_{F-S}$	-0.0200	pu	0.209 s
<b>Derivative of the speed in Figure 39d</b>				
▽Speed diff.	$\Delta n_F$	$4.705 \cdot 10^{-4}$	pu	0.207 s
▽Time diff.	$\Delta t_F$	$1.048 \cdot 10^{-3}$	s	-0.208 s
Speed der.	$\Delta n_F / \Delta t_F$	0.4489	pu/s	
▽Load diff.	$\Delta T_{L,F}$	$8.709 \cdot 10^{-4}$	pu	0.207 s
▽Time diff.	$\Delta t_F$	$1.080 \cdot 10^{-3}$	s	-0.208 s
Load der.	$\Delta T_L / \Delta t_F$	0.807	pu/s	
<b>Peak phase current in the last el. period of Figure 40a</b>				
▽Peak	$ \hat{i}_{sbF} $	1.129	pu	0.1910 s
▽Peak	$ \hat{i}_{sbS} $	1.094	pu	0.1855 s
Difference	$\Delta \hat{i}_{sb,F-S}$	0.035	pu	
▽Phase lag	$\Delta t_{F-S}$	-5.485	ms	0.1910 s
<b>Current dq in Figure 40b</b>				
▽Peak	$ i_{dfF} $	-0.4004	pu	0.0820 s
▽Peak	$ i_{dfS} $	-0.4484	pu	0.0810 s
▽Peak	$ i_{qfF} $	0.8905	pu	0.0798 s
▽Peak	$ i_{qfS} $	0.8507	pu	0.0786 s
<b>Voltage dq in Figure 40c</b>				
◇Average	$u_{qF}$	$\approx 0.88$	pu	0.209 s
◇Average	$u_{qS}$	0.9381	pu	0.209 s
Difference	$\Delta u_{q,F-S}$	-0.0581	pu	0.209 s
<b>Error in Figure 40d</b>				
▽Difference	$\Delta e_d$	0.09	pu	0.209 s
▽Difference	$\Delta e_q$	0.07	pu	0.209 s



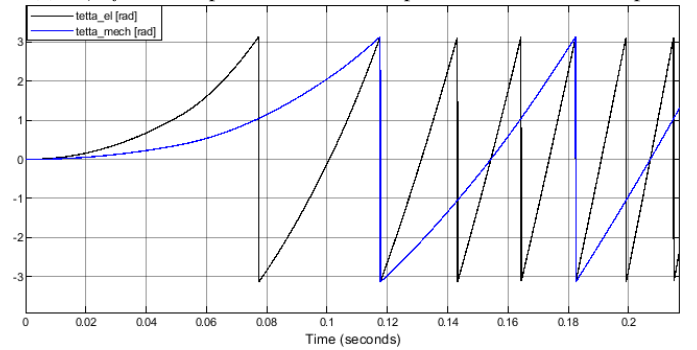
(a) Whole mechanical stair torque reference.



(b) Comparing unsaturated and saturated load.

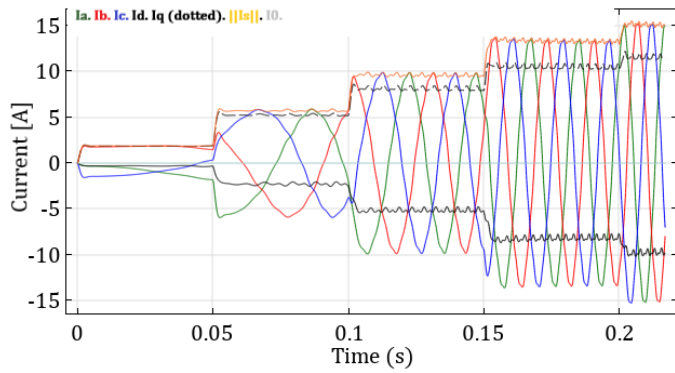


(c)  $\tau_{e,ref} = 0.25$  pu,  $\tau_{eFEM} = 0.25$  pu and  $\tau_{eLPM} = 0.25$  pu.

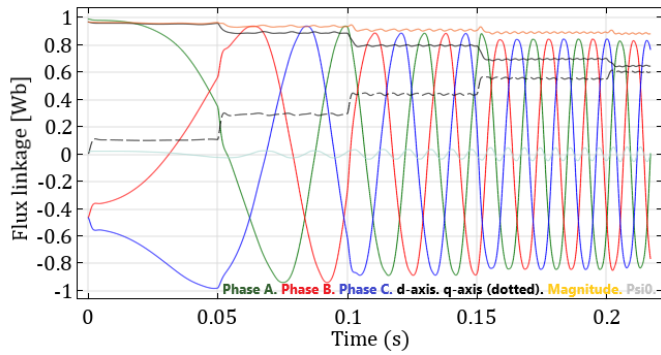


(d) Rotor is rotated below 2.5 rounds in the co-simulation.

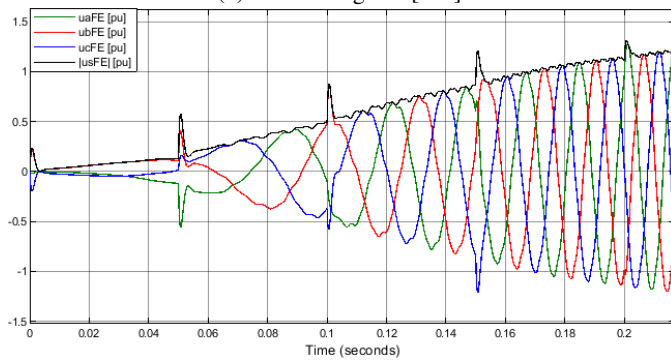
Fig. 41: MTPA Stair Load with  $L_{d1}$ .



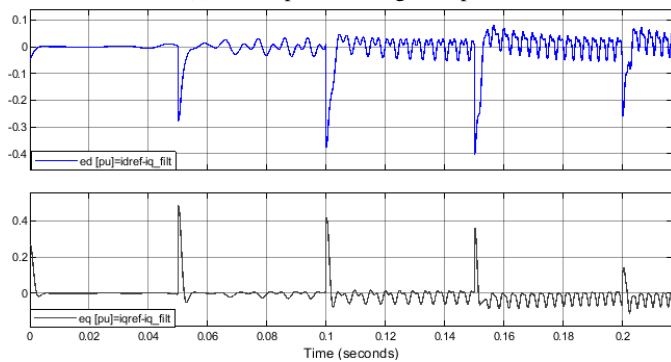
(a) Three phase current in [A].



(b) Flux linkage in [Wb].

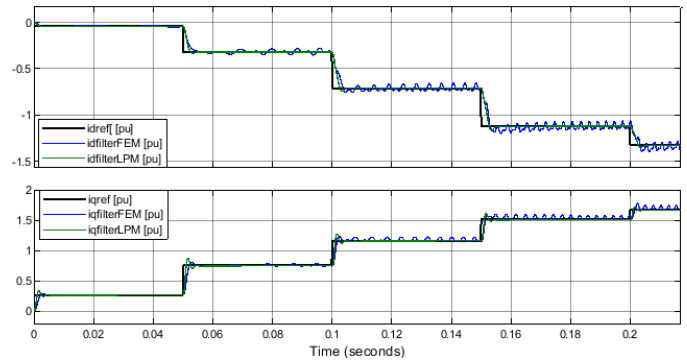


(c) Three phase voltage in [pu].

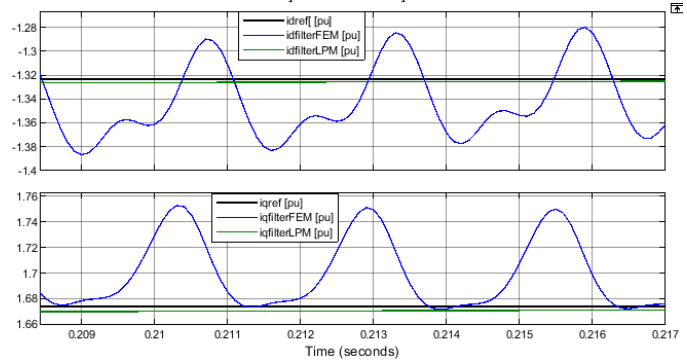


(d) Error in the whole period.

Fig. 42: MTPA Stair Load with  $L_{d1}$ .

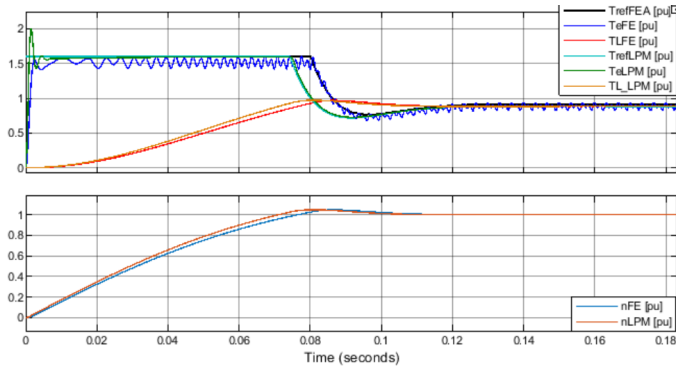


(a)  $i_{dqFEM} \approx i_{dqLPM}$ .

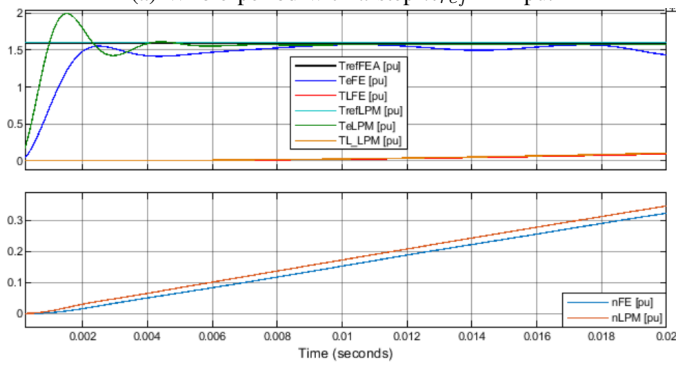


(b) Steady state error in the current components  $i_{dq}$ .

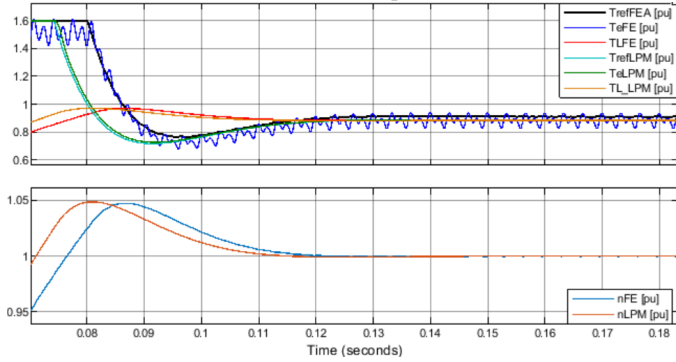
Fig. 43: MTPA Stair Load with  $L_{d1}$ .



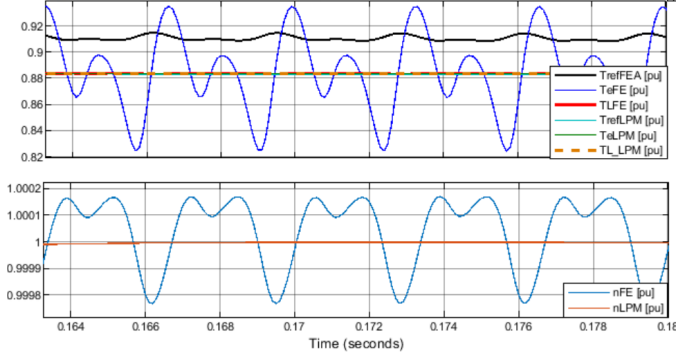
(a) Whole period with a step  $n_{ref} = 1$  pu.



(b) Start step.

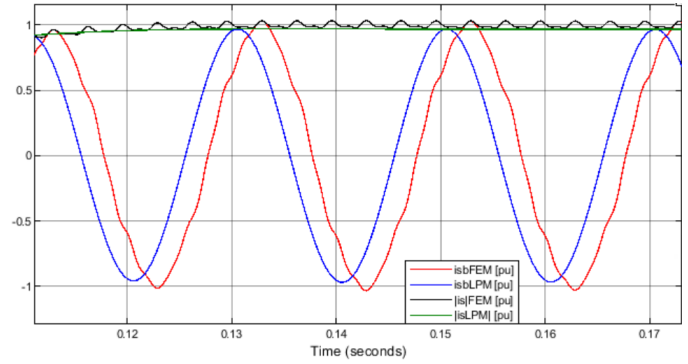


(c) LPM reaching the transitional phase 3-5 ms before FEA.

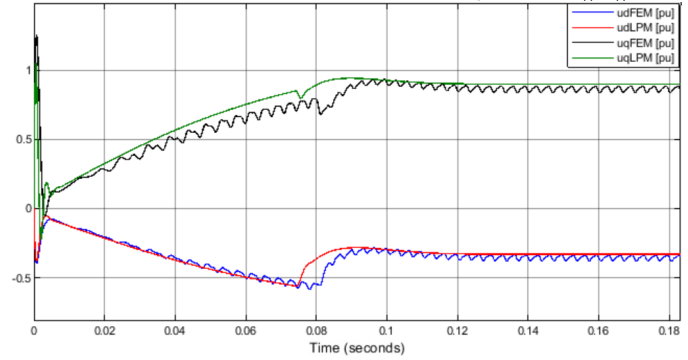


(d) Steady-state mechanical performance of the motor.

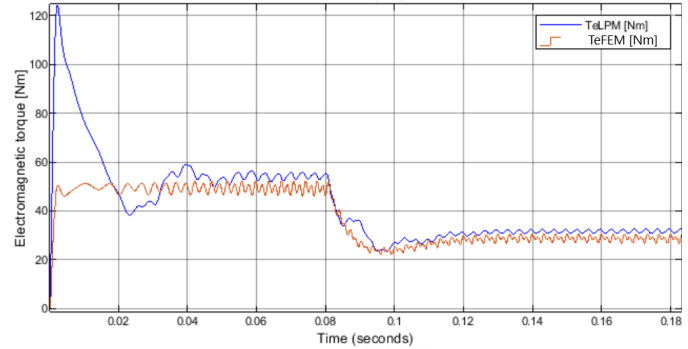
Fig. 44: Speed Control with  $L_{d1}$ .



(a) Phase shift in  $i_{sb}$  and an increased magnitude in  $\|i_s\|$ .

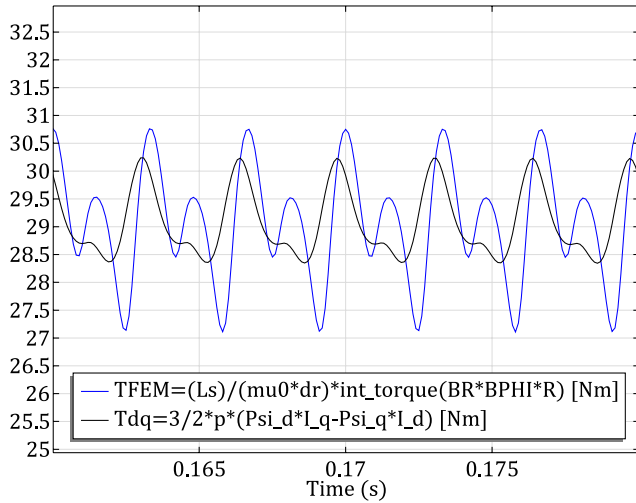


(b) Difference between  $u_d$  and  $u_q$  for FEM and LPM.

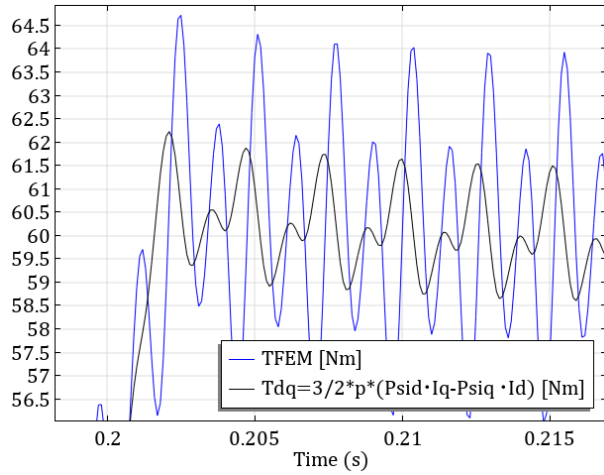


(c) LPM with equal feed-back voltage and speed.

Fig. 45: Speed Control with  $L_{d1}$ .

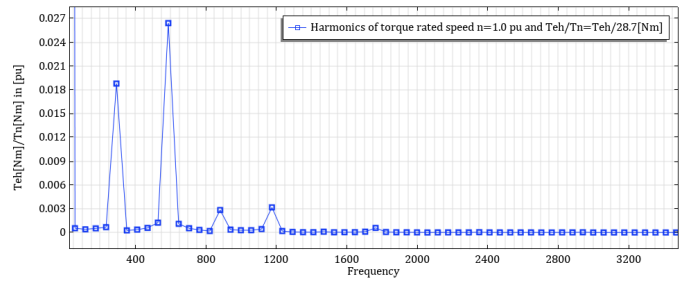


(a) Steady state results in time  $t = 0.16 - 0.18$  s from the "speed regulator" case depicted in Figure 44a.

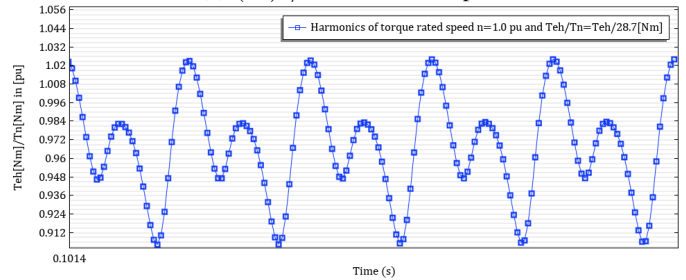


(b) From the "Stair load" case with  $\tau_{ref} = 2.0$  pu in Figure 41b.

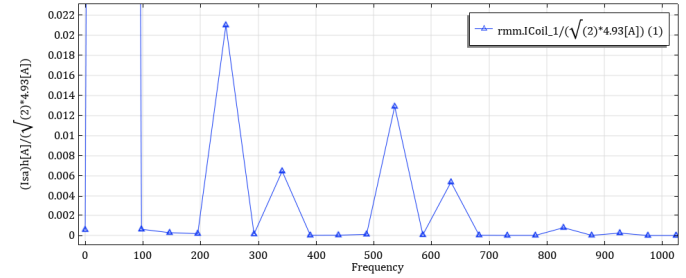
Fig. 46: Arkkios torque and co-energy torque. Obtained from Comsol Desktop with  $L_{d1}$ .



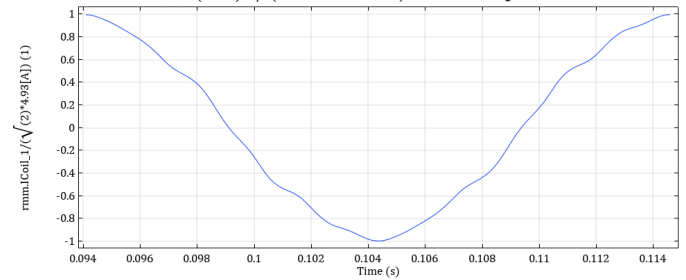
(a)  $(T_e)_1 / T_{rated} = 0.972$  pu.



(b) The torque curves it is performed Fourier transformation in Figure 47a



(c)  $(I_{sa})_1 / (\sqrt{2} \cdot 4.93 \text{ A}) = 0.681$  pu.



(d) The electrical period it is performed a Fourier transformation in Figure 47c. The electrical period  $T_1 = 20$  ms.

Fig. 47: Rated torque and rated speed in pu, steady state. Harmonic analysis with  $L_{d1}$ .

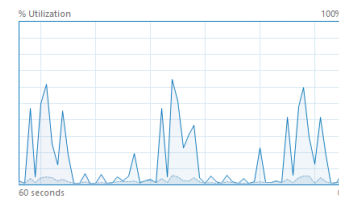
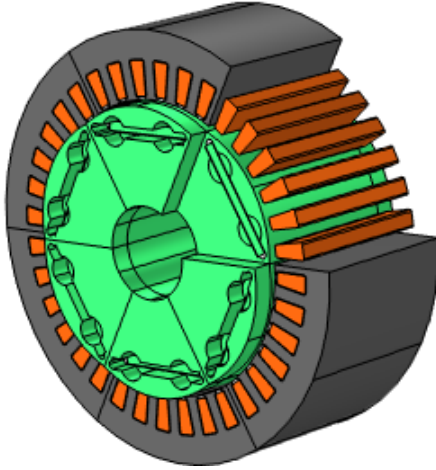


Fig. 48: How a computer use CPU in a co-simulation at the start, and the performance diminishes with time. Performed on external server connected to Professor Nilssens PC (best performing). With parameter  $L_{d2}$ .

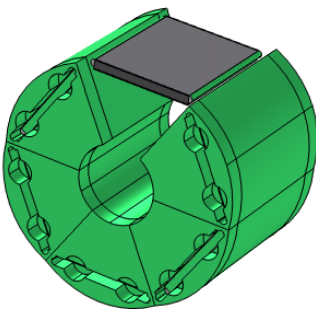


APPENDIX B  
IPMSM DATA AND GEOMETRY

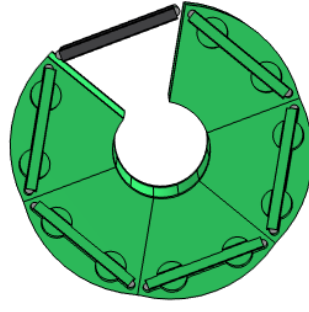
The following equations in Table X have been used regarding machine design with notation mainly from [36]. It is observed that the rotor have an ellipsis shape. The y-axis ellipsis radius is estimated to be  $b = \sqrt{((D_{roq}/2)^2 - (D_{rod}/2)^2 * (\cos(68.8[deg]))^2)}$  where it is estimated an angle of 68.8[deg], the x-axis radius of the ellipsis is  $a = D_{rod}/2$ , the pole pitch for the d and q axis  $\tau_{pd} = \pi D_{rod}/(2p)$  and  $\tau_{pq} = \pi D_{roq}/(2p)$  (respectively), conductor area  $A_c = \pi r_c^2$ , outer d-axis diameter  $D_{rod} = D_{ri} + 2h_{ryd}$ , outer q-axis rotor diameter  $D_{roq} = D_{ri} + 2h_{ryq}$ , outer air gap diameter  $D_g = D_{rod} + 2g_d$ , air gap in the d-axis  $g_d = (D_{si} - D_{rod})/2$ , air gap in the q-axis  $g_q = (D_{si} - D_{roq})/2$ , number of turns  $N_c = A_u k_{fill}/A_c$ , slot angle  $\alpha_u = (2\pi)/Q_s$ , machine aspect ratio  $\chi \approx L_s/(D_{rod})$ . It was also made a 3D model of the motor, not completed for 3D simulations in Figure 49a to Figure 49c.



(a) 3D view of the motor with stator.



(b) 3D view of the rotor with an open rotor and one hidden pole shoe.



(c) 3D view of the rotor with an open rotor and one hidden pole shoe.

TABLE X: Geometry used in COMSOL, measured and estimated values.  $\diamond$  is used as machine length in rmm.

Description	Name	Value	Unit
Pole angle	$\alpha_p$	60	$^\circ$
Slot angle	$\alpha_u$	10	$^\circ$
Approximate machine aspect ratio	$\chi$	0.548	pu
Small triangle in slot wedge length	$\Delta_{sw}$	1.25	mm
Pole-pitch largest rotor radius	$\tau_{pd}$	77.23	mm
Pole-pitch smallest rotor radius	$\tau_{pq}$	75.136	mm
Area of Cu in COMSOL	$A_{Cu}$	137.73	mm <sup>2</sup>
Measured conductor area	$A_c$	0.442	mm <sup>2</sup>
Area of slot (Domain 16+18)	$A_u$	168.08	mm <sup>2</sup>
Ellipsis rotor a-radius (d)	$a$	73.75	mm
Slot opening	$b_{so}$	3	mm
Tooth width	$b_{st}$	6.2	mm
Upper slot width	$b_{su1}$	9	mm
Lower slot width	$b_{su2}$	13	mm
Slot wedge width	$b_{sw}$	10.1	mm
Ellipsis rotor b-radius (q)	$b$	66.61	mm
Inner rotor diameter	$D_{ri}$	47.5	mm
Longest outer rotor diameter	$D_{rod}$	147.5	mm
Shortest outer rotor diameter	$D_{roq}$	143.5	mm
Inner stator diameter	$D_{si}$	150	mm
Outer stator diameter	$D_{so}$	220	mm
Stator yoke thickness	$D_{sy}$	190	mm
Measured conductor diameter	$d_c$	0.75	mm
Outer air gap diameter	$D_g$	150	mm
d-axis air gap	$g_d$	1.25	mm
q-axis air gap	$g_q$	3.25	mm
Slot height PM with sleeves	$h_{PM}$	6	mm
Height of PM	$h_{PM}$	5	mm
q-axis rotor yoke thickness	$h_{ryd}$	50	mm
d-axis rotor yoke thickness	$h_{ryq}$	48	mm
Tooth height	$h_{st}$	20	mm
Slot height	$h_{su}$	20	mm
Height of slot wedge	$h_{sw}$	1.5	mm
Copper fill factor	$k_{fill}$	0.5	pu
z-length of rotor	$L_r$	102	mm
z-length of stator	$L_s^\diamond$	80.8	mm
Number of phases	$m$	3	
Guessed amount of stator turn	$N_{coil}$	50	turns
Poles	$2p$	6	poles
Stator slots	$Q_s$	36	slots
Measured conductor radius at the lab	$r_c$	0.375	mm
Initialisation of time	$t$	0	s
Width of PMs	$w_{PM}$	60	mm
Distribution factor of the fundamental	$k_{d1}$	0.99619	pu
Pole-pitch factor of the fundamental	$k_{p1}$	1.00	pu
Winding factor of the fundamental	$k_{w1}$	0.99619	pu

Fig. 49: 3D view, not completed for simulation.

APPENDIX C  
CORRECT CIRCUIT

This project was carried out in different phases. The first part was to reverse engineer the motor at the lab, the second part was to design a control system and find a methodology to connect a FEA model to that controller.

The machine should have a correct line voltage constant  $K_e = 371$  V/krpm and corresponding phase voltage constant  $e_m = 214.2$  V/krpm. The flux linkage should be  $\Psi_{PM} = K_e / (2\pi f_n) = 0.9642$  Wb. This was done with some small deviation, also the end winding effects and end winding inductance's are also omitted.

Several test was made to ensure that the machine parameters was correct according to the expected performance. The graphs in this section verifies that the machine model perform as expected.

A. Attempt Without External Circuit

In Figure 50 the voltage vector of the applied three-phase voltage  $V_n = 230$  V<sub>RMS</sub> is applied in such a way that the pole wheel angle  $\angle\delta$  is aligned with the back EMF vector. The back EMF vector is aligned with the q-axis by the formula  $E_m(j\omega_{el}) = j\omega_{el}\Psi_m$ . This test was performed to ensure that it was possible to apply a voltage on the voltage driven coils. The back EMF was obtain during a rated speed, no load test with open-circuit, i.e. the coils were modelled as current sources with  $I_{coil} = 0$  A. It is observed in Figure 50 that phase A is lagging  $\vartheta_{el} \approx 90$  degrees with the d-axis. How the phase sequence was defined during this exact test is unknown. However the electrical voltage angle was defined in the expression  $\hat{V}_{coil} \cdot \sin(2 \cdot \pi \cdot f_n \cdot -92.2^\circ)$ . The time instances from the two simulation (no load test and applied rated voltage) are the extracted raw data from Comsol.

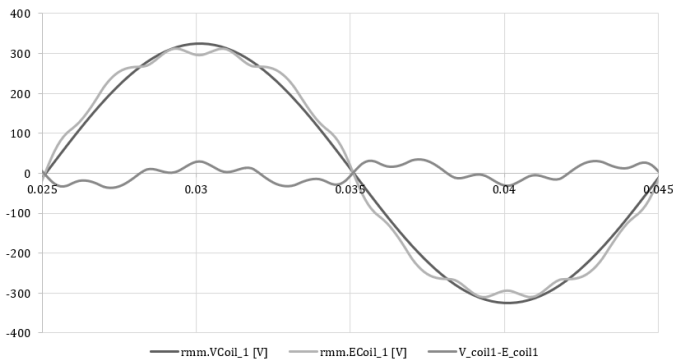


Fig. 50: The induced back EMF, the applied voltage and the voltage difference between the back EMF and applied voltage at rated speed.

The result of not modelling a neutral connection in the IPMSM circuit is shown in Figure 51. The current waveforms are from the same tests shown in Figure 52, with the same voltage angle  $-92.2^\circ$  and rotor position. It is a transient period not included here, before the currents reaches steady state. When the steady state is reached, it is observed that the currents are in phase, and the reluctance torque is thus

pulsating. It is of course only the reluctance torque component that is present, because  $\delta$  is small (but not equal to zero).

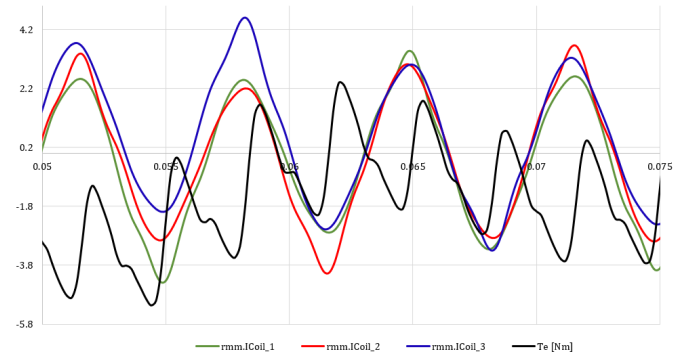


Fig. 51: Applied three-phase-voltage, reaching steady state and in phase

Figure 52 shows

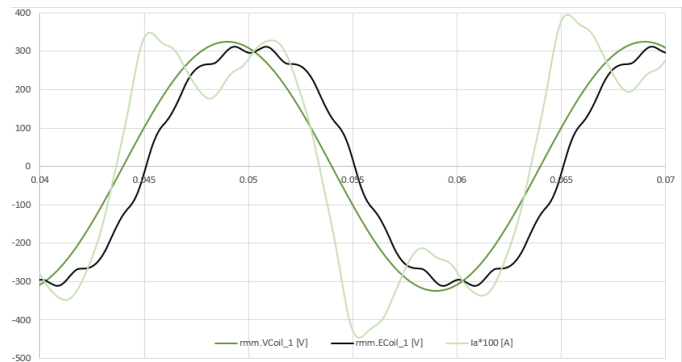
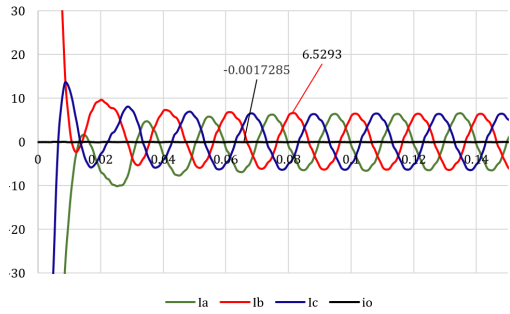


Fig. 52: Considerable amount of space harmonics.

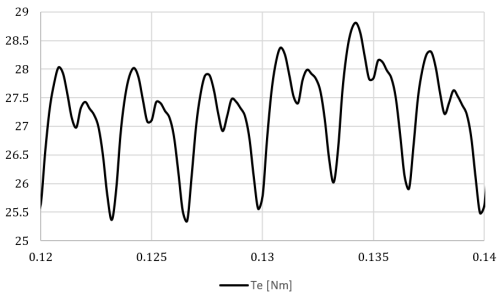
B. Attempt with Isolated Neutral

The tests that are done here are not exactly according to the rated performance with the applied voltage of  $V_n = 230$  V<sub>rms</sub> and  $N_n = 1000$  RPM. This can be looked upon as connecting a machine with in nominal speed  $N_n$  directly to an infinite bus. The circuit that is used for these tests is depicted in Figure 13. The DC sources are switched with **Voltage source: Sine wave**. The phase sequence with respect to the d-axis  $\Psi_m$  is defined according to Figure 8.

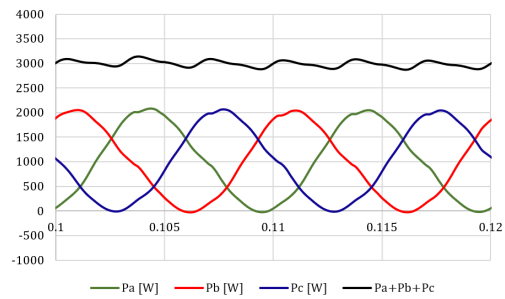
For the test in Figure 53a-Figure 53c the rotor is rotating in synchronous speed and it is applied a phase voltage of  $|V_n|\angle\delta = 230\angle + 18.2^\circ$ . The material in the rotor Electrical steel have a conductivity of  $\sigma_{rotor} = 1000$  S/m, to work as a damper winding in the rotor to reduced the duration of the transient envelope.



(a) Transient current.



(b) Nominal torque in the coils after the transient period.



(c) Nominal power in the coils after the transient period.

Fig. 53: Applied voltage at the approximate nominal working point.

## APPENDIX D MATLAB SCRIPT

```

1 %% IPMSM MTPA Speed Control
2 clear all; close all; clc;
3 %% Motor data
4 In = 4.93; %Arms
5 Un=230; %Vrms
6 N=1000; %RPM
7 Tn = 28.7; %Nm
8 Psi_m = 0.96312; %Wb
9 J=0.027; %kgm^2
10 p=3;
11 fe=N*2*p/120; %Hz
12 fn=fe; %Hz
13 we=2*pi*fe; %rad/s
14 wn=we;
15 w=we/p; %rad/s
16 kt=1.5*p;
17 Pn=Tn*w; %W
18 epm=we*Psi_m; %Vpk
19 Em=epm/sqrt(2); %Vrms
20 Rcoil= 1.892; %Ohm
21 Rend=0.005*2; %Ohm
22 Rs = Rcoil+Rend; %Ohm
23 %Lend=69.872e-6; %Ohm
24 % (Ld1,Lq1) - over-saturated
25 Ld1 = 23.4048e-3; %H
26 Xd1= 2*pi*fe*Ld1; %Ohm
27 Lq1 = 53.0932e-3; %H
28 Xq1 = 2*pi*fe*Lq1; %Ohm
29 saliency1=Lq1/Ld1;
30 % (Ld2,Lq2) - Rated MTPA
31 Ld2 = 30.8030e-3; %H
32 Xd2 = 2*pi*fe*Ld2; %Ohm
33 Lq2 = 53.6110e-3; %H
34 Xq2 = 2*pi*fe*Lq2; %Ohm
35 saliency2=Lq2/Ld2;
36 %% Base values
37 Ibasis = sqrt(2)*In; %A
38 Ubasis=sqrt(2)*Un; %V
39 Zbasis=Ubasis/Ibasis; %Ohm
40 Psi_basis =Ubasis/we; %Psi
41 Sbasis=3/2*Ubasis*Ibasis; %VA
42 Tbasis=3/2*p*Psi_basis*Ibasis; %Nm
43 wn=we;% rad/s
44 Wn=wn/3; %rad/s
45 kL=Tn/(Wn^2);
46 %% Per unit
47 % (xd1,xq2)- over-saturated
48 xd1=Xd1/Zbasis;
49 xq1=Xq1/Zbasis;
50 % (xd2,xq2) - MTPA
51 xd2=Xd2/Zbasis;
52 xq2=Xq2/Zbasis;
53 % Used for LPM IPMSM
54 xd=xd2;
55 xq=xq2;
56 % Decoupled from saturation
57 rs=Rs/Zbasis;
58 psi_m=Psi_m/Psi_basis;
59 te_n=Tn/Tbasis;
60 %% Converter
61 udc=1.0;
62 fsw=1000;
63 Tsw=1/fsw;
64 Tdelay=Tsw/3; % p. 244.
65 %% Filter
66 uctrl_ripp=0.08;
67 Tfq=200e-6;
68 Tfd=Tfq;
69 Teqi=2*(Tdelay+Tfq);
70 %% PI-CC Analog
71 % PI parameters (d1,q1)
72 Td1=xd1/(wn*rs);
73 Tq1=xq1/(wn*rs);
74 Kpd1=xd1/(2*wn*(Tdelay+Tfd));
75 Kpq1=xq1/(2*wn*(Tdelay+Tfq));
76 % PI parameters (d2,q2)
77 Td2=xd2/(wn*rs);
78 Tq2=xq2/(wn*rs);
79 Kpd2=xd2/(2*wn*(Tdelay+Tfd));
80 Kpq2=xq2/(2*wn*(Tdelay+Tfq));
81 % Used in LiveLink
82 Kpd=Kpd2;
83 Td=Td2;
84 Kpq=Kpq2;
85 Tq=Tq2;
86 % Decoupled from saturation
87 Tsum=Tdelay+Tfq;
88 Trise=4.7*Tsum;
89 Tsettling=8.4*Tsum;
90 Teqid=2*(Tdelay+Tfd);
91 Teqiq=2*(Tdelay+Tfq);
92 w0=1/(sqrt(2)*Tsum);
93 %% Speed Controller PI-CS - Analog
94 Tm = J*(Wn)^2/Sbasis;
95 beta = 4;
96 Tfn= 2e-3; %Tacho-filter
97 Tsumn=2*Tsum+Tfn;
98 Kpn=Tm/(sqrt(beta)*Tsumn);
99 Tin =beta*Tsumn;
100 wcn= 1/(sqrt(beta)*Tsumn);
101 %% Limits
102 ULi=2;
103 LLi =-ULi;
104 ULn=2;
105 LLn=-ULn;
106 te_max=1.6;
107 is_max=Inf;
108 %% MTPA Calculations
109 tn=Tn/Tbasis;
110 a=(psi_m/3)^3;
111 b=((xq2-xd2)^2*tn^2)/(3*psi_m);
112 idmtpa=(psi_m/3-(a+b)^(1/3))/(xq2-xd2);
113 psi_T=psi_m-(xq2-xd2)*idmtpa;
114 iqmtpa=tn/(psi_T);
115 %% Transfer functions
116 s= tf('s');
117 %% Margin d-axis over-saturated/ratedMTPA
118 % Over-saturated
119 toid1=Kpd1*(1+Td1*s)*(wn*Td1);
120 noid1=Td1*s*xd1*(1+Td1*s)*(1+Tsum*s);
121 hoid1=toid1/noid1;
122 % Rated MTPA
123 toid2=Kpd2*(1+Td2*s)*(wn*Td2);
124 noid2=Td2*s*xq2*(1+Td2*s)*(1+Tsum*s);
125 hoid2=toid2/noid2;
126 figure(1)
127 margin(hoid1)
128 hold on
129 margin(hoid2)
130 grid on
131 legend('sat: hoid1','rated MTPA: hoid2')
132 %% Margin q-axis over-saturated/ratedMTPA
133 % Lq1 \approx Lq2
134 % Over-saturated
135 toiq1=Kpq1*(1+Tq1*s)*(wn*Tq1);
136 noiq1=Tq1*s*xq1*(1+Tq1*s)*(1+Tsum*s);
137 hoiq1=toiq1/noiq1;
138 % Rated MTPA
139 toiq2=Kpq2*(1+Tq2*s)*(wn*Tq2);
140 noiq2=Tq2*s*xq2*(1+Tq2*s)*(1+Tsum*s);
141 hoiq2=toiq2/noiq2;
142 figure(2)
143 margin(hoid1)
144 hold on
145 margin(hoid2)
146 grid on
147 legend('sat: hoiq1','rated MTPA: hoiq2')
148 %% Nyquist d
149 figure(3)

```

```
150 nyquist(hoid1)
151 hold on
152 nyquist(hoid2)
153 legend('sat: hoid1', 'Orated MTPA: hoid2')
154 %% Nyquist q
155 figure(4)
156 nyquist(hoiq1)
157 hold on
158 nyquist(hoiq2)
159 legend('sat: hoiq1', 'Rated MTPA: hoiq2')
160 %% Speed control
161 t0n=Kpn*(1+Tin*s);
162 n0n=Tin*s*Tm*s*(1+Tsumn*s);
163 h0n=t0n/n0n;
164 %% Margin PI-CCq and PI-SC
165 figure(5)
166 margin(hoiq2)
167 hold on
168 margin(h0n)
169 legend('rated MTPA: hoiq2', 'Speed: h0n')
170 %% Nyquist PI-CCq and PI-SC
171 figure(6)
172 nyquist(hoiq2)
173 hold on
174 nyquist(h0n)
175 legend('rated MTPA: hoiq2', 'speed: h0n')
```

APPENDIX E  
SIMULINK

Figure 55 shows the Simulink model used in this thesis. Figure 56 shows the FEA IPMSM Park-Clarke transformation used in this thesis. The gain at each voltage terminal is  $U_{basis}$ , while the gain at the output is  $1/I_{basis}$  before the Park-Clarke transformation to obtain pu values.

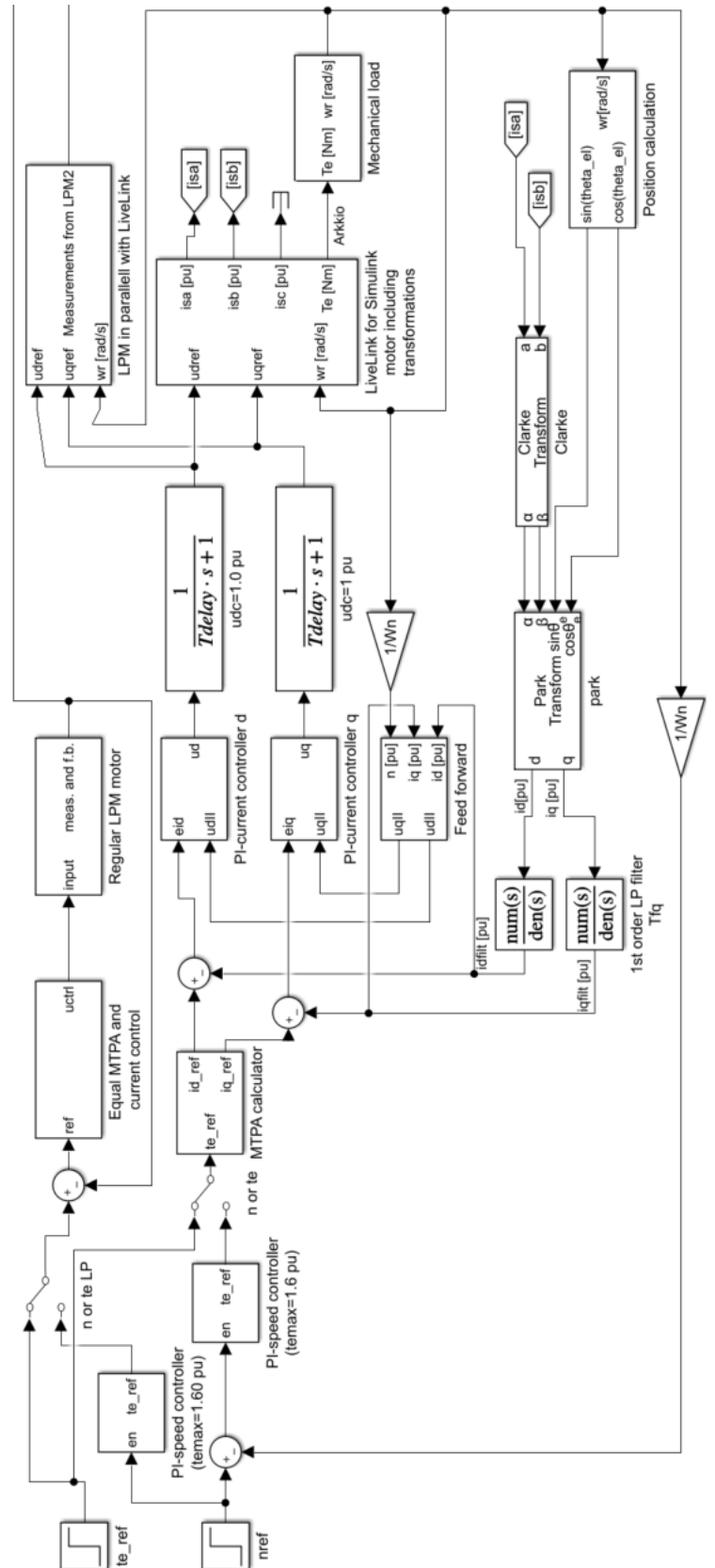


Fig. 54: Conceptual drawing of the simulation model structure. Not used.

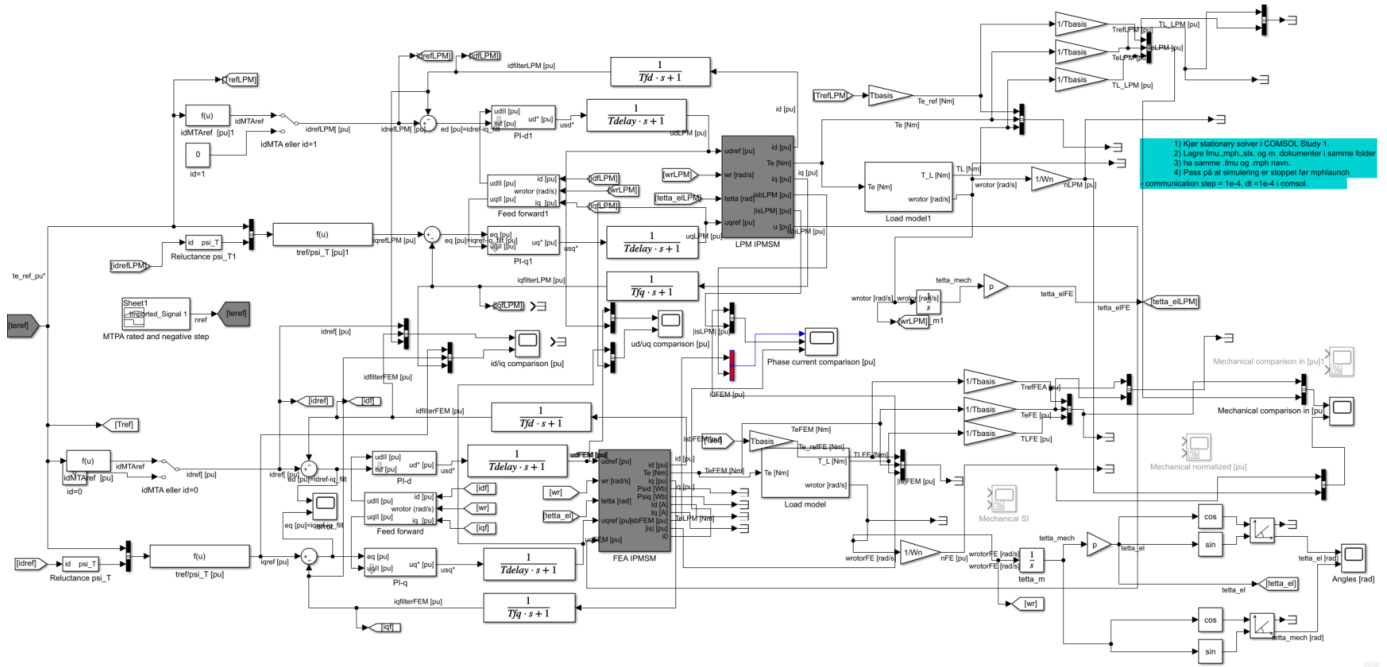


Fig. 55: This is the MTPA speed control that is used in this thesis.

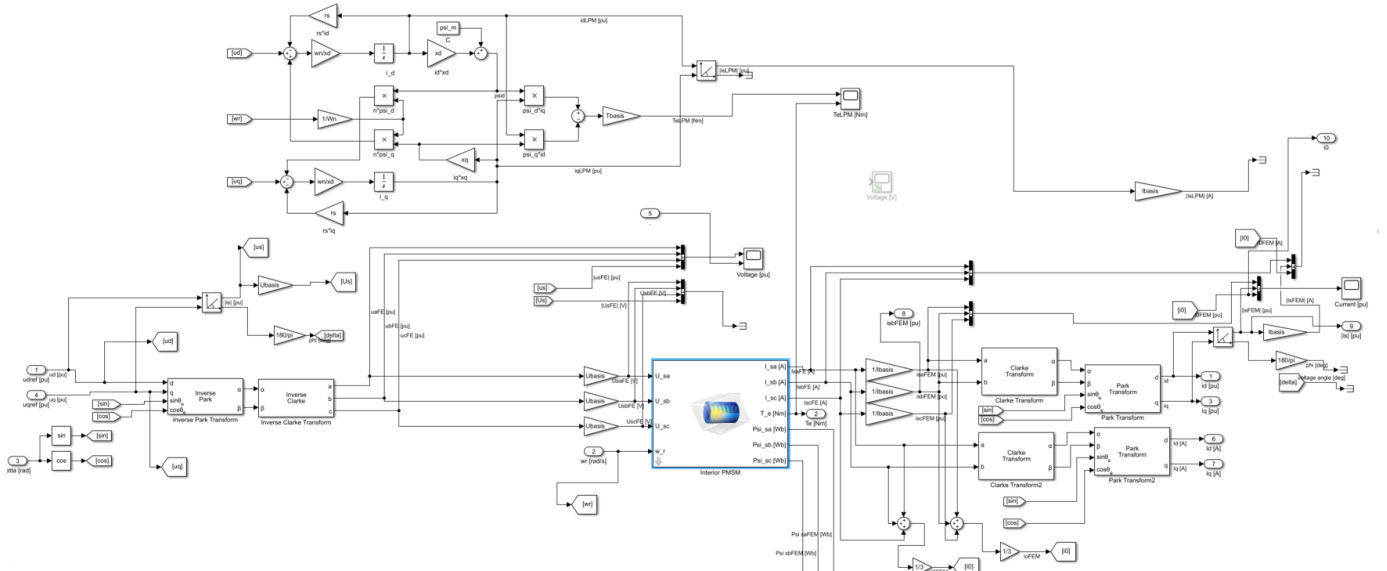


Fig. 56: This is below the "FEA IMPMS"-mask.

## CONTENTS

<b>I</b>	<b>Introduction</b>	2	<b>VI</b>	<b>Method - Co-Simulation Set Up</b>	15
I-A	Relation to the Specialization Project . . .	3	VI-A	Co-Simulation Set Up in COMSOL . . .	15
I-B	Targets and Scope . . . . .	3	VI-B	Co-Simulation Settings in Simulink . . .	16
I-C	Organization of the Thesis . . . . .	3	VI-C	Time Stepping . . . . .	17
	I-C1 Chapters . . . . .	3	VI-D	Notes on Post-Processing . . . . .	17
	I-C2 Notation . . . . .	3	<b>VII</b>	<b>Results</b>	17
<b>II</b>	<b>Theory - FEM and machine design</b>	3	VII-A	Introduction . . . . .	17
II-A	Introduction . . . . .	3	VII-B	Control, Stability and Frequency Response	17
II-B	IPMSM . . . . .	3	VII-C	MTPA Rated Torque reference . . . . .	19
II-C	Coils and Phase Sequence . . . . .	4	VII-D	MTPA Rated and Negative Value . . . . .	19
	II-C1 Conductor Model and Group	4	VII-E	MTPA 1.6 pu and 1.0 pu Torque Reference	19
	II-C2 Coil Excitation . . . . .	4	VII-F	MTPA Stair reference . . . . .	21
II-D	Boundary Conditions . . . . .	5	VII-G	Speed Control with LPM . . . . .	22
II-E	Electrical Steel . . . . .	5	VII-H	Speed Control with LPM with Feed- back from FEM . . . . .	23
II-F	Magnet Description in Cylindrical Co- ordinates . . . . .	5	VII-I	Comparison of Arkkio's method and Co-Energy Torque . . . . .	23
II-G	Flux Distribution . . . . .	5	VII-J	Harmonic Analysis, Motor Saturation and Inductances . . . . .	23
II-H	Torque . . . . .	6	<b>VIII</b>	<b>Discussion</b>	23
II-I	External Circuit Star Connection . . . . .	6	VIII-A	Introduction . . . . .	23
II-J	Current Direction in External Circuit . . .	6	VIII-B	Modeling for Co-Simulation Summary . .	23
II-K	Induced EMF . . . . .	6	VIII-C	Potential of Co-Simulations . . . . .	24
II-L	Determining the Controller Parameters for an IPMSM . . . . .	7	VIII-D	Limitations with Co-Simulations . . . . .	25
<b>III</b>	<b>Theory - Control of an IPMSM</b>	7	VIII-E	MTPA Step Reference . . . . .	25
III-A	Introduction . . . . .	7	VIII-F	MTPA Rated Negative . . . . .	25
	III-A1 Space Vector of IPMSM . . .	7	VIII-G	MTPA 1.6 pu and 1.0 Pu . . . . .	25
	III-A2 Transformations . . . . .	7	VIII-H	MTPA Stair . . . . .	26
	III-A3 Basis Values and Per Unit Values . . . . .	8	VIII-I	Speed Control . . . . .	26
	III-A4 Power Electronics Model . . .	8	VIII-J	Parameters . . . . .	26
	III-A5 MTPA and Mechanical Model	8	VIII-K	Frequency Response, Stability and Switching Frequency . . . . .	26
III-B	Control Theory . . . . .	8	<b>IX</b>	<b>Conclusion</b>	27
III-C	Torque and Current Controllers - Mod- ulus Optimum Control . . . . .	9	IX-A	Conclusion . . . . .	27
III-D	Cross-Coupling and Saturation . . . . .	9	IX-B	Further Work . . . . .	28
III-E	Speed Control Symmetrical Optimum . .	10	<b>Appendix A: Co-simulation Results</b>		31
<b>IV</b>	<b>Theory - Co-Simulation</b>	10	<b>Appendix B: IPMSM Data and Geometry</b>		43
IV-A	General . . . . .	10	<b>Appendix C: Correct Circuit</b>		44
IV-B	Time Stepping . . . . .	10	C-A	Attempt Without External Circuit . . . . .	44
IV-C	Softwares, Standards, Functional Mock- up Unit . . . . .	10	C-B	Attempt with Isolated Neutral . . . . .	44
<b>V</b>	<b>Method - FEM modelling</b>	10	<b>Appendix D: Matlab Script</b>		46
V-A	Introduction . . . . .	10	<b>Appendix E: Simulink</b>		48
V-B	Reverse Engineering . . . . .	11			
V-C	Coils and Phase Sequence . . . . .	11			
V-D	Moving Mesh Rotating Domain . . . . .	12			
	V-D1 General Angular Velocity . . .	12			
	V-D2 Position Integration . . . . .	13			
V-E	Mesh Refinement . . . . .	13			
V-F	External Circuit . . . . .	13			
V-G	Parameters for the Regulators . . . . .	15			



## SYMBOLS

## LIST OF SYMBOLS AND VARIABLES

$\Delta t_i$	communication time step in co-simulations [s]	$t_0(s)$	OL numerator(Norwegian: teller)
<b>C</b>	connection graph matrix for co-simulation	$T_i$	integral time constant in controller [s]
<b>u</b>	co-simulation input vector	$t_i$	communication points in co-simulation
<b>y</b>	co-simulation output vector	$T_{delay}$	converter delay time constant [s]
$\mu_r$	relative permeability	$T_d$	electric time constant [s]
$\Omega$	rotor speed [rad/s]	$T_{eq,i}$	equivalent current control time constant [s]
$\omega$	electrical frequency in [rad/s]	$T_{eq,n}$	equivalent speed control time constant [s]
$\omega_r$	rotor speed input parameter used in LiveLink [rad/s]	$T_m$	mechanical time constant [s]
$\psi_d$	d-axis flux linkage [pu]	$T_q$	electric time constant [s]
$\psi_m$	flux linkage PM in [pu]	$T_{sum}$	small time constant [s]
$\psi_q$	q-axis flux linkage [pu]	$T_{sw}$	switching period [s]
$\psi_T$	reluctance component of the total flux linkage [pu]	$u_d$	d-axis voltage [pu]
$\tau_L$	load torque [pu]	$u_q$	q-axis voltage [pu]
$\tau_p$	pole pitch [mm]	$x_d$	d-axis reactance [pu]
$\tau_{e,n}$	rated [pu] torque	$x_q$	q-axis reactance [pu]
$\tau_{emax}$	torque limit [pu]	$z$	discrete transfer function variable
$\tau_{eref}$	reference torque in [pu]		
$\vartheta$	electrical angle [rad]		
$\vartheta_m$	rotor position [rad]		
$A_z$	magnetic vector potential in the z-direction [Wb/m]		
$B_r$	remanent flux density in PM [T]		
$f_n$	nominal electrical frequency [Hz]		
$f_{sw}$	switching frequency [Hz]		
$h_0(s)$	open loop transfer function		
$i_d$	d-axis current [pu]		
$i_q$	q-axis current [pu]		
$i_s$	stator current magnitude [pu]		
$i_\alpha$	$\alpha$ -axis current [pu]		
$i_\beta$	$\beta$ -axis current [pu]		
$i_{sa}$	phase <i>a</i> stator current [pu]		
$i_{sb}$	phase <i>b</i> stator current [pu]		
$i_{sc}$	phase <i>c</i> stator current [pu]		
$J$	inertia [kgm <sup>2</sup> ]		
$J_z$	current density in the z-direction [A/mm <sup>2</sup> ]		
$K_p$	gain in the p part of a PI-controller		
$k_w$	winding factor		
$L$	inductance in [mH]		
$L_s$	active machine length [mm]		
$l_s$	stator inductance [pu]		
$l_w$	length of the end winding [mm]		
$L_w^s$	end winding inductance [mH]		
$m$	number of phases		
$M(s)$	closed loop transfer function		
$n_0(s)$	OL denominator (Norwegian: nevner)		
$N_n$	poles in the right half plane of $M(s)$		
$N_n$	rated speed [RPM]		
$n_n$	rated speed [pu]		
$N_p$	poles in the right half plane of $h_0(s)$		
$N_s$	stator coil-turns per phase		
$p$	poles in an electric machine		
$Q_s$	number of stator slots		
$q_s$	slots per pole per phase		
$r_s$	stator resistance [pu]		
$R_{end}^s$	stator end winding resistance [Ohm]		
$s$	continuous transfer function variable		

	ABBREVIATION DESCRIPTION
BEV	battery electric vehicle
CC	current controller
CL	closed loop transfer function
CS	co-simulation
CS1	co-simulation case with parameter $L_{d1}$
CS2	co-simulation case with parameter $L_{d2}$
Cu	copper
CPU	central processing unit
<b>EC</b>	external circuit physics in Comsol
FE	finite element
FEA	finite element analysis
FEM	finite element method
FMU	functional mock-up unit file format
FOC	field oriented vector control
FWM	fundamental wave model
IGBT	transistor
IM	induction machine
IPMSM	interior permanent magnet synchronous motor
LPM	lumped parameter model
MMF	magnetomotive force
MPH	Comsol Desktop file format
MTPA	maximum torque per ampere control
NdFeB	Neodymium Iron Boron
NGO	non grain oriented
NTNU	Norwegian University of Science and Technology
OL	open loop transfer function
PI	proportional integral
PM	permanent magnet
PMSG	permanent magnet synchronous generator
<b>RMM</b>	rotating magnetic machinery physics in Comsol
RPM	round per minute
SC	speed controller
SPMSM	surface permanent magnet synchronous machine
SR	saliency ratio
SV-PWM	space vector - pulse width modulation
THD	total harmonic distortion
VSI	voltage source inverter
ZOH	zero order hold

